Matrix Approach of Waves in Complex Media: From Ultrasound to Optics and Seismology

Alexandre Aubry

PSL UNIVERSITÉ PARIS

MÉMOIRE D'HABILITATION À DIRIGER DES RECHERCHES

DE L'UNIVERSITÉ PSL

Préparé à École Supérieure de Physique et de Chimie Industrielles de la ville de Paris

Matrix Approach of Waves in Complex Media: From Ultrasound to Optics and Seismology

Soutenu par

Alexandre Aubry

Le 27 Septembre 2022

Préparé à

l'Institut Langevin

Institut Langevin
ONDES ET IMAGES

Composition du jury :

Hui CAO Professeure à Yale University	*Rapporteure*
Stefan CATHELINE Directeur de Recherche INSERM	*Examinateur*
Mathias FINK Professeur à l'ESPCI Paris	*Examinateur*
Ori KATZ Professeur à Hebrew University of Jerusalem	*Examinateur*
Josselin GARNIER Professeur à l'Ecole Polytechnique	*Examinateur*
Philippe ROUX Directeur de Recherche CNRS	*Rapporteur*
Anne SENTENAC Directrice de Recherche CNRS	*Rapporteure*

ESPCI PARIS | PSL

Résumé

En imagerie, on cherche à caractériser un milieu inconnu en le sondant avec une onde puis en analysant les échos réfléchis par le milieu. C'est, par exemple, le principe de l'échographie ultrasonore, de la tomographie par cohérence optique ou de la sismologie par réflexion. Cependant, la propagation des ondes entre les capteurs et le plan focal est souvent dégradée par les hétérogénéités du milieu lui-même. Elles peuvent induire des distorsions des fronts d'onde et des événements de diffusion multiple qui dégradent fortement la résolution et le contraste de l'image. Ces phénomènes constituent donc les limites les plus fondamentales de l'imagerie dans tous les domaines de la physique des ondes.

Cependant, l'émergence des réseaux multi-éléments et les progrès récents en science des données ouvrent la voie à une nouvelle révolution en imagerie. Dans ce contexte, nous avons développé une approche matricielle de l'imagerie dans les milieux hétérogènes. Le formalisme matriciel est en effet un outil idoine pour compenser localement les aberrations sur de grands champs de vision, brisant ainsi les limites actuelles des méthodes de focalisation adaptative. Il conduit également au changement de paradigme suivant en imagerie: Alors que la diffusion multiple est généralement considérée comme un cauchemar, l'approche matricielle peut en tirer profit pour une imagerie hautement résolue et ultra-profonde des milieux diffusants. L'imagerie matricielle est également un outil de caractérisation prometteur puisqu'elle peut fournir une tomographie à haute résolution de la vitesse des ondes et des paramètres de diffusion. Tous ces concepts sont appliqués à la fois à l'optique (pour l'imagerie des tissus biologiques), à l'échographie (pour le diagnostic médical) et à la sismologie (pour la surveillance des volcans et des failles sismiques).

D'un point de vue plus fondamental, un formalisme matriciel est particulièrement adéquat pour sonder le transport des ondes dans les milieux fortement diffusants. D'une part, l'interférence constructive entre des chemins de diffusion réciproques peut ralentir, voire stopper le processus de diffusion. D'autre part, les phénomènes d'interférence peuvent, au contraire, aider les ondes à trouver leur chemin à travers un dédale de diffuseurs. La matrice de diffusion constitue alors un outil unique pour sonder ces canaux de propagation ouverts et mettre en évidence l'importance des boucles de diffusion récurrentes au seuil de la localisation d'Anderson.

Abstract

In wave imaging, we aim at characterizing an unknown environment by actively probing it and then recording the waves reflected by the medium. It is, for example, the principle of ultrasound imaging, optical coherence tomography or reflection seismology. However, wave propagation from the sensors to the focal plane is often degraded by the heterogeneities of the medium itself. They can induce wave-front distortions (aberrations) and multiple scattering events that can strongly degrade the resolution and the contrast of the image. Aberration and multiple scattering thus constitute the most fundamental limits for imaging in all domains of wave physics.

However, the emergence of multi-element technology and recent advances in data science pave the way towards a next revolution in wave imaging. In that context, we developed a universal matrix approach of wave imaging in heterogeneous media. A matrix formalism is actually the perfect tool to locally compensate for aberrations over large imaging volumes, thus breaking the limitations of adaptive focusing methods. It also leads to the following paradigm shift in wave imaging: Whereas multiple scattering is generally seen as a nightmare, a matrix approach can take advantage of it for ultra-deep and high-resolution imaging. Our matrix approach is also a promising characterization tool since it can provide a high-resolution tomography of the wave velocity and of scattering parameters. All these concepts are applied to both optics (for in-depth imaging of biological tissues), ultrasound imaging (for medical diagnosis) and seismology (for monitoring of volcanoes and fault zones).

From a more fundamental perspective, a matrix formalism can also be particularly fruitful to probe exotic wave transport phenomena in the strong scattering regime. On the one hand, constructive interference between reciprocal multiple scattering paths can eventually stop the diffusion process, giving rise to Anderson localization. On the other hand, interference phenomena can also help waves to find a way through a maze of disorder. The scattering matrix provides a unique tool to probe these open/close scattering channels and highlight the importance of recurrent scattering loops at the onset of 3D Anderson localization.

Contents

CHAPTER 1

Introduction

In the past decades, there have been many proposals for the harnessing of waves through complex media. By taking advantage of the emergence of large-scale sensors array, it has been shown that one can tame wave-fields in order to take advantage of the complexity of propagation media to for instance, focus waves or image objects hidden behind them. This has been realized in acoustics using the concept of the time reversal mirror [1] or in optics using wave-front shaping techniques [2]. More fundamentally, a matrix formalism is particularly appropriate in wave physics when the wave field can be controlled by transmission and/or reception arrays of independent elements. Since an inhomogeneous medium can be treated as one realization of a random process, some aspects of random matrix theory [3] may be fruitfully applied to wave control or imaging through complex media [4]. The scattering matrix can fully describe the transmission and reflection of waves by a complex medium. My group provided the first experimental proof that a properly designed combination of incident waves could be fully transmitted through (or reflected by) a disordered medium, based on the existence of propagation channels which are essentially either closed or open (bimodal law) [5]. By investigating the Wigner-Smith time-delay matrix [6], we extended this proof to the time domain by synthesizing particle-like wave packets that remain focused in time and space throughout their complex trajectory [7].

While a subsequent amount of work has considered the transmission matrix for optimizing wave control and focusing through complex media [8–14], the reflection matrix has drawn much less attention until 2015 [15–20]. Yet, this configuration is often the most relevant for imaging purposes, as shown by W. Choi's group [21–23] in the context of optical coherence microscopy. Since 2011, my research work thus focused on the development of a universal reflection matrix approach of wave imaging with a wide range of applications going from optical microscopy or ultrasound imaging to radar technology or seismology. During my PhD thesis, I developed a

matrix method dedicated to target detection embedded in strongly scattering media [18, 24]. This approach relies on: (i) the memory effect to separate the single and multiple scattering contribution [25]; (ii) iterative time reversal [15] and random matrix theory [26] for the detection of bright scatterers. Since 2011, I extended this approach to deep imaging in turbid media with proof-of-concept demonstrations both in optical microscopy [19, 27], seismology [28] and non-destructive testing [25]. While the penetration depth shown by conventional imaging methods typically scales as one scattering mean free path ℓ_s (the typical distance between two scattering events) , matrix imaging pushes back this fundamental limit beyond $10\ell_s$ [29].

These spectacular results led me to the development of a full theory of matrix imaging. This approach is based on the projection of the reflection matrix into a family of bases that are chosen depending on the aimed application and the scattering regime we have to cope with. In particular, the projection of the reflection matrix into a focused basis brings much more information than the conventional confocal image that imaging scientists are used to manipulate. The concept is that focused beamforming enables the synthesis, in transmit and receive, of an array of virtual transducers [30] which map the entire medium to be imaged [31, 32]. First, it can lead to an estimation of the transmission matrix that links each sensor and image voxel [33–35]. This matrix is the Holy Grail for imaging since its inversion actually yields a reliable 3D image of the scattering medium, with an optimized contrast and a close-to-ideal resolution at every pixel. This resolution can actually be even better than in free space since the medium can be used as a scattering and/or kaleidoscopic lens [36, 37], as demonstrated by our recent work in seismology [38, 39]. Beyond direct imaging of the medium reflectivity, spatial maps of various characteristics of the propagating wave can be retrieved such as (i) the wave velocity that can be evaluated everywhere inside the medium, including in random speckle; (ii) a highly resolved spatial mapping of the prevalence of multiple scattering [31]; (iii) the mapping of local transport parameters that govern wave diffusion in the multiple scattering regime [40], thereby leading to a full characterization of scattering media.

While this latter contribution is often seen as a nightmare for imaging, it also gives rise to fascinating phenomena in mesoscopic physics such as coherent backscattering [41–43] or Anderson localization [44–46]. Disorder can indeed induce spectacular interference phenomena that can slow down or even stop wave diffusion. Again, the reflection matrix is shown to be a valuable tool to investigate such exotic phenomena. In particular, it allowed us to study phase transitions of wave transport in the strong scattering regime [47–49]. Interestingly, the predominance of recurrent scattering paths in the reflected wave-field has been highlighted, whether it be at the Anderson localization transition [47] or in a much weaker scattering regime [50].

Beyond a control of waves induced by disorder, I also explored, in collaboration with the team of Claire Prada, alternative ways for harnessing waves such as negative refraction [51] and the concept of complementary media [52, 53]. To that aim, guided elastic waves are perfect candidates. They actually display rich and complex dispersive properties [54] with the existence of zero group velocity (ZGV) points above which coexists Lamb modes with positive and negative phase velocity [55, 56]. By abruptly changing the thickness of a plate, a forward mode can be converted into a backward mode and vice versa, resulting in negative, refraction [57–59] or

negative reflection phenomena [60–63]. This led us to the design of devices consisting in plates of varying thickness, relying on the concept of complementary media, where a particular layout of negative index media can cloak an object with its anti-object, trap waves around a negative corner or image an object at the deep sub-wavelength scale by transporting its evanescent wavefield in the far-field [64].

This manuscript presents a selection of works carried out between my arrival at Institut Langevin as a CNRS researcher in 2011 and today on a matrix approach of wave propagation in complex media. The first Chapter presents a reflection matrix approach of wave imaging to overcome the fundamental problems of aberrations that generally pollute standard reflection imaging methods in inhomogeneous media. The second Chapter tackles the deep multiple scattering regime and proposes several strategies for target detection and imaging in a fog of scatterers. The third Chapter shows how the reflection matrix approach can be exploited, not only to retrieve an image of the medium reflectivity, but also to map quantitatively various characteristics of wave propagation such as the wave velocity or transport parameters that govern wave diffusion inside complex media. At last, the fourth Chapter shows how the reflection matrix is a relevant tool to probe fascinating interference phenomena induced by disorder that can force waves to find their path through maze of disorder, or inversely, slow down or even stop wave diffusion. Throughout this manuscript, all these concepts are applied both to ultrasound imaging (for medical diagnosis and non destructive testing), seismology (for imaging heterogeneous areas such as volcanoes and fault zones) and optics (for deep imaging of biological tissues).

CHAPTER 2

Reflection Matrix Imaging in Wave Physics

Publications

- A. Badon, V. Barolle, K. Irsch, A.C. Boccara, M. Fink, and A. Aubry, *Distortion matrix concept for deep imaging in scattering media*, Sci. Adv. **6**, eaay7170 (2020)
- W. Lambert, L. A. Cobus, M. Couade, M. Fink, and A. Aubry, *Reflection Matrix Approach for Quantitative Imaging of Scattering Media*, Phys. Rev. X **10**, 021048 (2020)
- W. Lambert, L. A. Cobus, T. Frappart, M. Fink, and A. Aubry, *Distortion matrix concept for deep optical imaging in scattering media*, Proc. Nat. Sci. Acad. USA **117**, 14645-14656 (2020)
- R. Touma, T. Blondel, A. Derode, M. Campillo, and A. Aubry, *A Distortion Matrix Framework for High-Resolution Passive Seismic 3D Imaging: Application to the San Jacinto Fault Zone, California*, Geophys. J. Int. **226**, 780-794 (2021)
- V. Barolle, J. Schoeller, P. Mecê, K. Groux, J.-M. Chassot, M. Fink, A. C. Boccara, and A. Aubry, *Manifestation of aberrations in full-field optical coherence tomography*, Opt. Express **29**, 22044-22065 (2021)
- W. Lambert, J. Robin, L. A. Cobus, M. Fink, and A. Aubry, *Ultrasound Matrix Imaging – Part I: The focused reflection matrix, the F-factor and the role of multiple scattering*, IEEE Trans. Med. Imag. **41**, 3907-3920 (2022)
- W. Lambert, L. A. Cobus, J. Robin, M. Fink, and A. Aubry, *Ultrasound matrix imaging – Part II: The distortion matrix for aberration correction over multiple isoplanatic patches*, IEEE Trans. Med. Imag. **41**, 3921-3938 (2022)

In wave imaging, we aim at characterizing an unknown environment by actively probing it and then recording the waves reflected by the medium. It is, for example, the principle of ultrasound imaging, optical coherence tomography for light or reflection seismology in geophysics. However, wave propagation from the sensors to the focal plane is often degraded by the heterogeneities of the medium itself. They can induce wave-front distortions (aberrations) and multiple scattering events that can strongly degrade the resolution and the contrast of the image. Aberration and multiple scattering thus constitute the most fundamental limits for imaging in all domains of wave physics.

However, the emergence of large-scale sensors array and recent advances in data science pave the way towards a next revolution in wave imaging. During these last ten years, we developed a universal matrix approach of wave imaging in heterogeneous media. Such a formalism is actually the perfect tool to capture the input-output correlations of the wave-field with a large network of sensors. Matrix imaging (MI) relies on the measurement of a reflection matrix $\mathbf{R}$ that contains the set of impulse responses between each sensor. A set of matrix operations are then applied to $\mathbf{R}$, in order to retrieve an image of the medium reflectivity. In particular, three key operators will be introduced: (*i*) the focused reflection matrix $\mathbf{R_{rr}}$ for a local quantification of aberrations and multiple scattering; (*ii*) the distortion matrix $\mathbf{D}$ for a compensation of high-order aberrations over large imaging volumes; (*iii*) the transmission matrix $\mathbf{T}$ which connects any point inside the medium with the sensor array outside. This matrix is the holy grail for imaging: it enables in vivo imaging with close-to-ideal resolution and contrast at every voxel.

MI will be shown to break the field-of-view and penetration depth limitations of conventional adaptive focusing methods. It also leads to the following paradigm shift in wave imaging: Whereas multiple scattering is generally seen as a nightmare for imaging, the matrix approach is capable of exploiting such complex paths for reaching a much thinner resolution than in free space. Throughout this first chapter, I will apply all these concepts both in ultrasound imaging (for medical diagnosis), seismology (for high-resolution imaging of volcanoes and fault zones) and optics (for in-depth imaging of biological tissues).

1 Problematic and state-of-the-art

The resolution of a wave imaging system can be defined as the ability to discern small details of an object. In conventional imaging, this resolution cannot overcome the diffraction limit of a half wavelength and may be further limited by the maximum collection angle of the imaging device. However, even with a perfect imaging system, the image quality is affected by the inhomogeneities of the propagation medium. Strong concentration of scatterers induces multiple scattering (MS) events [Fig. 2.1(a)] that randomize the directions of wave propagation, leading to a strong degradation of the image resolution and contrast. Even before entering into a multiple scattering regime, large-scale spatial variations of the wave velocity or, equivalently, of the refractive index, introduces aberrations as wave passes through the medium of interest [Fig. 2.1(b)]. Such problems are encountered in all domains of wave physics, in particular for the inspection of biological tissues, whether it be by ultrasound imaging or optical microscopy,

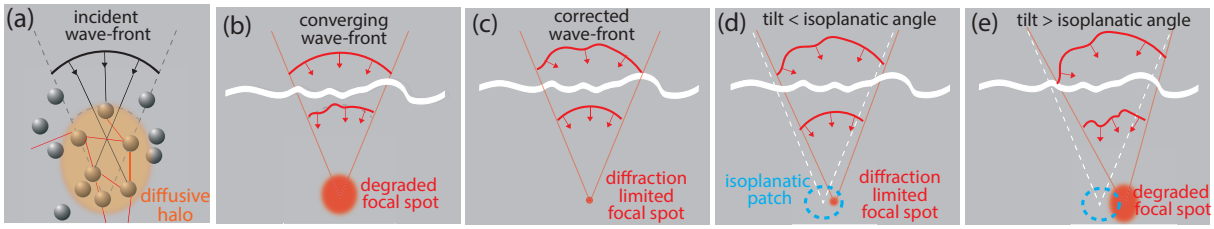

Figure 2.1: Fundamental limits in wave imaging: (a) Multiple scattering; (b) Aberrations. (c) Adaptive focusing techniques consist in modulating the incident or reflected wave-fronts by a phase law that compensates for the inhomogeneities of the medium. (d,e) This law remains valid over a finite area, often referred to as the isoplanatic patch, over which the aberrations can be considered as spatially-invariant.

or for the probing of natural resources or deep structure of the Earth's crust with seismic waves.

Originally, astronomers were the first to deal with aberration issues in wave imaging. To improve the quality of images, astronomers have proposed to measure and compensate for the wave-front distortions induced by the spatial variations of the optical index in the atmosphere: This is the principle of adaptive optics (AO), proposed as early as the 1950s [65]. This requires a loop that operates between a wave-front measuring device and a wave-front correction device. Subsequently, ultrasound imaging [66] and optical microscopy [67] have also drawn on the principles of AO to compensate for the aberrations induced by the deformed interfaces or tissues' inhomegeneities. Ultrasound imaging employs array of transducers that allows to control and record the amplitude and phase of broadband wave-fields. Conventional ultrasound uses adaptive focusing (AF) to form images. Wave-front distortions can be compensated for by adjusting the time-delays added to each emitted and/or detected signal in order to focus at a certain position inside the medium [68–71]. To correct for aberration of broadband acoustic fields, spatio-temporal matched filter methods have been proposed [72, 73]. Essentially, the signals to be sent into the medium are first convolved with a filter which is chosen for an optimal focusing in the sample. On a smaller scale, optical microscopy has also made great progress with the emergence of optical sectioning techniques: confocal microscopy [74], structured illumination microscopy [75], nonlinear microscopy [76] or optical coherence tomography (OCT) [77]. Adaptive optics has been applied to optical microscopy in the 2000s to overcome the specimen-induced aberrations [78–80]. Dynamic correction elements, such as deformable mirrors or spatial light modulators (SLM) have been employed to compensate specimen-induced aberrations. On a much larger scale, the migration of seismic data involves the backpropagation of the recorded wave-field from the region it was measured (Earth's surface) into the region to be imaged [81]. It requires a background model of seismic velocity. However, in some areas (typically, fault zones or volcanoes), the spatial and directional seismic wave speed variations cause strong distortions of the wave-fields [82]. A wealth of migration algorithms have been developed to correct for these aberrations but they are extremely resource-intensive [81].

Conventional AF methods generally requires the presence of a dominant scatterer (guide star) from which the signal to be optimized is reflected. While it is possible in some cases to generate

an artificial star, analyzing a wave-front returning from the depth of a complex biological sample is much less straightforward because it results from an incoherent superposition of many echoes due to unresolved scatterers (speckle image). Derived from stellar speckle interferometry[83], a first alternative is to extract the aberrating phase law from the spatial/angular correlations of the reflected wave-field as done in ultrasound imaging [69] or using a Sharck Hartmann sensor [84] and its numerical equivalent [85]. A second alternative is to retrieve the object the aberrations without measuring the wave-front, but only by optimizing the image quality, i.e. by deforming the incident and/or reflected wave-fronts in a controlled manner in order to converge towards an optimal image [86–90]. However, those methods generally imply an iterative time-consuming focusing process. In a strong aberration and/or scattering regime, an elegant trick is to exploit the spatial incoherence of the medium transmittance to retrieve the object's reflectivity from the auto-correlation of the scattered intensity [91–93]. Nevertheless, all the aforementioned methods rely on the assumption that aberrations do not change over the field-of-view (FOV) — a spatial invariance (or memory effect) [94–96] that is anything but true at large imaging depths [97] but also limited in a much weaker scattering regime as in ultrasound imaging [98]. High-order aberrations induced by short-scale fluctuations of wave speed are only invariant over small regions, often referred to as isoplanatic patches in the literature [Fig. 2.1(c,d)]. Conventional adaptive focusing methods thus suffer from a very limited FOV, which severely limits their performance for imaging heterogeneous media.

To go beyond the practical and intrinsic limits of adaptive focusing techniques, a matrix approach of wave focusing and imaging can be fruitful. Historically, a random matrix approach of wave propagation was first introduced in mesoscopic physics to describe wave transport through disordered media [3]. In the 1990s, the advent of multi-element technology has led to the development of a matrix formalism to describe the propagation of electromagnetic and ultrasonic waves between arrays of transducers [8, 9]. In the 2010s, the emergence of SLMs has allowed the extension of this transmission matrix approach to optics [10]. The experimental access to the transmission matrix has allowed to take advantage of multiple scattering for optimal light focusing [10–12] and communication [13, 99] across a diffusive layer or a multimode fiber. However, a transmission configuration is not adapted to non-invasive and/or in-vivo imaging of biological media. A reflection matrix approach should thus be considered. Until recently, apart from the seminal work of Robert and Fink [17], the reflection matrix had only been investigated for selective focusing in multi-target media[15, 19, 20, 100–102], diffraction tomography [16, 103] or energy delivery [104]. Yet, the emergence of large-scale sensor arrays in optics (SLM), acoustics (2D matrix array) and seismology (dense geophone array) is ideal for high-order aberration and multiple scattering compensation[21, 22, 33, 34, 38, 105].

During these last five years, we developed, in collaboration with Mathias Fink, a universal and non invasive reflection matrix approach for wave imaging and characterization in scattering media. Experimentally, this approach is based on the measurement of the reflection matrix $\mathbf{R}$ between sensors placed outside the medium of interest [Fig. 2.2(a)]. The goal is then to retrieve from these reflection measurements the transmission matrix $\mathbf{T}$ between the sensors and the set of voxels that map the medium [Fig. 2.2(b)]. The phase conjugate or pseudo-inversion

of this transmission matrix actually provide the focusing laws that should be applied from the sensors to optimally focus waves at any voxel inside the medium. The matrix formalism enables to perform this process in post-processing both in the transmit and receive modes. A matrix approach is particularly powerful since the reflection matrix can be easily projected between different bases both for: (*i*) the quantification of aberrations and multiple scattering; (*ii*) a local and optimized aberration compensation for any image voxel. In the next section, we describe these different matrix manipulations with ultrasonic waves before showing the benefits of MI in terms of: (*i*) super-resolution through the passive seismic imaging of fault zones and volcanoes; (*ii*) penetration depth for optical microscopy of biological tissues; .

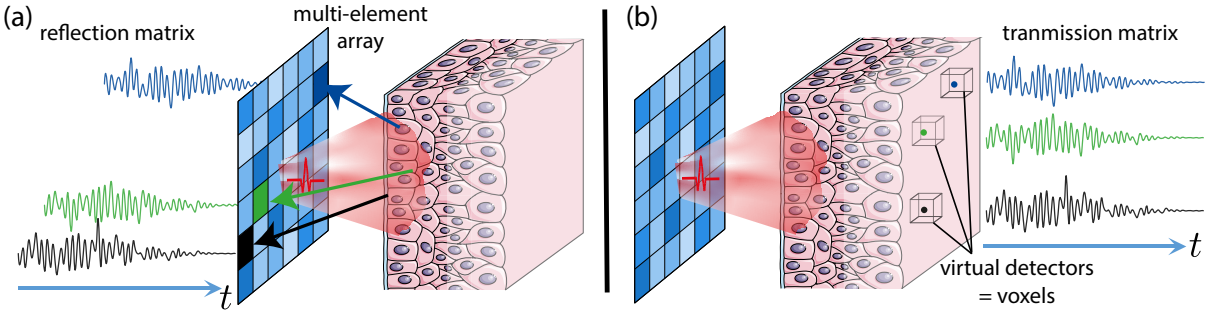

Figure 2.2: Principle of matrix imaging: From a reflection matrix that contains the set of impulse response between an array of sensors (a), the aim of MI is to estimate the transmission matrix between the sensors outside the medium and the set of voxels mapping the medium.

2 An Ultrasound Proof-of-Concept

To investigate soft tissues in ultrasound imaging, a sequence of incident waves is used to insonify the medium. Inside the medium, the waves encounter short-scale fluctuations of acoustic impedance, generating back-scattered echoes that are used to build an ultrasound image. Conventionally, this estimation of the medium reflectivity is performed using the process of delay-and-sum (DAS) beamforming, which relies on a coherent summation of the signals associated with each echo generated by scatterers in the medium [Fig. 2.3(b)]. Signals from a particular echo are selected by computing the time-of-flight associated with the forward and return travel paths of the ultrasonic wave between each transducer and the image voxel. From a physical point of view, time delays in transmission are used to concentrate the ultrasound wave on a focal area whose size is ideally only limited by diffraction. Time delays at reception select echoes coming from this excited area [Fig. 2.3(b)]. This process falls into the so-called confocal imaging techniques, meaning that, for each point of the image, a double focusing operation is performed.

The critical step of computing the time-of-flight for each insonification and each focal point is achieved in any clinical device by assuming the medium as homogeneous with a constant speed of sound. This assumption is necessary in order to achieve the rapidity required for real-time imaging; however, it may not be valid for some configurations in which long-scale fluctuations of the medium speed-of-sound impact wave propagation [106]. In soft tissues, such

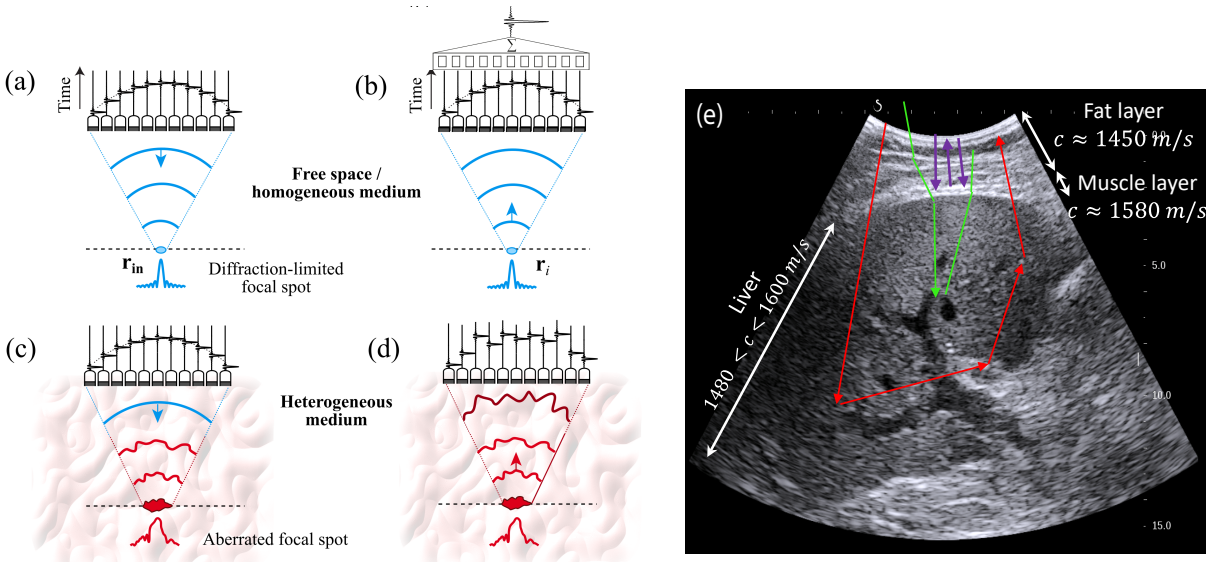

Figure 2.3: Principle of ultrasound imaging. (a) A focused wave is synthesized by applying parabolic time delays to the wavelet emitted by each transducer, producing a diffraction-limited focal spot at the targeted focal point. (b) In reception, the same time delays are applied to the back-scattered echoes before summing them coherently. The resulting signal at the ballistic time is the value assigned to one pixel of a standard ultrasound image. (c) In soft tissues, the fluctuations of the background wave speed induce phase distortions on the focused wave-front, resulting in a degraded focal spot. (d) The reflected wave also undergoes additional time delays compared to the ideal case (b), which alters the coherent summation of echoes produced by each scatterer at the end of the imaging process. (e) Aberrations, that can also be depicted as deviations of incident and reflected paths (green line), degrade the contrast and resolution of the ultrasound image (of, here, a liver). Beyond aberrations, multiple reflections between tissue interfaces (purple arrows) can give rise to reverberation artifacts. Multiple scattering paths (red arrows) generate an incoherent background that degrades the contrast of the ultrasound image.

fluctuations are around 5%, as the speed of sound typically ranges from 1400 m/s (*e.g.* fat tissues) to 1650 m/s (*e.g.* skin, muscle tissues) [107]. In such situations, the incident focal spot spreads beyond the diffraction-limited area, the exciting pressure field at this focusing point is reduced, and undesired echoes are generated by surrounding areas [Fig. 2.3(c)]. In reception, the application of an incorrect time delay profile mixes echoes which originate from neighboring points in the medium, resulting in a distorted point spread function (PSF) at the output [Fig. 2.3(d)]. These aberrating effects can strongly degrade the image resolution and contrast. For highly heterogeneous media, such aberrations may impact the diagnosis of the medical exam or limit the capability to image some organs. A classic example of this effect is liver imaging of difficult-to-image patients. Because the ultrasonic waves must travel through successive layers of skin, fat, and muscle tissue before reaching the liver, both the incident and reflected wave-fronts undergo strong aberrations [108] [green arrows in Fig. 2.3(e)].

Besides the problem of aberrations, an ultrasound image will be a reliable estimator of the medium reflectivity provided that back-scattered echoes only result from a single scattering process. Yet multiple scattering can be far from being negligible in soft tissues[102] [red arrows in Fig. 2.3(e)]. A local quantification of the multiple scattering component is thus required in order

to assess the reliability of the ultrasound image. Moreover, multiple reflection events between tissue interfaces, organ walls or bones induce reverberation artifacts on the ultrasound image [purple arrows in Fig. 2.3(e)]. The removal or, better, the compensation of such reverberation echoes would be particularly rewarding to help clinicians in their diagnostic.

Advanced synthetic beamforming relies on a double focusing operation at transmission and reception on each point of the medium [Fig. 2.5(b)]. Contrastedly, MI consists in decoupling the location of these transmitted and received focal spots [Fig. 2.5(c)]. The response between those virtual transducers form the so-called focused reflection matrix that actually contains much more information than a confocal ultrasound image. First, spatial maps of various characteristics of the propagating wave can be retrieved. In a first part, we will demonstrate: (*i*) a local focusing criterion that enables the focusing quality to be evaluated everywhere inside the medium, including in random speckle, and (*ii*) a highly resolved spatial mapping of the prevalence of multiple scattering, which constitutes a new and unique contrast for ultrasonic imaging. Second, we will show how these detrimental effects can be compensated by introducing the distortion matrix concept. This operator essentially connects any focal point inside the medium with the distortion that a wave front, emitted from that point, experiences due to heterogeneities. A time-reversal analysis of the distortion matrix enables the estimation of the transmission matrix that links each sensor and image voxel. Phase aberrations can then be unscrambled for any point, providing a full-field image of the medium with diffraction-limited resolution. Importantly, this process is particularly efficient for spatially-distributed aberrations, where traditional approaches such as adaptive focusing fail.

2.1 Acquisition of the reflection matrix

The experimental aspect of our matrix approach consists in recording the reflection matrix using an ultrasonic transducer array placed in direct contact with the medium to be imaged. To illustrate the MI process, we will consider, in the following, the reflection matrix acquired on the calf of a healthy volunteer [32]. The simplest acquisition sequence for the reflection matrix is to emit with one element at a time, and for each emission record with all elements the time-dependent field reflected back from the medium [Fig. 2.4(a)]. This canonical basis was first used to describe the so-called time-reversal operator [15], and is now commonly used in non destructive testing where it is referred to as the full matrix capture sequence [109]. A matrix acquired in this way can be written mathematically as $\mathbf{R_{uu}}(t) \equiv [R(\mathbf{u}_{\text{out}}, \mathbf{u}_{\text{in}}, t)]$, where $\mathbf{u}$ is the position of elements along the array, 'in' denotes transmission, and 'out' denotes reception [Fig. 2.4(b)]. Alternately, the response matrix can be acquired using beamforming (emitting and/or receiving with all elements in concert with appropriate time delays applied to each element) to form, for example, focused beams as in the conventional B-mode [66] or plane waves for high frame rate imaging [110] [Fig. 2.4(c)]. To demonstrate the compatibility of our method with state-of-the-art medical technology, our data is here acquired using plane-wave beamforming in emission and recording with individual elements in reception. A set of plane waves is used to probe the medium of interest [Fig. 2.4(c)]. For each plane wave emitted with an incident angle θ_{in}, the time-dependent reflected wavefield is recorded by the transducers. The corresponding signals

are stored in a reflection matrix $\mathbf{R}_{\mathbf{u}\theta}(t) = [R(\mathbf{u}_{\text{out}}, \theta_{\text{in}}, t)]$ [Fig. 2.4(d)].

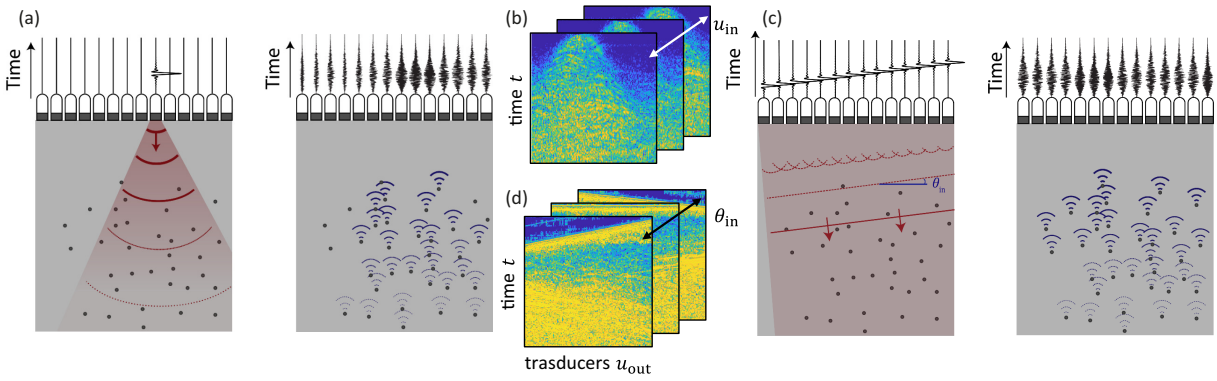

Figure 2.4: Acquisition of the reflection matrix. (a) The simplest acquisition sequence is to emit with one element $\mathbf{u}_{\text{in}}$ at a time, and for each emission record with all elements the time-dependent field reflected back from the medium, $R(\mathbf{u}_{\text{out}}, \mathbf{u}_{\text{in}}, t)$. (b) At the end of the process, all these wave-fields are stored in a canonical reflection matrix expressed in the transducer basis both at input and output: $\mathbf{R}_{\mathbf{uu}}(t) = [R(\mathbf{u}_{\text{out}}, \mathbf{u}_{\text{in}}, t)]$. (c) A faster acquisition sequence is to insonify the medium with a set of plane waves (with incident angle θ_{in}) and record, for each illumination, the time-dependent reflected field at each transducer element $\mathbf{u}_{\text{out}}$. (d) Thee resulting reflection matrix $\mathbf{R}_{u\theta}(t)$ is defined between the plane wave and transducer bases at input and output, respectively.

An ultrasound image can then be formed by coherently summing the recorded echoes coming from each focal point $\mathbf{r}$, which then acts as a virtual detector inside the medium. In practice, this is done by applying appropriate time delays to the recorded signals [110]. The images obtained for each incident plane wave are then summed up coherently and result in a final compounded image with upgraded contrast [see Fig. 2.5(a)]. This last operation generates *a posteriori* a synthetic focusing (i.e. a virtual source) on each focal point [see Fig. 2.5(b)]. The compounded image is thus equivalent to a confocal image that would be obtained by focusing waves on the same point in both the transmit and receive modes. However, there is much more information in the acquired reflection matrix that just a confocal image. A set of matrix operations can actually be applied to it in order to extract the relevant information as a function of the problem considered. For characterization and imaging purposes, a projection the reflection matrix into a focused basis is particularly fruitful as will be shown now .

2.2 Focused Reflection Matrix

In contrast with conventional ultrasound imaging that relies on confocal beamforming, the idea here is to apply independent focused beamforming procedures at the input and output of the reflection matrix [see Fig. 2.5(c)]. This process yields a focused reflection (FR) matrix $\mathbf{R}_{\mathbf{rr}}$ that contains the responses $R(\mathbf{r}_{\text{out}}, \mathbf{r}_{\text{in}})$ between virtual transducers synthesized directly in the medium from the transmitted and received focal spots located at points $\mathbf{r}_{\text{in}}$ and $\mathbf{r}_{\text{out}}$, respectively. It can be done through beamforming operations either, in the time domain, via conventional delay-and-sum beamforming applied to the complex RF signals [35]; or in the frequency domain, by applying appropriate phase shifts to all frequency components of the received signals in order

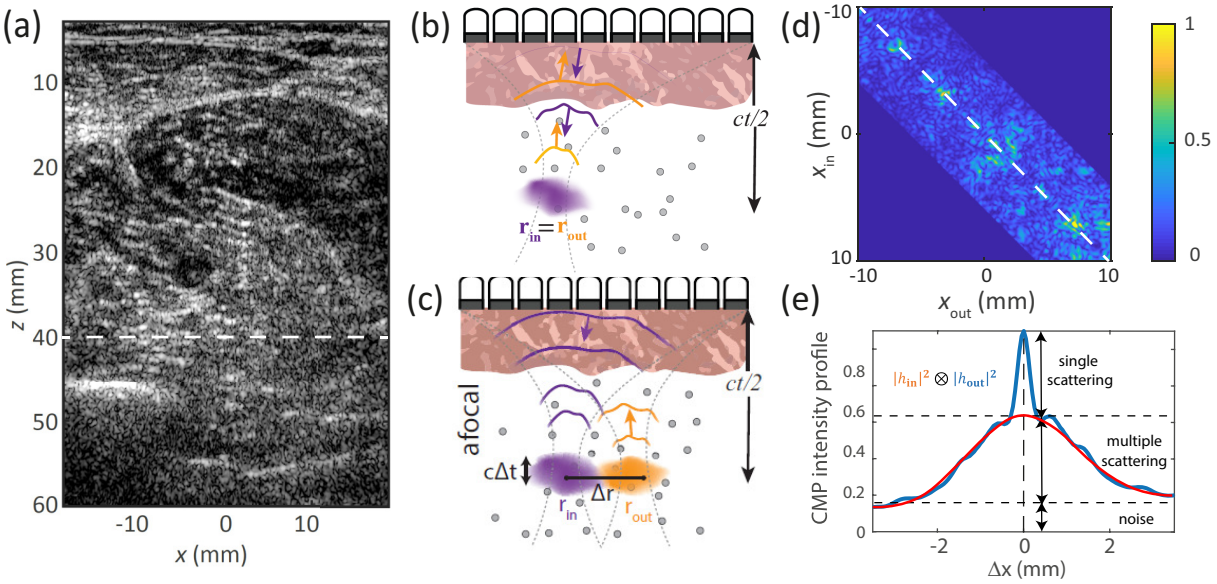

Figure 2.5: Principle of the focused reflection matrix approach. (a) Ultrasound image of a calf that results from (b) a standard confocal beamforming performed at input and output on each point of the field-of-view. (c) Ultrasound MI consists in an independent focused beamforming process at input and output to probe the response between distinct points $\mathbf{r}_{\text{in}}$ and $\mathbf{r}_{\text{out}}$ in emission and reception. (d) The set of impulse responses between such virtual transducers form a focused reflection matrix $\mathbf{R}_{xx}$ at each depth ($z = 40$ mm, here). (e) The associated CMP intensity enables the discrimination between the single scattering, multiple scattering and noise contributions to the back-scattered wave-field.

to realign them at each focal point. In the latter case, a matrix formalism is particularly suitable for this operation, because, in the frequency domain, the projection of data from the plane-wave or transducer bases to any focal plane can be achieved with a simple matrix product previously described by Lambert *et al.* [31]. Note that the focused basis corresponds to a set of vectors that are not linearly independent; this is therefore not, strictly speaking, a basis in a mathematical sense. In contrast, the incident plane waves used to record the reflection matrix are linearly independent, but they do not form a complete basis. Nevertheless, for convenience, we will refer to these two sets of wave-fronts as focused and plane wave bases in the following.

The result of the matrix beamforming process is a set of focused reflection matrices $\mathbf{R}_{\mathbf{rr}}(t)$. In contrast to standard synthetic ultrasound imaging, in which input and output focusing points coincide, the approach presented here decouples these points. In emission, the incident energy is concentrated at the focusing point $\mathbf{r}_{\text{in}}$; this point can thus be seen as a virtual source [111, 112]. Similarly, in reception, a virtual sensor is synthesized by selecting the part of the back-scattered wave-field originating from the vicinity of point $\mathbf{r}_{\text{out}}$. Therefore, each coefficient $R(\mathbf{r}_{\text{out}}, \mathbf{r}_{\text{in}}, t)$ of $\mathbf{R}_{\mathbf{rr}}(t)$ contains the time response of the medium between a set of virtual transducers. The position of each virtual transducer maps onto a pixel of the ultrasound image. Fig. 2.5(c) illustrates this matrix focusing process. Note that the concept of virtual transducers is merely didactic and that, of course, they do not act as real source or sink of energy. Moreover, they are strongly directive: in the downward direction for the virtual source, in the upward direction for

the virtual receiver.

In the rest of the section, we restrict our study to the $x-$projection of $\mathbf{R_{rr}}$ at time $t = 0$ (ballistic time). The corresponding sub-matrix will be written $\mathbf{R}_{xx}(z)$, in which only the ballistic responses between virtual transducers located at the same depth are considered ($z = z_{\text{in}} = z_{\text{out}}$). Figure 2.5(d) shows $\mathbf{R}_{xx}(z)$ depth at $z = 40$ mm in the calf experiment. It shows a sur-intensity along its diagonal elements that corresponds to the single scattering contribution [31]. Indeed, singly-scattered echoes can only originate from the point which was illuminated by the incident focal spot [see Fig. 2.6(a)]. In fact, the elements of $\mathbf{R_{rr}}$ which obey $\mathbf{r}_{\text{in}} = \mathbf{r}_{\text{out}}$ hold the information which would be obtained via multifocus (or confocal) imaging, in which transmit and receive focusing are performed at the same location for each point in the medium. The diagonal elements of $\mathbf{R}_{xx}(z)$, computed at each depth, corresponds to the line of the ultrasound image at the same depth.

Interestingly, the off-diagonal elements of $\mathbf{R_{rr}}$ can also provide valuable information on the physical properties of the medium, as well as on the wave focusing quality. To understand why this is, $\mathbf{R}_{xx}(z)$ can be expressed theoretically, as follows:

$$\mathbf{R}_{xx}(z) = \mathbf{H}_{\text{out}}^{\top}(z) \times \mathbf{\Gamma}(z) \times \mathbf{H}_{\text{in}}(z), \tag{2.1}$$

where the matrix $\mathbf{\Gamma}$ describes the scattering process in the sample; in the single scattering regime, $\mathbf{\Gamma}$ is diagonal and its elements correspond to the medium reflectivity $\gamma(\mathbf{r})$. $\mathbf{H}_{\text{in}}(z)$ and $\mathbf{H}_{\text{out}}(z)$ are the input and output focusing matrices, respectively [31]. Each column of $\mathbf{H}_{\text{in}}(z) = [H_{\text{in}}(x, x_{\text{in}}, z)]$ corresponds to one focused illumination, and contains the monochromatic PSF at emission – the spatial amplitude distribution of the input focal spot resulting from that particular illumination. Similarly, each column of $\mathbf{H}_{\text{out}}(z) = [H_{\text{out}}(x, x_{\text{out}}, z)]$ contains the spatial amplitude distribution of an output focal spot.

In the single scattering regime and for spatially-invariant aberration, the previous equation can be rewritten in terms of matrix coefficients as follows:

$$R(x_{\text{out}}, x_{\text{in}}, z) = \int dx H_{\text{out}}(x - x_{\text{out}}, z)\gamma(x, z)H_{\text{in}}(x - x_{\text{in}}, z). \tag{2.2}$$

This last equation confirms that the diagonal coefficients of $\mathbf{R}_{xx}(z)$, i.e. a line of the ultrasound image, result from a convolution between the sample reflectivity γ and the confocal PSF $H_{\text{in}} \times H_{\text{out}}$. As we will see, access to the off-diagonal elements of $\mathbf{R}_{xx}$ enables the probe of the input-output PSF in the vicinity of each focal point [Fig. 2.6(b)], thereby giving access to a local quantification of the focusing quality.

Another important feature in $\mathbf{R}_{xx}(z)$ is the existence of an incoherent wave-field that subsists whatever the distance between $\mathbf{r}_{\text{in}}$ and $\mathbf{r}_{\text{out}}$. The only possible physical origin of echoes between distant virtual transducers is the existence of multiple scattering paths occurring at depths shallower than the focal depth, as sketched in Fig. 2.6(c). Another non-physical origin is electronic noise that can hamper ultrasound data especially at large times-of-flight. To discriminate between both effects, spatial reciprocity theorem can be invoked. Unlike electronic noise, multiply-scattered waves actually check this fundamental property of wave equation and give

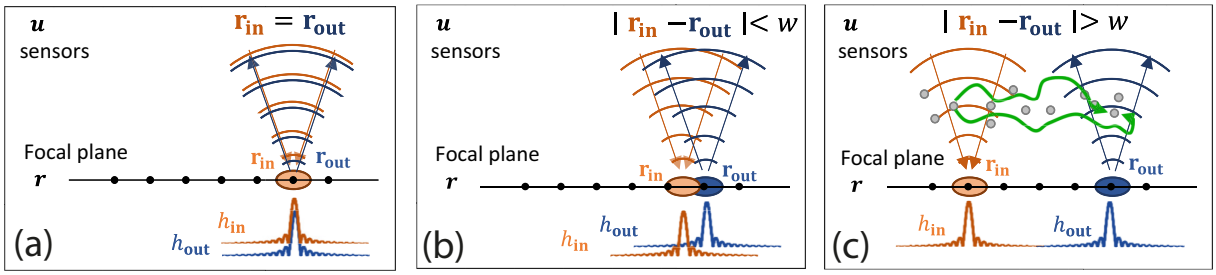

Figure 2.6: Manifestation of single scattering (a), aberrations (b) and multiple scattering (c) in the focused reflection matrix.

rise to a symmetric random reflection matrix. In Fig. 2.5(d), the reflection matrix is close to be symmetric, meaning that most of the off-diagonal signal can be attributed to multiple scattering events in the medium.

2.3 Focusing factor and multiple scattering rate

To go beyond this qualitative analysis and assess quantitatively the aberration and multiple scattering levels in the ultrasound image, a relevant observable is the mean intensity profile along each antidiagonal of $\mathbf{R}_{xx}$:

$$I(\mathbf{r}, \Delta x) = \left\langle |R(x + \Delta x/2, x - \Delta x/2, z)|^2 \right\rangle, \tag{2.3}$$

where $\langle \cdots \rangle$ denotes an average over the pairs of points $\mathbf{r}_{\text{in}} = (x_{\text{in}}, z)$ and $\mathbf{r}_{\text{out}} = (x_{\text{out}}, z)$ which share the same midpoint $\mathbf{r} = (\mathbf{r}_{\text{out}} + \mathbf{r}_{\text{in}})/2$, and $\Delta x = (x x_{\text{out}} - x_{\text{in}})$ is the relative position between those two points. We term $I(\mathbf{r}, \Delta x)$ the *common-midpoint intensity profile*. Whereas $\mathcal{I}(\mathbf{r})$ only contains the confocal intensity response from an impulse at point $\mathbf{r}$, $I(\mathbf{r}, \Delta x)$ is a measure of the spatially-dependent intensity response to an impulse at $\mathbf{r}$.

Figure 2.5(e) shows the corresponding common midpoint (CMP) intensity profile for the matrix $\mathbf{R}_{xx}$ displayed in Fig. 2.5(d). It shows a confocal peak mainly due to single scattering on top of a lower but wider pedestal linked to multiple scattering and noise. A fitting procedure developed by Lambert *et al.* [32] enables to discriminate between these different components. Local multiple scattering and electronic noise rates, $\alpha_M(\mathbf{r})$ and $\alpha_N(\mathbf{r})$, can then be assessed for each pixel $\mathbf{r}$ of the ultrasound image. The evolution of α_N is shown in Fig. 2.7(b). Unsurprisingly, a predominant noise occurs at large depth ($z > 50$ mm) and in areas where the medium reflectivity is weak. In any case, if a medical diagnosis is desired, the features of the ultrasound image in these areas should be more carefully interpreted. However, this is not the only factor which affects the quality of the ultrasound image [Fig. 2.7(a)]. Clutter is also far from being negligible at shallow depths due to multiple reflection events between superficial layers and at larger depths because of multiple scattering processes in speckle [Fig. 2.7(c)].

With regards to the single scattering component, it can be used to probe the focusing quality. Indeed, in the ultrasound speckle regime, the single scattering component of $I(\mathbf{r}, \Delta x)$ is shown to scale as the convolution between the incoherent output and input PSFs, $\left[|H_{\text{out}}|^2 \otimes |H_{\text{in}}|^2\right](\Delta x)$ [31]. In the following, we will refer to this quantity as the *reflection* point spread function (RPSF). By

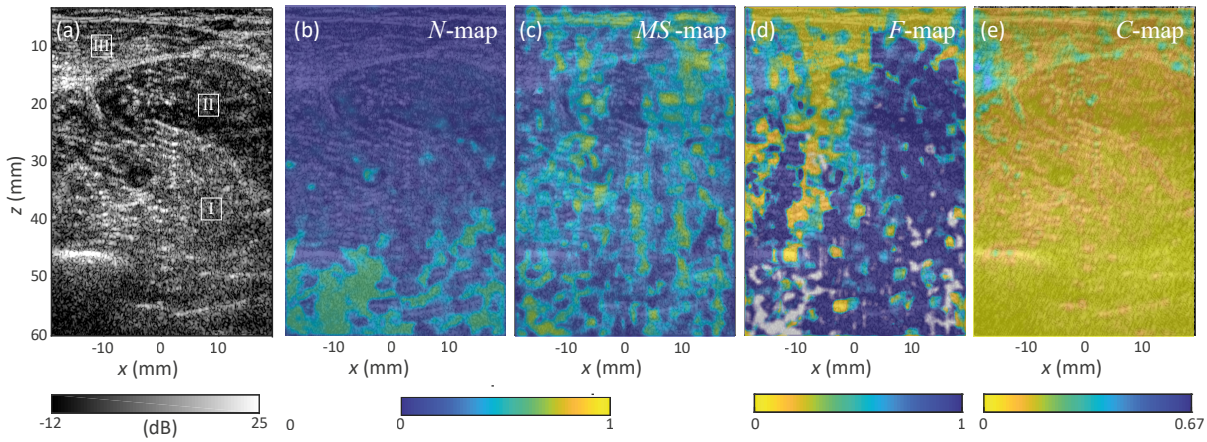

Figure 2.7: Mapping of local focusing quality and multiple scattering in the calf imaging experiment. (a) Ultrasound image of the calf. (b) Noise rate $\alpha_N()$. (c) Multiple scattering rate $\alpha_M()$. (d) F-factor. (d) $C-$factor. In (b,c) yellow areas correspond to a weak SNR and high multiple scattering rate, respectively. In (d,e) blue and yellow areas correspond to a high and low quality of focus respectively. In (d), gray areas highlights location where the estimation of the focusing criterion is not reliable because the incoherent background is too high ($\alpha_N + \alpha_M > 0.75$)

fitting the confocal peak of by a rescaled version of its ideal diffraction-limited profile, a focusing factor F can be extracted for each pixel of the ultrasound image. In first approximation, it corresponds to the ratio between the diffraction-limited resolution w_0 and the characteristic width w of the confocal peak. The focusing factor F is bounded between 0 ($w >> w_0$, bad focusing) and 1 ($w = w_0$, perfect focusing). F this provides a direct probe of the focusing quality at each pixel of the ultrasound image. The corresponding $F-$map is displayed by Fig. 2.7(d). The focusing quality shows strong variations across the field-of-view, particularly between the left and right parts of image. While high values of F (blue areas) indicate good image reliability, low values of F (green/yellow areas) indicate a poor quality of focus. As expected, yellow areas seem to correspond to blurring of the ultrasound image [Fig. 2.7(a)].

While our focusing criterion shows some similarities with the coherence factor C introduced by Mallart and Fink [71], the parameter F constitutes a much more sensitive and spatially-resolved probe of the focusing quality. To demonstrate this benefit, a map of the standard coherence factor C is built for the ultrasound image of the human calf [Fig. 2.7(d)]. C is equal to the ratio of the coherent intensity to the incoherent intensity of the realigned reflected wavefronts recorded by the probe for each input focusing beam [17, 71]. In the speckle regime, the coherence factor C ranges from 0, for strong aberrations, to 2/3 in the ideal case. Compared to the $F-$map [Fig. 2.7(d)], the coherence factor C provides a weakly contrasted image of the focusing quality. To understand this difference, one can notice first that the coherence factor C only probes the incoherent PSF, $|H_{\text{in}}|^2 \overset{\Delta x}{\circledast} |H_{\text{out}}|^2$, at $\Delta x = 0$ [32]. Moreover, it remains sensitive to multiple scattering and noise that can strongly hamper its measurement. Yet these incoherent components are far from being negligible and account for the low value of C throughout the field-of-view. Unlike the C-factor, the CMP intensity enables a clear discrimination between the single scattering contribution and the noise components. The $F-$factor is sensitive only

to aberrations, since it is estimated after removing the incoherent background. This crucial feature accounts for the difference in behavior between F and C in Fig. 2.7, especially at large depths. This result demonstrates one of the benefits of MI compared to standard ultrasound imaging: Probing the focusing quality in the focused basis drastically improves the robustness to multiple scattering and noise compared to a direct cross-correlation of back-scattered echoes in the transducer basis.

Beyond the focusing quality, the focusing criterion F can be exploited to map the spatial distribution of the speed of sound [31]. It can be also used as a virtual guide star for aberration correction in adaptive focusing. Currently, in the literature in this area, this role is performed by the coherence factor C [113–115]. In the following, we propose a more powerful approach to aberration correction for *in vivo* ultrasound imaging based on the distortion matrix concept. The $F-$factor can then be used to probe the focusing quality throughout the aberration correction process.

2.4 Distortion Matrix

Adaptive focusing methods have been developed to deal with aberrations, they rely on the hypothesis that the speed-of-sound variations occur only in a thin screen at the probe aperture. However, this assumption is simply incorrect in soft tissues [98] such as fat, skin and muscle, in which the order of magnitude of acoustic impedance fluctuations is around 5% [107]. This causes higher-order aberrations which are only invariant over small *isoplanatic patches*. To tackle this issue, recent studies [105, 116] leverages the multi-element capabilities of ultrasonic transducers via a post-processing of the recorded reflection matrix. An aberration law for each image voxel is retrieved by probing the correlation of the time-delayed echoes coming from adjacent focal spots. The aberration laws are estimated either in the time domain [105, 113, 117] or in the Fourier domain [17, 116], for different insonification sequences (focused beams [113], single-transducer insonification [116] or plane wave illumination [105]). In all of these techniques, a focusing law is estimated in a single correction basis (transducer or plane wave basis) either the receive [17, 113] or transmit [116, 117] mode. Yet, spatially-distributed aberrations that go in hand with small isoplanatic patches can only be addressed by investigating them from several correction planes. This is the principle of multi-conjugate adaptive focusing in optical microscopy [118, 119].

In a series of papers [34, 35], we have proposed a more general solution to optimize the information stored in the reflection matrix. Under this approach, the previously introduced focused reflection matrix introduced plays a pivotal role [Fig. 2.8(a)]. First, it enables the application of an adaptive confocal filter to: (*i*) reduce the detrimental influence of multiple scattering and/or noise; (*ii*) ensure a local isoplanaticity in order to converge towards a satisfying aberration law [35]. Second, working with the FR matrix allows easy projection of the input or output wave-fields into different bases (far-field, transducer plane, some intermediate surface, *etc.*) for optimal aberration correction. In contrast with previous studies that compensate aberrations from a single (transducer or plane wave) basis [17, 105, 116, 117], alternating correction bases is particularly relevant for spatially-distributed aberrations.

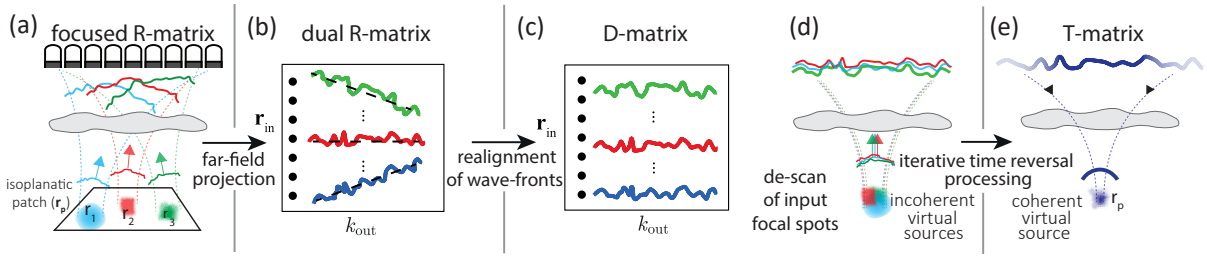

Figure 2.8: Principle of the distortion matrix approach. (a) A focused reflection matrix $\mathbf{R_{rr}}$ is considered over an arbitrary isoplanatic patch. (b) $\mathbf{R_{rr}}$ is projected in a correction basis $\mathbf{k}$ at input. Each column of the resulting dual matrix $\mathbf{R_{kr}}$ corresponds to the reflected wavefield induced by the associated virtual source $\mathbf{r_{in}}$. (c) By removing the geometrical curvature/tilt of each reflected wavefront, the resulting distortion matrix extracts the aberrated component of those wavefronts. From an other point of view, all the wavefronts are realigned as if they were generated by input focal spots that are virtually shifted at the same location. (d) A time reversal analysis of $\mathbf{D_{kr}}$ is applied to the virtual reflector that results from a coherent average of all the shifted input focal spots. It leads to an estimation of the aberration phase law over the considered isoplanatic patch.

A dual reflection matrix $\mathbf{R_{kr}}$ is obtained between the focused basis ($\mathbf{r}$) and an arbitrary correction plane ($\mathbf{k}$) [34, 35]. Reflected wave-fronts consist of two components [Fig. 2.8(b)]: (i) An ideal geometric wave-front linked to diffraction and the position of the input focusing point, and; (ii) Phase distortions induced by the speed-of-sound variations. These distortions are stored in a so-called distortion matrix $\mathbf{D_{kr}}$ [Fig. 2.8(c)]. A local time reversal analysis of $\mathbf{D_{kr}}$ performed over isoplanatic patches centered around each pixel $\mathbf{r}$ provides the corresponding aberration transmittance seen from that point [34, 35]. This set of aberration transmittance provides an estimator of the transmission matrix $\mathbf{T_{kr}}$ that links the correction basis ($\mathbf{k}$) and each pixel $\mathbf{r}$ of the focused basis [Fig. 2.9]. This matrix is the Holy Grail for imaging since its phase conjugate, or its pseudo inverse, yields optimized focusing laws for each pixel of the image. An updated focused refection matrix is retrieved and the whole process can then be iterated by extracting the input aberration phase laws from a set of local distortion matrices $\mathbf{D_{rk}}$. At last, the estimation of $\mathbf{T}$-matrices can be improved by applying an iterative strategy that consists in addressing alternative correction bases and gradually reducing the size of isoplanatic patches [35]. Thereby, compensation for high-order and spatially-distributed aberrations can be achieved. Phase aberrations can then be unscrambled for any point, providing a full-field image of the medium with a close-to-ideal resolution and optimized contrast.

Figure 2.10(b) and (d) shows the result of this aberration correction process on the calf image. The comparison with the standard ultrasound images [Fig. 2.10(a) and (c)] shows the benefit of MI. The resolution is enhanced by a factor 3 and the contrast improved by 3dB in the area surrounded by the white rectangle in Fig. 2.10(a) . The drastic gain in focusing quality is also quantified by means of the focusing factor [see comparison between Figs. 2.10(e) and (f)]. Most of the aberrations have been corrected by MI and the focusing parameter F is now close to 1 over a large part of the image [Fig. 2.10(f)].

At last, Figs. 2.10(g) and (h) illustrate the potential of ultrasound MI for clinical applica-

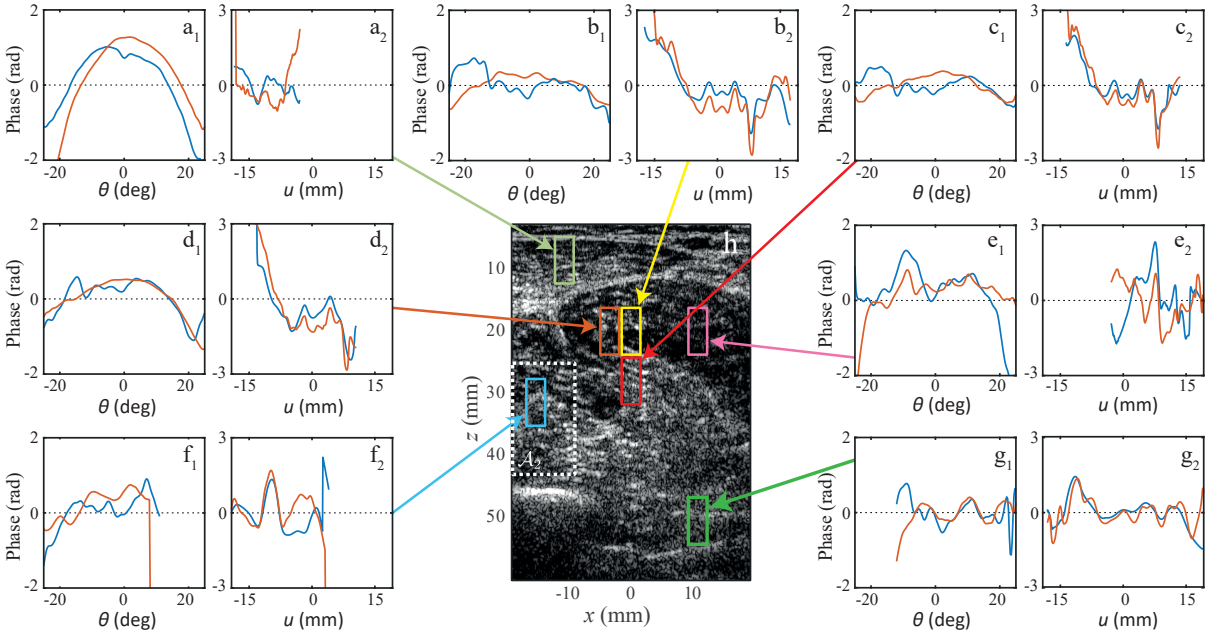

Figure 2.9: Examples of aberration phase laws resulting from the MI process, computed in transmit (blue curves) and in receive (red curves) modes, in the plane wave (1) and transducer (2) bases.

tions by considering the in-vivo imaging of a gallbladder. Ultrasound imaging is actually often used for diagnosis of cholecystitis [120] (inflammation of the gallbladder), either by detecting gallstones or identifying pericholic fluid and thickened gallbladder wall. The probe is placed in a subcostal position in order to image the gallbladder along its short axis. In this configuration, the gallbladder appears as a circular ring. In Fig. 2.10(g), the ultrasound image of the gallbladder internal wall shows a thickened gallbladder wall that leads to the wrong diagnosis of a gallbladder. On the contrary, MI indicates the presence of drastic aberrations and multiple scattering that explain the blurred aspect of the gallbladder on the ultrasound image [35]. The final matrix image finally reveals a clear view of the internal wall that was completely blurred in the original image. Therefore, this example shows the potential interest of MI for clinical applications.

Ultrasound MI thus constitutes a powerful tool for imaging a heterogeneous medium when little to no previous knowledge on the spatial variations of the speed-of-sound is available. It can be applied whatever the array geometry (curved probes, phased arrays, matrix arrays, *etc.*) or acquisition scheme (focused excitations, plane wave, diverging waves, *etc.*). Optimized contrast and resolution can be recovered for any pixel of the ultrasound image. Beyond ultrasound imaging, the distortion matrix concept is universal and can be applied to any field of wave physics for which multi-element technology is available. By now extending this approach to seismic imaging and optical microscopy, we will show how MI is a flexible and powerful tool since: (*i*) the reflection matrix can be acquired not only using active measurement but also extracted from passive measurements of the wave-field reflected by the medium of interest; (*ii*) it can be applied not only in the speckle regime (continuous random reflectivity) but also in

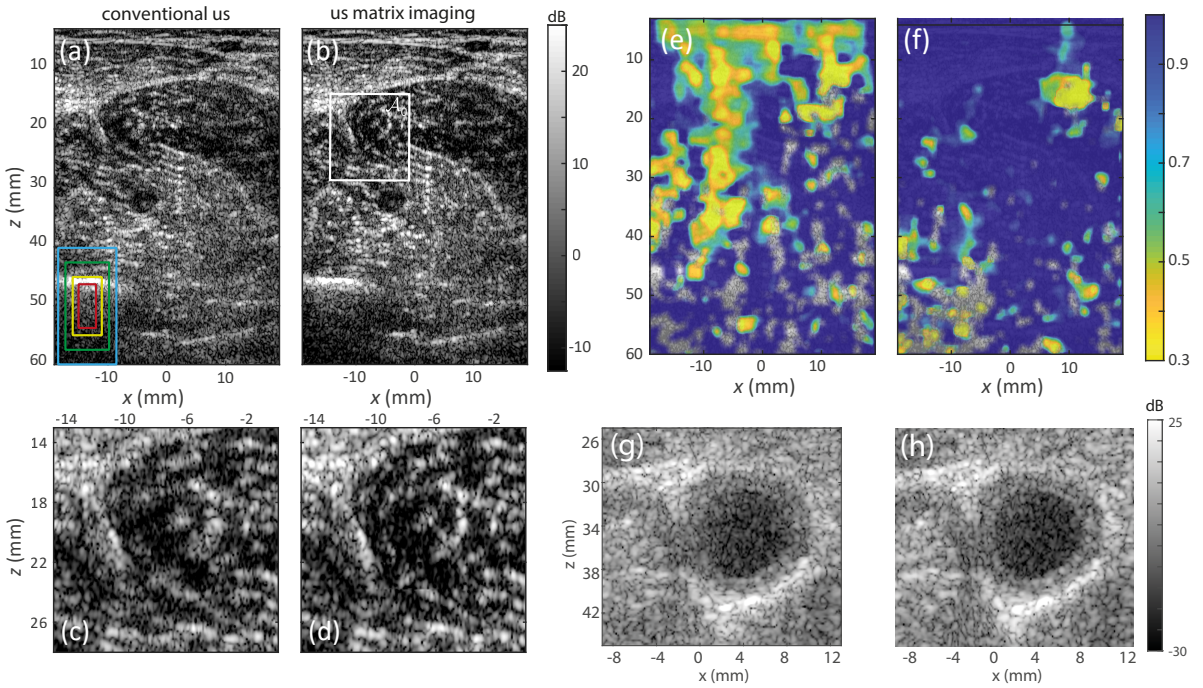

Figure 2.10: Results of the aberration correction process applied to *in-vivo* ultrasound imaging. (a,b) Ultrasound image of the calf before and after $\mathbf{T}-$matrix compensation of aberrations [34]. (c,d) Corresponding focusing factor [31]. (e,f) Zooms on the white rectangle displayed in (b). (g,h) Ultrasound images of a gall bladder before and after $\mathbf{T}-$matrix compensation of aberrations [35].

sparse and specular scattering regimes; (*iii*) it can exploit the medium complexity to improve significantly the resolution with respect to the diffraction limit; (*iv*) increase drastically the penetration depth in the multiple scattering regime.

3 Towards High Resolution: Passive Seismic Matrix Imaging

3.1 Seismic imaging context

Seismic waves constitute a powerful means to non destructively probe the Earth's crust. To do so, one has to solve the inverse problem that consists in deducing the medium internal properties from the recording of the seismic wave field at its surface. A first way to do so is to assume a velocity and density background, solve the forward problem to compute the time-dependent signal that would be backscattered if the background model was true, and iteratively update this model to minimize the difference with the actual recordings. Another way is to directly back-propagate the scattered echoes to reflectors inside the medium. This also amounts to updating a background model since a reflector is nothing else than a variation in acoustic impedance ρc. In both strategies, referred to as "inversion" and "migration", respectively, a celerity macro model is required and the purpose is to compute variations from this model under the assumption that they are small (Born approximation, see Fig. 2.11 (a)). If they are not, the reflected wave-field may be subject to aberrations [Fig. 2.11 (b)] and multiple scattering [Fig. 2.11 (c)] that the

macro model fails at modeling. These issues lead to distorted images, lack of resolution and unphysical features, which are very detrimental to the imaging process.

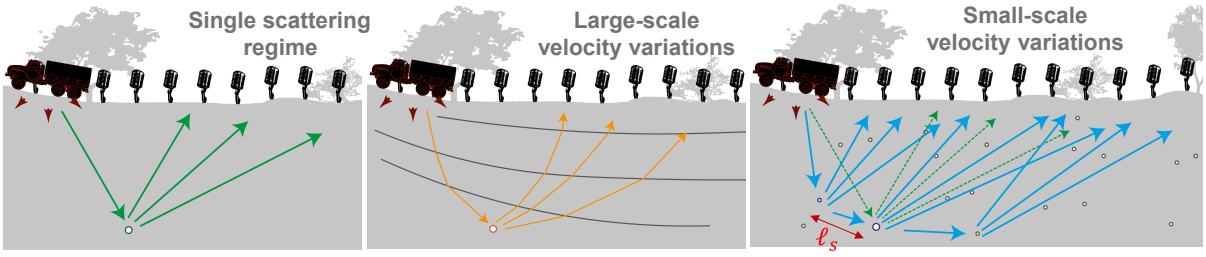

Figure 2.11: Fundamental limits in reflection seismology. (a) Based on a single scattering assumption, (b) reflection seismology requires a correct wave velocity model to account for the variations of bulk wave velocity between different geological units. (c) Multiple scattering can also arise in particularly heterogeneous areas such as fault zones or in volcanoes.

In seismic exploration, these issues are important because in most cases the celerity is non constant in space and its distribution is unknown. Most geological settings actually consist of several layers of rocks and sediments with distinct mechanical properties as well as location-dependent thickness, faulting and strata organization. These may be difficult to estimate without previous geologic expertise of the subsurface, especially in areas with high lateral mechanical stress that bend and break the layers and make them superimpose. When trying to retrieve details at a diffraction-limited resolution, the previous knowledge required to build reliable images may be already fairly demanding. On the one hand, the inversion problem cannot be solved if the initial celerity model is too far from the reality because the regularization procedure can end up stuck in a local minimum. On the other hand, migration techniques would lead to loss of resolution due to phase distortions and a blurred image due to multiple scattering. That being said, the question that naturally arises and which the present work aims at addressing is: how to retrieve an accurate image when little to no previous knowledge on the spatial variations of the wave speed is available?

To cope with this issue, our strategy has consisted in extending our matrix approach to seismic wave imaging. Indeed, overcoming phase distortions induced by wave velocity variations would be especially valuable for geophysical applications given the stratified structures of the environments of interest. Migration techniques in Fourier domain have actually been very popular for imaging in layered media [121, 122], however they only hold for 1D celerity models with no lateral variations. Subsequent works have focused on adapting these techniques to take into account increasing lateral velocity variations, at the cost of more numerical and computational complexity [123–125]. Contrary to these well-established methods, the matrix approach does not require any assumption on the structures and on the velocity distribution inside the medium, while being fairly light on the computational aspect. The present paper aims at studying the relevance of the matrix approach for geophysical imaging.

Coherent sources (vibrating trucks, explosives, *etc.*) can be used for reflection seismic imaging but the penetration depth is limited (<1 km), not to mention the cost of such measurements and the possible impact on the environment. Interestingly, incoherent signals (seismic noise) can

also be taken advantage of for imaging purposes. It was actually shown, twenty years ago, how a coherent information can be extracted from this incoherent seismic noise. Under appropriate wave-field conditions, the cross-correlation of seismic noise recorded by two stations was actually shown to yield the impulse response between them [126–131], providing new opportunities to develop imaging techniques without using active sources [see Fig. 2.12]. As surface waves dominate ambient noise, most papers on the topic aimed at extracting surface wave properties from ambient noise correlations [132–134]. However, a few studies also reported the retrieval of body wave reflection from noise correlations [135–138].

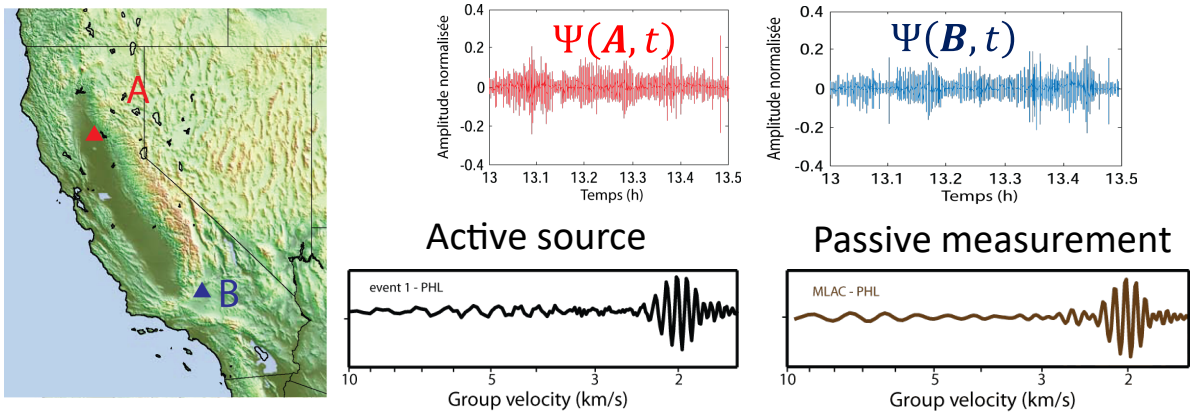

Figure 2.12: Green's functions retrieval from seismic noise cross-correlations. (a) Locations of two USArray stations in California. (b) Seismic noise recorded on each station. (c) Rayleigh waves recorded at A excited by earthquake at B. (d) Waveform emerging from cross-correlations of ambient seismic noise recorded at A and B (b). Figure taken from [132].

Based on this approach, the reflection matrix associated with a dense network of geophones can be extracted from the cross-correlations of seismic noise over time [28]. Here, as a the proof-of-concept, we have considered the spatially dense array of geophones deployed over the damage zone of the San Jacinto Fault zone (SJFZ) in California [139] [see Fig. 2.13]. Fault zones are indeed among the most challenging media for seismic imaging given their highly localized and abrupt variations of mechanical properties, extensive fractures and damage zone. In that respect, the SJFZ is the most seismically active fault zone in Southern California [140]. It accounts for a large portion of the plate motion in the region [141, 142]. A highly complex fault-zone structure with prominent lateral and vertical heterogeneities at various scales have already been highlighted in previous studies [143–145].

3.2 Passive 3D matrix imaging

The distortion matrix approach developed in the context of ultrasound is here extended to satisfy seismic imaging purposes. Compared to the ultrasound proof-of-concept [31, 32], the MI method is here refined to image both specular reflectors, corresponding to the boundaries between layers of different propagation velocities, and non-specular reflections generated by a sparse distribution of localized inhomogeneities. The first step consists in retrieving the impulse responses between the geophones from seismic noise cross-correlations [139, 145]. The associated

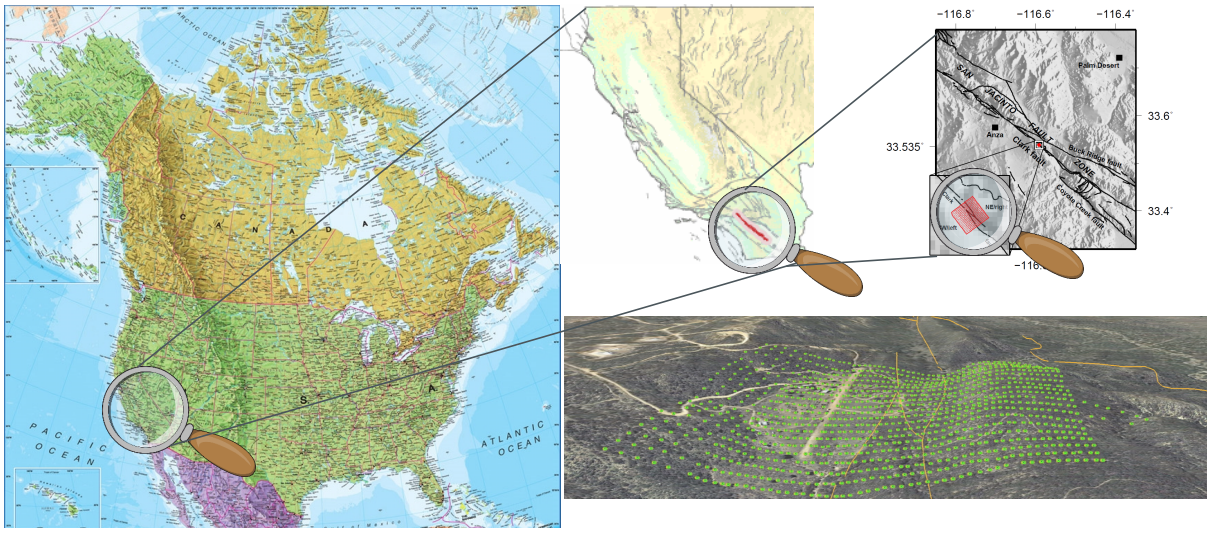

Figure 2.13: Location of the dense geophone array deployed over the Clark fault of SJFZ. The data used in this study has been measured from May 7, 2014 to June 13, 2014 by a spatially dense Nodal array consisting of 1108 vertical geophones straddling the Clark Branch of SJFZ, southeast of Anza [139].

passive reflection matrix is then investigated to image the first few kilometers of the crust by virtue of body waves emerging from noise correlations [38].

Based on a rough estimate of velocity c_0, a double focusing operation is performed both at emission and reception to obtain a broadband reflection matrix $\mathbf{R_{rr}}$ in the focused basis [see Fig. 2.14(a)]. The confocal image extracted from the diagonal of $\mathbf{R_{rr}}$ [Fig. Fig. 2.14(b)] should be considered with caution. The CMP intensity profile $I(\mathbf{r}_m, \Delta r)$ (Eq. 2.3) extracted from $\mathbf{R_{rr}}$ shows a significant spreading of energy over off-diagonal coefficients of $\mathbf{R_{rr}}$. This effect is a direct manifestation of the aberrations sketched in Fig. 2.14(a). Indeed, in absence of aberration, all the back-scattered energy would be contained in a diffraction-limited confocal focal spot [white circle in Fig. 2.14b] whose size δ_0 is dictated by the dimension of the geophone array: $\delta_0 \sim \lambda z/D$ [Fig. 2.17(a)]. Here the characteristic size of the main central lobe is larger and few secondary lobes also emerge in Fig. 2.14b due to the gap between the velocity model and the actual seismic wave velocity distribution in SJFZ.

By projecting the input or output entries of this matrix in the far-field, the distorted component $\mathbf{D}$ of the reflected wave-field can be extracted. A virtual iterative time reversal process is applied to the matrix $\mathbf{D}$ to extract the phase distortions undergone by the incident or reflected wave-fields during their travel from the Earth surface to the focal plane [38]. Mathematically, this process is performed by means of a singular value decomposition (SVD) of $\mathbf{D}$. Because we are in sparse scattering regime, there is then a one-to-one association between each isoplanatic patch and each main eigenstate of $\mathbf{D}$. The phase conjugate of the two first singular vectors, $\mathbf{U}_1^*$ and $\mathbf{U}_2^*$ [Figs. 2.14(d) and (e)], provide the focusing laws that shall be applied to compensate for aberrations over the two main isoplanatic patches. The resulting images of the subsoil reflectivity are displayed in Figs. 2.14 (h) and (i) at $z = 3600$ m over the two main isoplanatic patches. Their comparison with the initial image [Fig. 2.14(c)] illustrates the benefit of the aberration

correction process. The first isoplanatic patch highlights the presence of three distinct reflectors that arise in the vicinity of the fault's surface traces [Fig.2.14(h)]. The second isoplanatic patch yields a highly-resolved image of a coherent reflector on the west of the Clark fault [Fig.2.14(i)].

3.3 High transverse resolution

Compared to the initial image in Fig. 2.14(a), the contrast and resolution are drastically improved [see Fig. 2.14(h) and(i)]. This observation can be confirmed by looking at the corresponding CMP intensity profiles [Figs.2.14(f) and (g)]. The incoherent background is below -35 dB beyond the theoretical transverse resolution cell (white dashed line). Last but not least, the observed lateral resolution is nearly one-eighth of the theoretical limit based on the geophone array aperture [see Fig. 2.15(a)].

A first reason for this striking result could be an overestimation of the wave speed c at shallow depth. This value actually dictates the maximum spatial frequency exhibited by body waves induced at the Earth surface. However, the chosen value $c_0 = 1500$ m/s seems in agreement with P-wave velocity measured in the shallow (<100 m) fault zone at the site under study [146].

Alternatively, the local gradient of the background seismic velocity in the vicinity of the fault can constitute a wave-guide through which seismic waves can be channeled [147]. Reflections on wave guide boundaries can also enlarge the effective array aperture: This is the so-called kaleidoscopic effect [37] [see Fig. 2.15(d)].

A last hypothesis is that the heterogeneous subsoil acts as a lens between the geophones and the focal plane by scattering [see Fig. 2.15(c)]. As in a time reversal experiment, scattering by small-scale heterogeneities can widen the angular aperture of the focused beam [36]. Here the damage area is particularly heterogeneous and can play the role of scattering lens. Moreover, its location near the surface and its finite thickness (~ 1000 m) implies the existence of an angular memory effect even for multiple scattering speckle [92–95]. In that configuration, multiple scattering manifests itself as high-order aberrations associated with relatively small isoplanatic patches. Another potential mechanism could be the conversion of Rayleigh waves into bulk waves that would be induced by scattering by heterogeneities lying at the Earth surface [see Fig. 2.15(b)].

Whether it be by scattering or wave guiding, such high-order aberrations can be corrected by our matrix method in the geophone or plane wave basis, respectively. A recent study by Elsa Giraudat showed that, in the present case, the super-resolution is not observed if distorted wavefields are projected in the geophone basis [see Fig. 2.16(d)]. This justifies *a posteriori* the choice of the plane wave basis for the correction of aberrations. The kaleidscopic effect [Fig. 2.15(d)] is *a priori* the main reason for the super-resolution observed in SJFZ. Beyond this specific case, note that the choice of basis for the aberration correction is flexible. The reflection matrix can be ideally projected onto any aberrating layer in the subsoil. This choice shall be dictated by the local topography and any prior knowledge on the local distribution of seismic wave velocities in the zone under study.

3.4 Structural interpretation of 3D images

Figure 2.16(a,b) compares a slice of the 3D image before and after the MI process. While the raw image $\mathcal{I}_0$ is completely blurred, the gain in horizontal resolution provided by the MI process reveals an image of the SJFZ subsoil with a refined level of details. Based on the surface traces displayed in Fig. 2.13, the fault is expected to spread orthogonally to the x-axis. The choice of the profiles' orientation in Figs. 2.16(a) and (b) is dictated by our willingness to highlight the fault blocks on the right and left side of the slip interface.

The SJFZ is a major continental strike-slip fault system that accumulated through history a significant slip of tens of kilometers. Such large fault systems induce zones of strongly damaged materials [148, and references therein] and the damage is expected to be pronounced in the shallow crust. Thanks to the distortion matrix correction, Fig. 2.16(b) shows the two main signatures of the fault in diffraction imaging. First, it reveals a damage zone associated with a dense distribution of scatterers. The damage volume extends from the surface to 1000 m below with a section decreasing in depth. Second, beyond a depth of 1000 m, the matrix image displays strong echoes associated with the presence of sub-horizontal reflectors. The corresponding strata layers are located at different depths on both sides of the fault. This discontinuity seems to indicate the fault location in depth (see the shaded area in Fig. 2.16), although the damage area is no longer discernible beyond 1000 m. A deeper structural interpretation is provided in Ref.[149].

MI has also been applied recently to the volcano La Soufrirère in Guadeloupe by Elsa Giraudat [39]. This study results from a collaboration with Arnaud Burtin from the Institut de Physique du Globe de Paris. Strikingly, MI also leads to super-resolution in that configuration and numerical simulations seem to indicate that a kaleidoscopic effect [37] due to the lateral variations of the seismic velocity account for the increase of the effective aperture of the geophone array. An endoscopic image of the internal structure of the volcano is therefore obtained and shows a nice agreement with existing conceptual models of La Soufrière [150].

During her PhD thesis [151], Rita Touma also imaged at a much larger scale the structure of North Anatolian Fault ($D = 70$ km, [0.1 0.5] Hz). The scattering structure of the crust and the upper mantle as well as the depth evolution of the Moho are revealed. Contrary to previous local studies performed in the [10-20] Hz frequency bandwidth [38, 39], no super-resolution is here observed since the wave velocity distribution appeared to be much more homogeneous in this lower frequency regime.

All these examples thus show both the efficiency and flexibility of MI to cope with and exploit the heterogeneities of the subsoil at any scale. It also demonstrates the great potential of passive seismic imaging to study the fine structure of active faults and volcanoes in depth from reflected bulk waves. In the following, we will see how these different ideas can be implemented at a much smaller scale in optical microscopy.

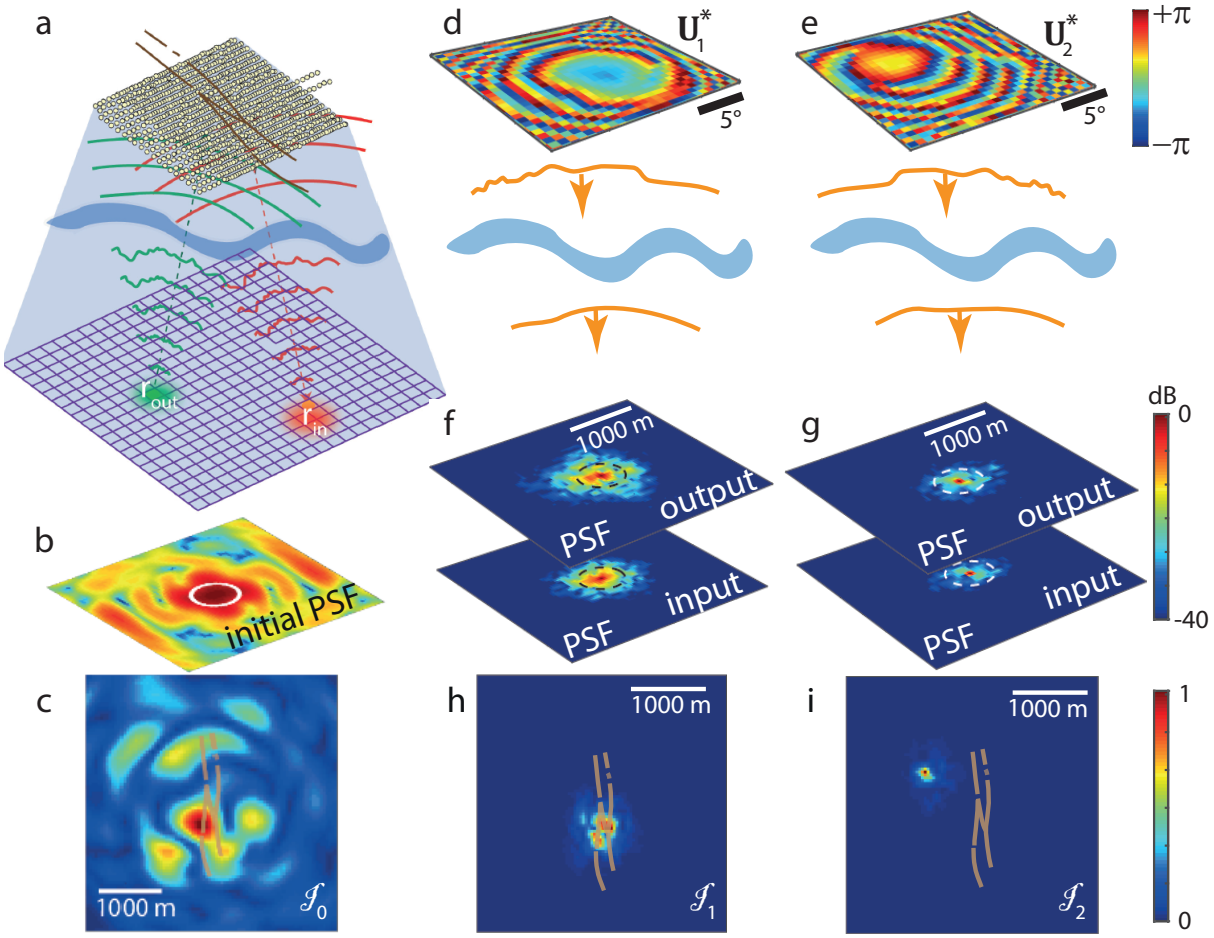

Figure 2.14: Passive MI applied to SJFZ. (a) Adaptive focusing at emission and reception on two points $\mathbf{r}_{\text{in}}$ and $\mathbf{r}_{\text{out}}$ of the focal plane ($z = c_0 t/2$) yields the impulse response between virtual geophones placed at these two points. The same operation is repeated for any couple of points in the focal plane and yields the focused reflection matrix $\mathbf{R_{rr}}$. (b) CMP intensity profile at effective depth z =3600 m. The white circle accounts for the theoretical transverse resolution cell imposed by the geophone array aperture. (c) Confocal image extracted from the diagonal of $\mathbf{R_{rr}}$ at the same depth. (d,e) Aberration phase laws extracted for the first and second isoplanatic patches. (f,g) CMP intensity profiles (color scale in dB) and confocal images, $\mathcal{I}_1$ and $\mathcal{I}_2$, after matrix compensation of aberrations.

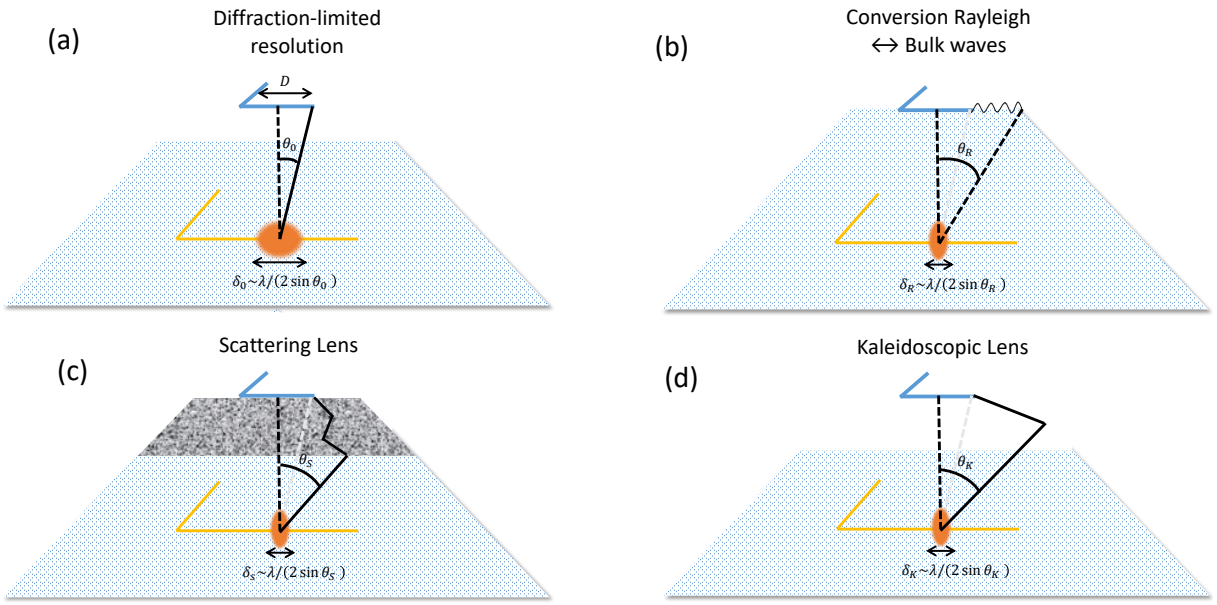

Figure 2.15: Physical mechanisms potentially responsible for the high resolution provided by matrix imaging in SJFZ. (a) In an homogeneous medium, the image resolution δ_0 is dictated by the dimension D of the geophone array. The much finer resolution δ exhibited by the CMP intensity profiles in Figs. 2.14(d) and(e) can be explained by several mechanisms: (b) Conversion of Rayleigh waves into bulk waves by scattering; (c) Multiple scattering paths induced by the heterogeneities of the damage area; (d) Multiple reflection paths or wave guiding induced by a lateral gradient of the seismic wave velocity around the fault.

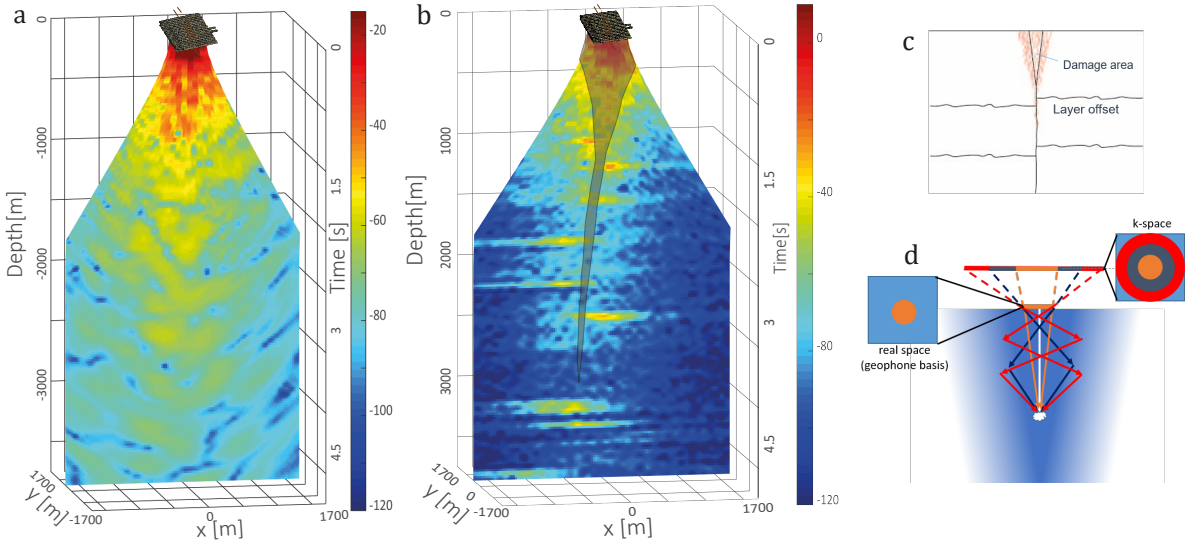

Figure 2.16: Vertical slice of the 3D confocal images before (a) and after (b) application of the MI process. The slice orientation is chosen to be normal to the fault plane. From this image, the fault location can be circumscribed and is represented by the shaded area. The color scale is in dB. (c) Conceptual model of the fault structure. (d) The lateral velocity gradient acts as a wave guide whose transmission matrix can be extracted by investigating the distorted wave-field in the plane wave basis ($\mathbf{k}$).

4 Towards Deep Imaging: Smart Optical Coherence Tomography

For decades, optical microscopy has been a vital tool in biomedical research to observe live specimen with a sub-micron resolution and with minimum invasiveness. Yet, imaging conditions required for such exquisite performances are rarely gathered. For instance, both the resolution and the contrast drop as the imaging depth increases inside a biological tissue. This observation is a consequence of the spatial variations of the specimen refractive index that distort the wavefront of both the incoming and outgoing light. When these variations exhibits low spatial frequencies we use the term aberrations while scattering describes the effect of the higher spatial variations. Both these effects limit the use of conventional microscopy to shallow depths or to semi-transparent specimens. Imaging deeper require to simultaneously compensate for these detrimental phenomena.

Multiple scattering is a particularly difficult challenge with regards to imaging. On the one hand, imaging techniques like diffuse optical tomography [152], acousto-optic [153] or photoacoustic [154] imaging take advantage of the diffuse light to image scattering media in depth but their resolution power is limited. More recently, the memory-effect exhibited by the MS speckle [94, 95] has been taken advantage of to image objects through strongly scattering layers with a diffraction-limited resolution [91–93]. However, it only applies to thin opaque layers as the field-of-view is inversely proportional to the scattering medium thickness. On the other hand, conventional reflection imaging methods provide an optical diffraction-limited resolution but usually rely on a single scattering assumption. The imaging limit of conventional microscopy can be derived from the scattering mean free path ℓ_s. It describes the average distance that a photon travels between two consecutive scattering events. In turbid media, multiple scattering starts to predominate beyond a few ℓ_s. To cope with the fundamental issue of multiple scattering, several approaches have been proposed in order to enhance the single scattering contribution drowned into a predominant multiple scattering background. The first option is to spatially discriminate single scattering and multiple scattering as performed in confocal microscopy [155, 156] or two-photon microscopy [157]. The second option consists in separating SS from MS photons by means of time gating [158]. Probably, the most widely employed coherent time-gated technique is optical coherence tomography (OCT) [77, 159, 160], which is the analogous to ultrasound imaging. It combines scanning confocal microscopy with coherent heterodyne detection [161]. OCT has drastically extended the imaging-depth limit compared to conventional microscopy. Nevertheless, its ability in imaging soft tissues remains typically restricted by a second physical parameter, the transport mean free path. The transport mean free path ℓ_t indicates the mean propagation distance that it takes for photons to, on average, lose relation to the propagation direction they had before entering tissue. In many biological tissues, ℓ_t path is typically ten times larger than ℓ_s. Nevertheless, for a depth between ℓ_s and ℓ_t, forward multiple scattering induce high-order aberrations that one should compensate in order to obtain a reliable image of the sample reflectivity.

To mitigate the aberrations induced by the specimen, the concept of AO has been adapted

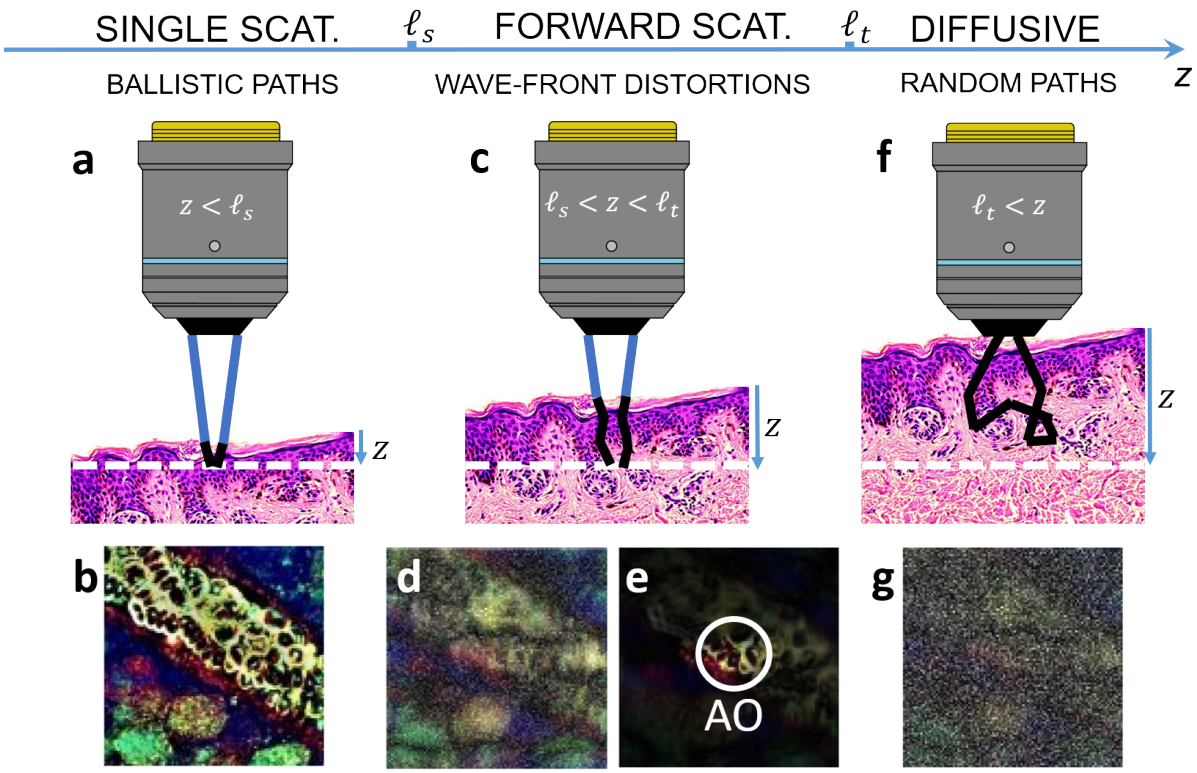

Figure 2.17: Multiple scattering limit for optical microscopy in a reflection configuration. (a) For a penetration depth $z < \ell_s$, single scattering predominates and (b) provides a reliable image of the sample at a diffraction-limited resolution. (b) For $\ell_s < z < \ell_t$, forward multiple scattering induces (d) a loss of resolution and contrast of the image. (e) AO can compensate for these phase distortions but is only effective over an isoplanatic patch. (f) For $z > \ell_t$, the multiple scattering paths follow a random walk and (g) conventional imaging methods fail.

to microscopy from astronomy where it was developed decades ago [162, 163]. Indeed, astronomers faced the same impediment as fluctuations in the atmosphere severely distort the wave-front of the light coming from stars and prevent to obtain a diffraction-limited stellar image. Astronomers then proposed to measure these distortions using a wave-front sensor and to counterbalance it with a dynamic programmable element such as deformable mirrors. Following this concept and the development of deformable mirrors with increasing number of elements, AO already demonstrated its benefits in various imaging techniques such as digital holography [164, 165], confocal microscopy [166, 167], two-photon microscopy [85–87, 168], or optical coherence tomography (OCT) [84, 169]. Unfortunately, AO methods usually require a guide star or are based on an image sharpness metric. Additionnally, there are limited to a small region called the isoplanatic patch, the area over which the aberrations can be considered as spatially-invariant. Therefore, there is a need to extend the field-of-view of AO methods by tackling the case of multiple isoplanatic patches. This issue is particularly decisive for deep imaging where IP size becomes extremely tiny: <10 μm beyond a depth of 1 mm [97].

During the last few years, the reflection matrix $\mathbf{R}$ had been investigated to perform selective focusing/detection in multi-target media [19, 27], energy delivery [104, 170] through strongly

scattering media. With regards to the specific purpose of imaging, the matrix approach has been recently used to implement AO tools in post-processing. The single scattering component of the reflected wave-field through biological tissues has been enhanced in depth by compensating for high-order aberrations [21–23].

4.1 Principle of the distortion matrix in optics

During the PhD theses of Amaury Badon [171] and Victor Barolle [172], we proposed to go beyond a matrix approach of AO by exploiting the distortion matrix concept for deep optical imaging. Unlike previous works in optics that investigated the reflection matrix $\mathbf{R}$ either in the focal plane [27] or the pupil plane [19, 21–23], we thus considered the medium response between those dual bases. To that aim, Amaury Badon and Dayan Li (post-doc) built the experimental set up described in Fig. 2.18(a) [27]. As a first experimental proof-of-concept, we considered a resolution target as the object to be imaged behind a thick layer of biological tissues. A resolution target acts as a specular reflector that enabled us to investigate the properties of the $\mathbf{D}$-matrix in this peculiar regime. In particular, we showed how the $\mathbf{D}$-matrix dramatically highlights the input/output correlations of the wave-field. While the $\mathbf{R}$-matrix exhibits a seemingly random feature in a turbid medium, the $\mathbf{D}$-matrix displays strong field-field correlations over each isoplanatic patch [33].

Several experiments with an increasing order of complexity have been performed to demonstrate the benefits of the $\mathbf{D}$-matrix for optical imaging in turbid media [33]. In particular, we considered an imaging experiment through a turbid non-human primate cornea that induces high-order aberrations (including forward multiple scattering) and a strong diffuse multiple scattering background. By projecting the dual reflection matrix in the focused basis, the CMP intensity profile can be averaged over the field-of-view and displays a highly distorted RPSF, which is a manifestation of high-order aberrations induced by forward multiple scattering events [see Fig. 2.18(c,d)]. The confocal image extracted from the diagonal of $\mathbf{R_{rr}}$ does not show the pattern "3" of the resolution target but an image of speckle without nay connection with the reflectivity of the resolution target.

While the imaging situation seems desperate, the spatial correlations exhibited by the $\mathbf{D}-$matrix can be exploited. In the specular scattering regime, the SVD of the $\mathbf{D}$-matrix actually allows us to decompose the FOV into a set of isoplanatic modes whose degree of complexity increases with their rank (*i.e.*, smaller spatial extent in the focal plane and higher phase distortion in the pupil plane) [see Figs. 2.19(e) and (f)]. The Shannon entropy $\mathcal{H}$ of the singular values allows to define the effective rank of the imaging problem [33]. A combination of the $\mathcal{H}$ first eigenstates yields an image of the focal plane with an excellent contrast and a diffraction-limited resolution as if the medium ahead was made perfectly transparent. This experiment demonstrates the ability of our matrix approach to discriminate between forward multiple scattering paths, which can be taken advantage of for imaging, and the diffuse background, which shall be removed from the final image.

This experimental proof-of-concept was a first step towards real-time deep optical imaging of biological tissues. Nevertheless, it suffered from several limitations. First, we used a negative

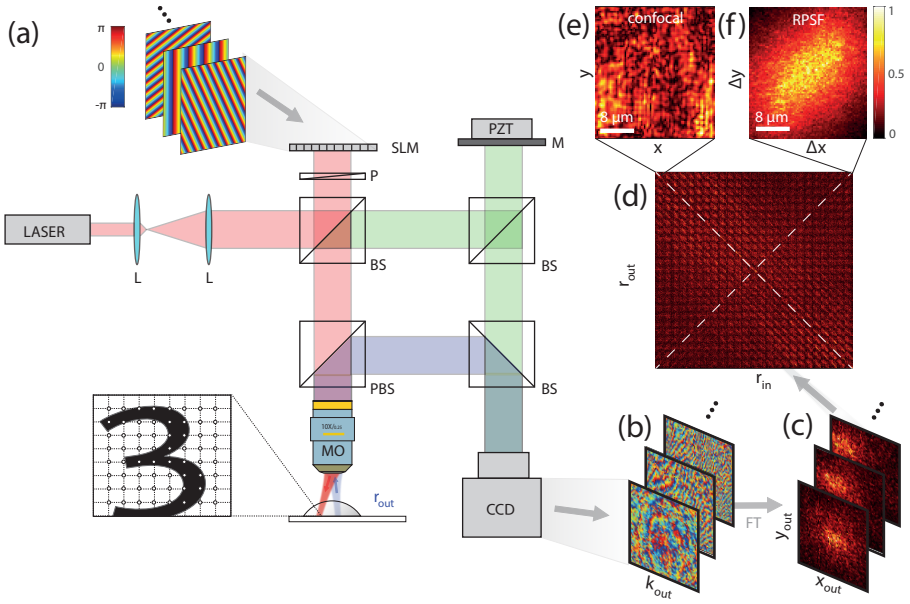

Figure 2.18: Measuring the time-gated dual reflection matrix. (**a**) Experimental set up [27]. A femtosecond laser beam is shaped by an SLM acting as a diffraction grating. A set of incident plane waves is thus emitted from the SLM and focused at a different position in the focal plane of a MO. The backscattered wave-field is collected through the same MO and interferes with a reference beam on a CCD camera. The latter one is conjugated with the back focal plane of the MO. The amplitude and phase of the wave-field is recorded by phase shifting interferometry. The time of flight t is controlled by the length of the interferometric arm and is matched with the position of the focal plane that contains a resolution target positioned below an edematous nonhuman primate cornea. (b) For each input focusing point $\mathbf{r_{in}}$, a reflected wave-field $R(\mathbf{r_{in}}, \mathbf{k_{out}})$ is recorded in the $\mathbf{k}$-space. (c) A 2D Fourier transform yields the wave-field in the real space, $R(\mathbf{r_{in}}, \mathbf{r_{out}})$, where $\mathbf{r_{out}}$ represents the output focusing point in the focal plane. (d) For each incident focusing point $\mathbf{r_{in}}$, the recorded wave-field is stored along a column vector. The set of column vectors finally form the focused reflection matrix $\mathbf{R_{rr}} = [R(\mathbf{r_{in}}, \mathbf{r_{out}})]$. (e) The diagonal of $\mathbf{R_{rr}}$ yields a confocal image of the resolution target that is drastically degraded by aberrations and multiple scattering. (f) This is confirmed by the CMP intensity distribution [Eq. 2.3] that exhibits a highly distorted RPSF that spreads well beyond the diffraction limit (~ 1 px). Figure courtesy of Amaury Badon.

resolution target as the sample to be imaged in this work. The reason is that this highly contrasted object was the ideal specimen to clearly highlight the issue of multiple isoplanatic areas. However, our goal is a direct 3D imaging of biological specimens over large penetration depth. In that perspective, the experimental set up and procedure used in [33] are clearly perfectible. While post-process operations take less than one minute on a regular laptop, the main limitation in this experimental configuration is the acquisition time. In particular, the scanning illumination scheme was not optimized because of the SLM speed but the acquisition time can be drastically reduced by using a galvanometric mirror [23] or an high-speed deformable mirror.

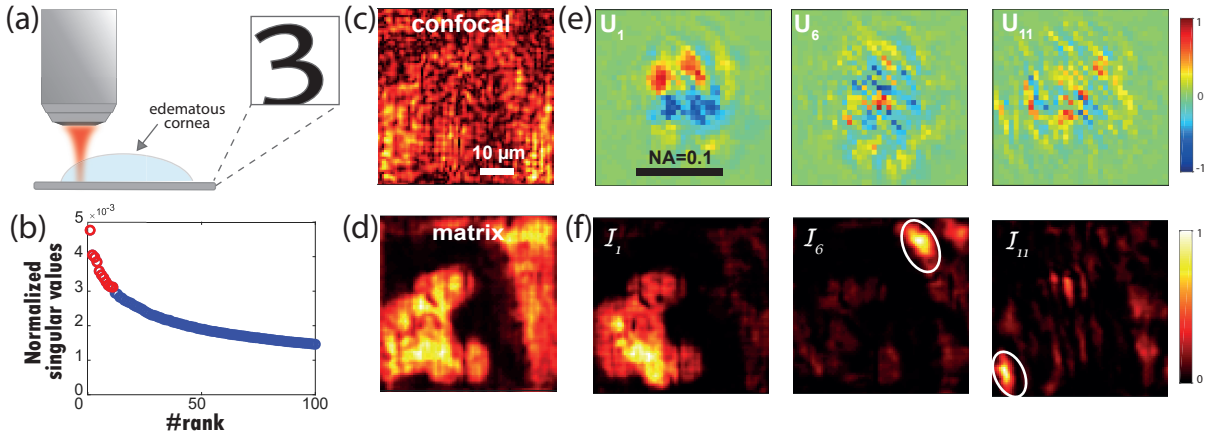

Figure 2.19: Imaging through corneal tissue with deteriorated transparency. (a) Schematic of the experiment. (b) Plot of the normalized singular values of $\mathbf{D}$. The red circles correspond to the eleven first singular values (signal subspace), while the noisy singular values are displayed in blue. (c) Original confocal image deduced from the focused reflection matrix $\mathbf{R_{rr}}$. (d) Final matrix image constructed from the eleven first eigenstates of $\mathbf{D}$. (e) Real parts of the pupil eigenvectors of $\mathbf{D}$ that provide the aberration phase laws. (f) Corresponding isoplanatic modes. Figure extracted from [33].

4.2 Passive matrix imaging: Deep optical microscopy

Another route consists in switching from a scanning to a full-field illumination scheme. Inspired by passive seismic imaging, a measurement of the coherent reflection matrix $\mathbf{R}$ can actually be performed under a spatially incoherent illumination [40, 173]. This full-field configuration enables a recording of the $\mathbf{R}$-matrix over millimetric volumes in a moderate acquisition time. As we will see, this set up allowed us to go beyond the 2D imaging of a specular reflector through biological tissues and provides a 3D image of the biological specimen.

Built by Victor Barolle and Ulysse Najar during their PhD theses, the experimental set up, originally proposed by Claude Boccara, is derived from time domain full-field OCT [174, 175]. It relies on low-coherence interference microscopy. The experimental set up is based on a Michelson interferometer with identical microscope objectives (MO) in both arms, as depicted in Fig. 2.20(b). This configuration is referred to as the Linnik interferometer. In the first arm, a reference mirror is placed in the focal plane of the microscope objective. The second arm contains the scattering sample to be imaged. The same broadband incoherent light source is used to illuminate the entire field of the microscope objectives. Because of the broad spectrum of the incident light, some interferences occur between the two arms provided that the optical path difference through the interferometer is close to zero. The length of the reference arm determines the slice of the sample to be imaged. The backscattered light from each voxel of this slice can only interfere with the light coming from the conjugated point of a reference mirror. The spatial incoherence of the light source indeed acts as a physical pinhole [176]. All these interference signals are recorded in parallel by the pixels of a CMOS or CCD camera in the imaging plane. An axial translation of the sample should then be performed to obtain a volumetric confocal

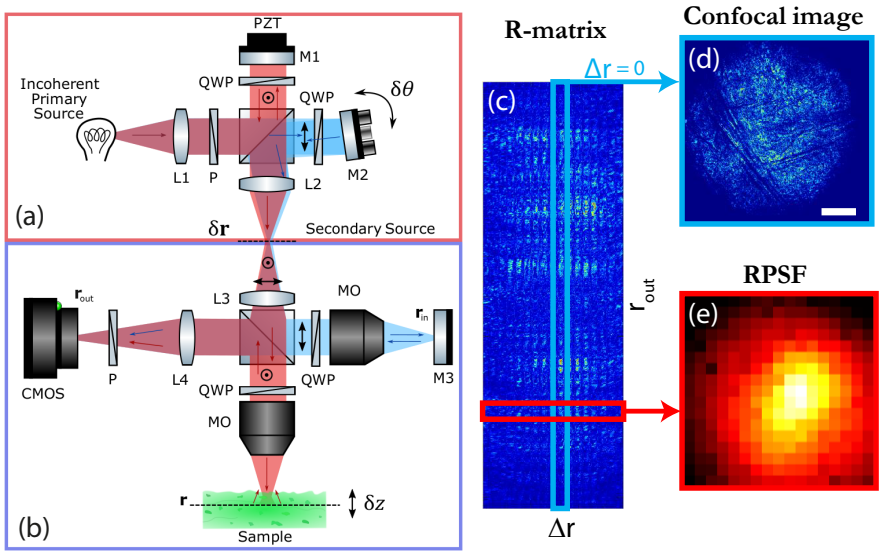

Figure 2.20: Passive measurement of the focused reflection matrix in optical microscopy [172]. The experimental set setup is divided into two building blocks, labelled (a) and (b). The first building block (a) is a Michelson interferometer that separates the incident incoherent wave-field into two orthogonally-polarized paths: a reference path (blue) and a sample path (red). The reference mirror can be tilted by an angle $\Delta\theta$, which equates to a shift of the reference beam by $\mathbf{\Delta r}$ in the secondary source plane. Each beam illuminates the reference and sample arms of a polarized FFOCT set up (b). By means of the polarizer, the reflected beams interfere on a CMOS camera in a plane conjugated with the focal plane inside the sample. The interference signal recorded by each pixel of the camera yields a sub-diagonal of the focused reflection matrix. By scanning $\mathbf{\Delta r}$, one can record the focused reflection matrix $\mathbf{R_{r\Delta r}} = [R(\mathbf{r}_{\text{out}}, \mathbf{\Delta r})]$ in a de-scanned basis. (c) Absolute value of $\mathbf{R_{r\Delta r}}$ recorded at depth $z = 150$ μm of an opaque human cornea. (d) The central column of $\mathbf{R_{r\Delta r}}$ ($\mathbf{\Delta r} = \mathbf{0}$) yields a confocal image of the cornea cross-section. (e) An incoherent average of its lines yields an estimation of the RPSF at this penetration depth. Figure courtesy of Ulysse Najar.

image of the sample.

To go beyond a simple confocal image and record the whole reflection matrix associated with the sample, a Michelson interferometer [Fig. 2.20(a)] is added before the FFOCT apparatus. This interferometer enables to separate the incident beam into two identical incoherent wave-fields shifted by a lateral relative position $\mathbf{\Delta r}$ in the secondary source plane of the FFOCT set up. By a game of polarization, each field illuminates either the reference or the sample arm. As in passive seismology, the cross-correlation between the reflected wave-fields coming from the sample and reference arms provide the impulse response between each point $\mathbf{r}_{\text{out}}$ of the camera and each point $\mathbf{r}_{\text{in}} = \mathbf{r}_{\text{out}} + \mathbf{\Delta r}$ in a conjugated source plane [40, 173] [see Fig. 2.20(c)]. The reflection matrix is thus recorded in a de-scanned basis, *i.e* sub-diagonal by sub-diagonal. This de-scanned matrix is denoted as $\mathbf{R_{r\Delta r}} = [R(\mathbf{r}_{\text{out}}, \mathbf{\Delta r})]$, with $\mathbf{\Delta r} = \mathbf{r}_{\text{in}} - \mathbf{r}_{\text{in}}$. A de-scanned basis is much more efficient than scanning the whole field-of-view with a focused beam as performed previously with a coherent optical set up [Fig. 2.18]. Indeed, the number of interferograms that should be acquired scales as the number of resolution cells contained in the aberrated focal spot.

As a first experimental proof-of-concept, the set up is employed to image an opaque human

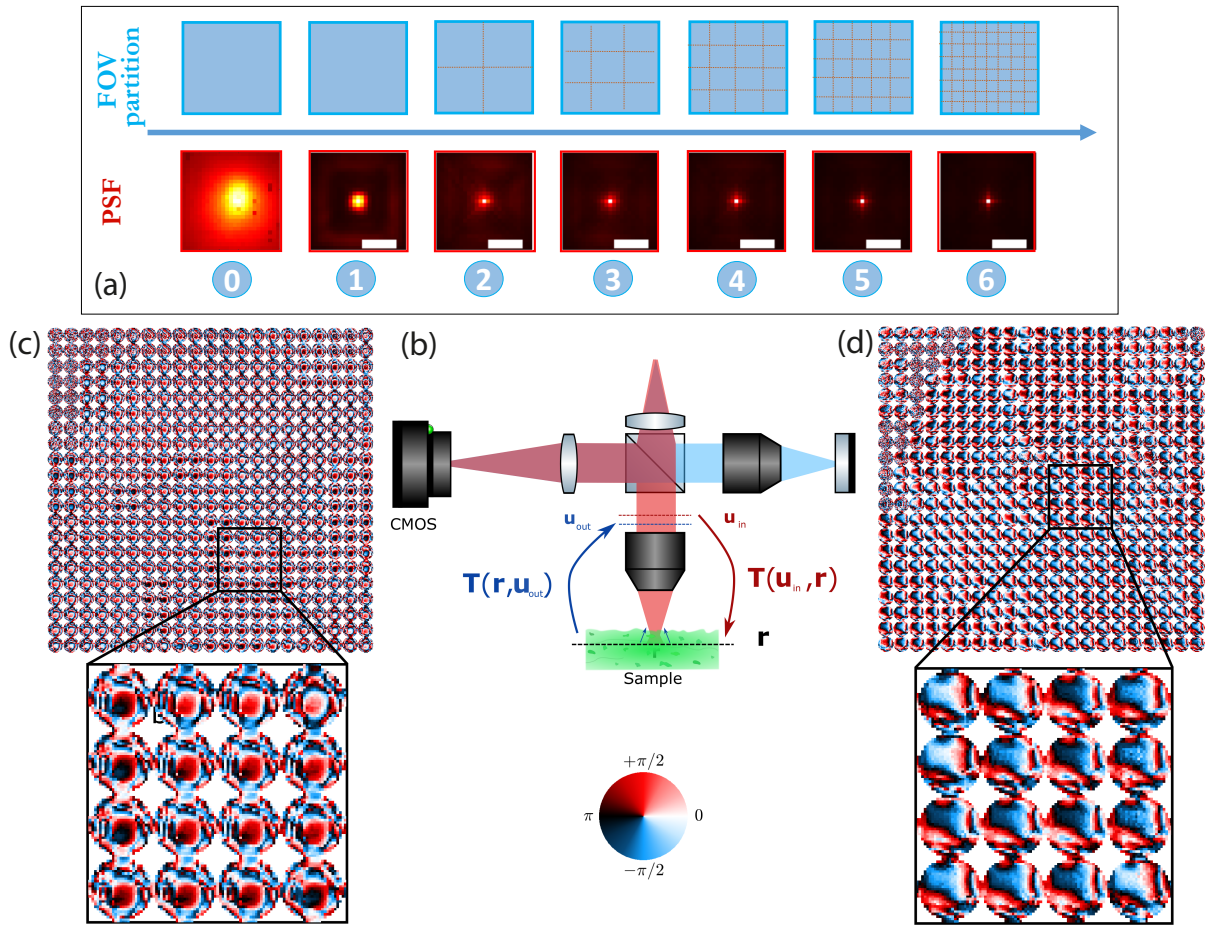

Figure 2.21: Local distortion matrix analysis. (a) Field-of-view partition and RPSF obtained at each iteration of the MI process. (b) The input and output transmission matrices, $\mathbf{T}_{\text{in}}$ and $\mathbf{T}_{\text{out}}$, contain the impulse responses $T(\mathbf{u}_{\text{in/out}}, \mathbf{r})$ between each the input/output pupil plane ($\mathbf{u}_{\text{in/out}}$) and the focal plane ($\mathbf{r}$). (c,d) Aberration phase laws extracted from the input and output transmission matrices at the end of the MI process. Figure courtesy of Ulysse Najar.

cornea. Once the focused $\mathbf{R}-$matrix is measured [Fig. 2.20(c)], an estimator of the RPSF can be computed by an incoherent average of each de-scanned wave-field [Fig. 2.20(e)]. Not surprisingly, the turbuidity of the cornea gives rise to a highly distorted RPSF. The confocal image extracted from the central column of $\mathbf{R}_{\mathbf{r}\Delta\mathbf{r}}$ ($\Delta\mathbf{r} = \mathbf{0}$) should thus be considered with caution [Fig. 2.20(d)] since high-order aberrations and forward multiple scattering events prevent from a reliable estimation of the cornea reflectivity at this depth.

To compensate for these issues, a local distortion matrix analysis can be performed as already described for ultrasound MI [35]. By gradually reducing the size of the targeted isoplanatic patches, aberrations are compensated step by step, as evidenced by the refinement of the RPSF at each step of the process [Fig. 2.21(a)]. A set of aberration phase laws [see Fig. 2.21(c,d)] is finally obtained and constitutes our estimator of the input/output transmission matrix that links each voxel with the input/output pupil plane [Fig. 2.21(b)]. Note that the input and output transmission matrices differ probably because the secondary source plane in Fig. 2.20 is not strictly conjugated with the focal planes of the microscope objectives.

The phase conjugate of each **T**-matrix provide the optimal input and output focusing laws for each pixel of the image. Two cross-sectional views (B-scan) of the 3D image are displayed in Fig. 2.22(b) and compared to the initial FFOCT image [Fig. 2.22(a)]. While standard FFOCT fails to image the opaque cornea beyond a depth of 90 μm, MI manages to image its entire thickness (350 μm). Original and MI en-face images are displayed in Figs. 2.22(c) and (d), respectively. The contrast gain is drastic [Figs. 2.22(e)], especially at z=250 μm where it can reach a value of 25 in intensity. While the original FFOCT image is very noisy due to a high level of aberrations, MI enables to recover a high contrast and a diffraction-limited resolution. At $z = 150$ μm, stromal striae (indicator of keratoconus) are also revealed by MI.

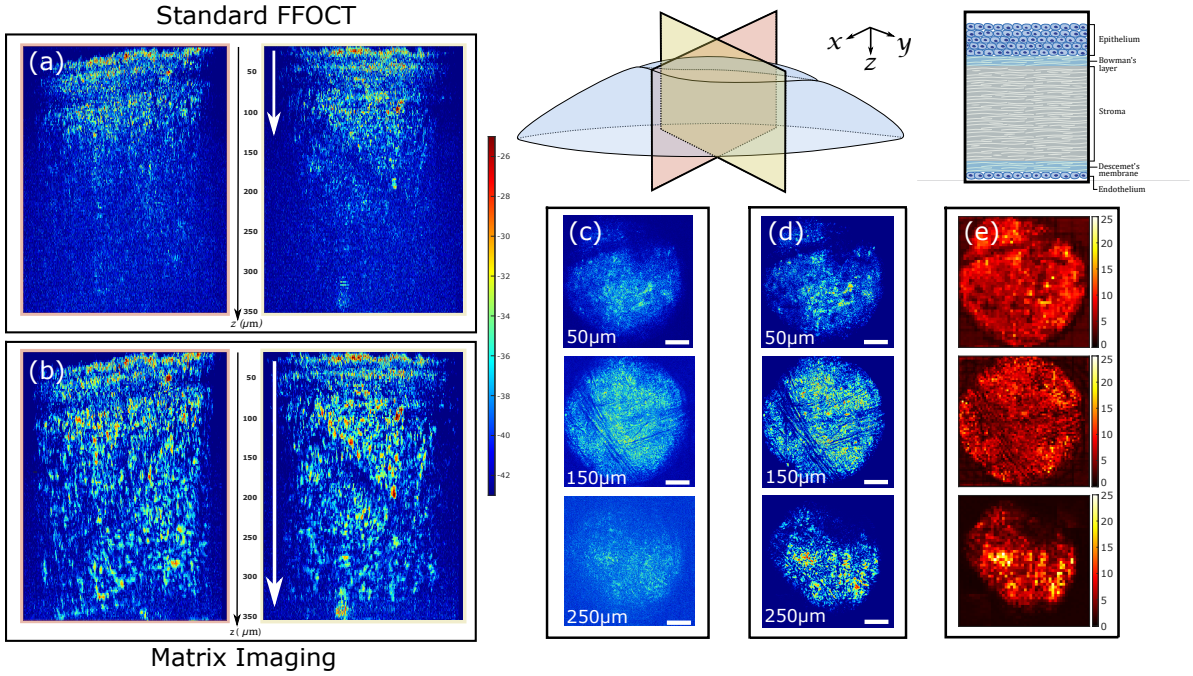

Figure 2.22: Three-dimensional matrix imaging of the opaque cornea. (a,b) Cross-sectional views (B-scan) of the cornea, before and after the MI process, respectively. (c,d) En-face images of the cornea at different depths, before and after the MI process, respectively. (e) Confocal gain provided by the MI process at the corresponding depths. Figure courtesy of Ulysse Najar.

As also demonstrated by closely related works based on the CLASS algorithm [22, 23], the reflection matrix opens a new route toward deep optical imaging of biological tissues. Nevertheless, these studies have been so far based on the recording of a time-gated reflection matrix. An axial translation of the sample is thus required to obtain its volumetric image which drastically increases the acquisition time. The capabilities of the existing set ups are therefore limited for in-vivo and real-time applications.

4.3 The Matriscope: Ultra-fast acquisition of a polychromatic reflection matrix

To circumvent this problem, Paul Balondrade developed during his PhD thesis a novel apparatus, the so-called Matriscope, dedicated to ultra-fast 3D MI [177]. This set up is inspired from Fourier

domain full-field OCT (FD-FFOCT) that uses a swept laser source [178] instead of broadband light. Working in the Fourier domain implies a much better sensitivity since the signal-to-noise ratio scales as the number of independent wavelengths over which the FFOCT signal is recorded [179–181]. High-speed cameras can then be used to reach almost real time volumetric imaging [182, 183]. Structured [184] or spatially-incoherent [185] illuminations can then be used to maintain the confocal gate of the original FFOCT scheme [174, 175] and filter most of multiple scattering background.

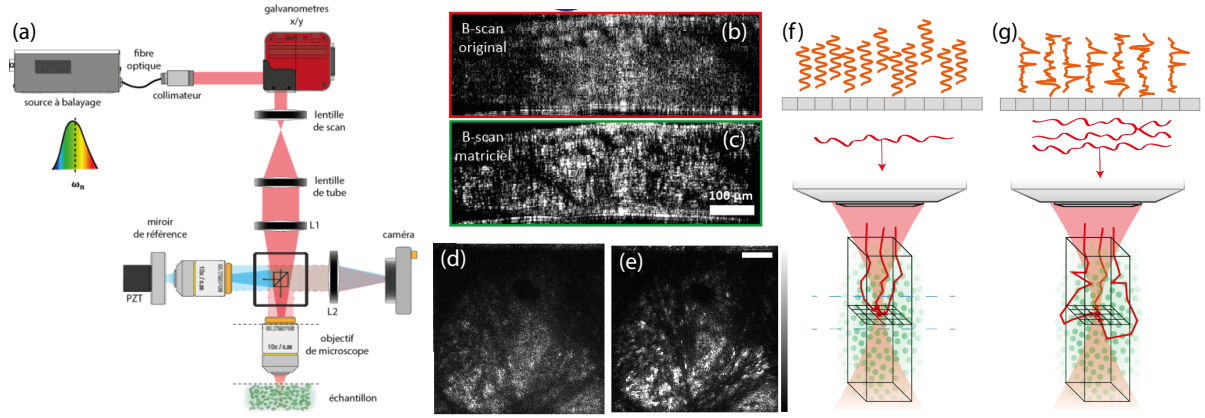

Figure 2.23: Principle of the matriscope and application to the imaging of an opaque cornea. (a) Experimental set up. (b,c) Cross-sectional views (B-scan) of the cornea, before and after the MI process. (d,e) En-face images of the cornea at a depth of 100 μm, before and after the MI process, respectively. (f) Spatial compensation of aberrations. (g) Spatio-temporal compensation of multiple scattering phenomena. Figure courtesy of Paul Balondrade.

With Paul Balondrade and Victor Barolle, we drew on swept-source full-field OCT (SS-FFOCT) to develop an interferometric microscope combining a sequence of illuminations of a sample over a wide range of optical frequencies in order to measure a polychromatic reflection matrix in record time [see Fig. 2.23(a)]. The so-called Matriscope is the optical equivalent of the ultra-fast imaging platform developed at the Langevin Institute in the late 2000s and that revolutionized the field of ultrasound imaging with a frame rate 200 times higher than conventional systems [110]. In optics, in contrast with previous works that recorded the reflection matrix at a single frequency [19] or time-of-flight [21, 23, 27], this polychromatic reflection matrix allows to realize in post-processing: (i) a 3D confocal image of the sample reflectivity on millimeter volumes (1 mm^3 = 10^9 pixels) in an ultra-fast acquisition time (1 s) [see Fig. 2.23(b,c)]; (ii) a matrix correction of the aberration and multiple scattering problems that are currently the fundamental limits of microscopy [see Fig. 2.23(d,e)]. Compared to a time-gated reflection matrix that only allows the compensation of transverse aberrations (lateral variations of the optical index) [see Fig. 2.23(f)], the polychromatic reflection matrix gives access to many temporal degrees of freedom that can be exploited for compensating the distortions of the coherence volume (axial aberrations). In the future, it will be exploited for overcoming the multiple scattering limit in optical microscopy since it will enable the tailoring of complex spatio-temporal focusing laws that are required to focus light in depth whether it be numerically in post-processing or

physically with wave-front shaping techniques [see Fig. 2.23(g)]. The ultimate goal will be to extract a time-dependent transmission matrix between the source/imaging planes and the voxels inside the medium [Fig. 2.2(b)]. In the next chapter, we will present the first steps towards this ambitious goal but also alternative routes for target detection and imaging in a multiple scattering regime.

5 Perspectives

5.1 Dynamic Matrix Imaging

Beyond the fundamental multiple scattering issue, another problem we have not considered yet is the movement of the medium during the acquisition of the reflection matrix. Of course, the assumption of a static medium is everything but true especially for in-vivo applications. In optical imaging, we often have to deal with dynamic scattering media. This is the case for optical microcopy in which living tissues exhibit a decorrelation characteristic time ranging from 50 ms to 2.5 s depending on the level of immobilization [186]. This is also the case for ultrasound imaging despite plane wave illumination that enables ultra-fast measurement of the **R**-matrix. At last, in seismology, passive MI also implies the cross-correlation of seismic noise recorded over several months. Yet tides and temperature changes, for instance, can induce seismic velocity changes at a sub-daily time scale.

To cope with the dynamic features of the medium, two strategies can be followed. The first one is to limit the measurement time of the **R**-matrix at its minimum, as shown in the previous section. The second one is to develop algorithms that consider the movement of the medium during the measurement of the **R**-matrix. Yet, for deep imaging, the latter number should be high in order to harness all the multiple scattering paths that the wave can undertake to focus deep inside the medium. Hence, a dynamic matrix approach of wave imaging is required for deep imaging. The movement of the medium can be characterized during the illumination sequence by cross-correlating each output image. Movement can then be compensated in order to build a beamforming adapted to the object trajectory.

On the other hand, moving speckle can also be taken advantage of to optimally extract the **T**-matrix between sensors and medium voxels from reflection measurements. Moving speckle actually gives access to large number of speckle realizations at each voxel which can be used in return to extract an aberration phase law for each voxel of the medium without relying on any isoplanatic assumption [187]. Thereby, we will have access to a highly-resolved **T**-matrix which is the Holy Grail for wave imaging.

At last, dynamic scattering can be used to reveal a novel contrast for imaging for characterizing the dynamics of tissues in biomedical imaging [188]. Such a contrast is also particularly relevant for monitoring the movement of fluids in volcanoes [189], the variations of mechanical properties of the subsoil in fault zones [190] or the inner dynamics of a glacier [191].

At a larger time-scale, the temporal variation of the **R**-matrix can be leveraged to discriminate and map the movement in each part of the volume to be imaged. To that aim, the generalized Wigner Smith operator [192] can be a powerful tool. Compared to state-of-the-art

methods that consists in speckle tracking on images, such an approach would rely on an analysis of the back-scattered wave-field that is *a priori* much more sensitive to the dynamics of the medium.

5.2 Nonlinear Matrix Imaging

Finally, we plan to extend the **D**-matrix approach to non linear imaging. Harmonic ultrasound imaging is, for instance, widely used by clinicians as it often provides a better contrast and resolution. As developed so far, MI cannot be directly applied to this imaging mode as it relies on linearity of the wave equation. Nevertheless, the focused **R**-matrix can still be of interest for optimising harmonic tissue imaging [193]. Firstly, an aberration correction or a better wave velocity model can optimize the focusing process and a more efficient non-linear conversion in the focal spot. Second, a non-linear reflection matrix linking, for example, input focusing points at the fundamental frequency and output focusing points at a harmonic frequency can be a relevant tool to optimize the non-linear conversion process and the resolution of the harmonic image. In optics, several works started to exploit the matrix formalism to describe fluorescence imaging under structured illumination. For instance, Boniface *et al.* [194] extracted, from incoherent measurements, the transmission matrix to and from a fluorescent object buried inside a scattering medium. Idier *et al.* [195] used a matrix formalism to describe structured illumination microscopy and relates the output intensity with a set of input illuminations. In the next few years, our aim is to explore how the $\mathbf{D}-$matrix concept can be extended to deep imaging with both linear and non-linear contrast mechanisms.

CHAPTER 3

Matrix Beamforming and Imaging in the Multiple Scattering Regime

Publications

- S.M. Popoff, A. Aubry, G. Lerosey, M. Fink, A.C. Boccara, and S. Gigan, *Exploiting the time-reversal operator for adaptive optics, selective focusing, and scattering pattern analysis*, Phys. Rev. Lett. **107**, 263901 (2011)
- S. Shahjahan, A. Aubry, F. Rupin, B. Chassignole, and A. Derode, *A random matrix approach to detect defects in a strongly scattering polycrystal: How the memory effect can help overcome multiple scattering*, Appl. Phys. Lett. **104**, 234105 (2014)
- A. Badon, D. Li, G. Lerosey, A. C. Boccara, M. Fink, A. Aubry, *Smart optical coherence tomography for ultra-deep imaging through highly scattering media*, Sci. Adv. **2**, e1600370 (2016)
- A. Badon, A. C. Boccara, G. Lerosey, M. Fink, and A. Aubry, *Multiple scattering limit in optical microscopy*, Opt. Express **25**, 28914-28934 (2017)
- T. Blondel, J. Chaput, A. Derode, M. Campillo, and A. Aubry, *Matrix Approach of Seismic Imaging: Application to the Erebus Volcano, Antarctica*, J. Geophys. Res.: Solid Earth **123**, 10936-10950 (2018)

Multiple scattering of waves in disordered media is usually seen as a nightmare whether it is for detection or imaging purposes. So far, the best approach to get rid of multiple scattering is to combine confocal imaging and time gating to enhance the weight of singly-scattered waves. Nevertheless, the imaging-depth range remains limited to one transport mean free path ℓ_t at best. In this Chapter, we propose several approaches to push back this fundamental limit. The first strategy is to use a prior information on the object we want to retrieve. For point-like bright targets, we can combine a matrix discrimination of singly-scattered waves and iterative time reversal , or equivalently, an eigenvalue decomposition of the time reversal operator $\mathbf{R}\mathbf{R}^\dagger$. For more complex targets, one can exploit the spatio-temporal degrees of freedom exhibited by the target reflection matrix $\mathbf{R}_0$. To do so, we introduce a novel target-specific operator $\mathbf{R}\mathbf{R}_0^\dagger$. This operator is the basis of a fingerprint matrix beamformer that yields an image of the likelihood index of the target presence. Beyond target detection, we will finally draw our future strategy to address the imaging problem in the multiple scattering regime. To that aim, the $\mathbf{D}$-matrix introduced in the first Chapter will be a key tool. It will be investigated beyond the ballistic time to tailor the complex spatio-temporal focusing laws that are required to focus waves in the multiple scattering regime. The scientific challenge will lie in the absence of isoplanicity at those depths. To overcome this issue, inversion algorithms and/or learning based methods will be relevant tools to unscramble the different scattering orders of the $\mathbf{T}$-matrix from a Born decomposition of the $\mathbf{R}$-matrix.

1 Multiple scattering filter and Iterative time reversal

During my PhD thesis, we developed with Arnaud Derode a matrix method to separate the single scattered echo of the target from the multiple scattering background [18, 24] [see Fig. 3.1]. This

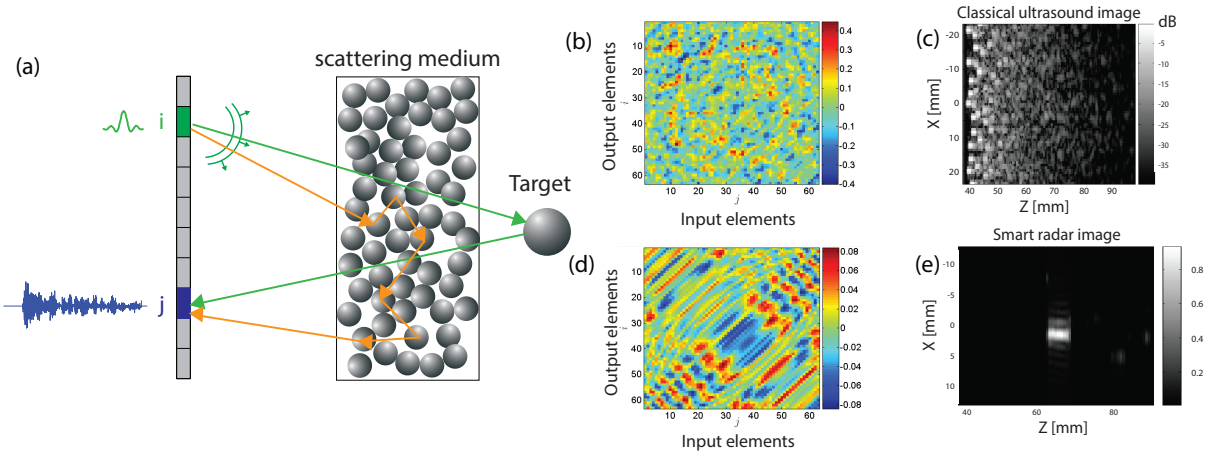

Figure 3.1: Experimental set up for the recording of the reflection matrix in a canonical basis. (b) Example of the real part of a reflection matrix when the multiple scattering contribution is predominant. (c) Conventional ultrasound image built from $\mathbf{R}$. (d) Real part of the extracted single scattering contribution $\mathbf{R}_S$. (e) Image of the target deduced from the DORT method applied to $\mathbf{R}_S$.

was done by taking advantage of the deterministic coherence of the back-scattered wave-field

which is characteristic of single scattering and related to the memory effect [see Fig. 3.2]. Once

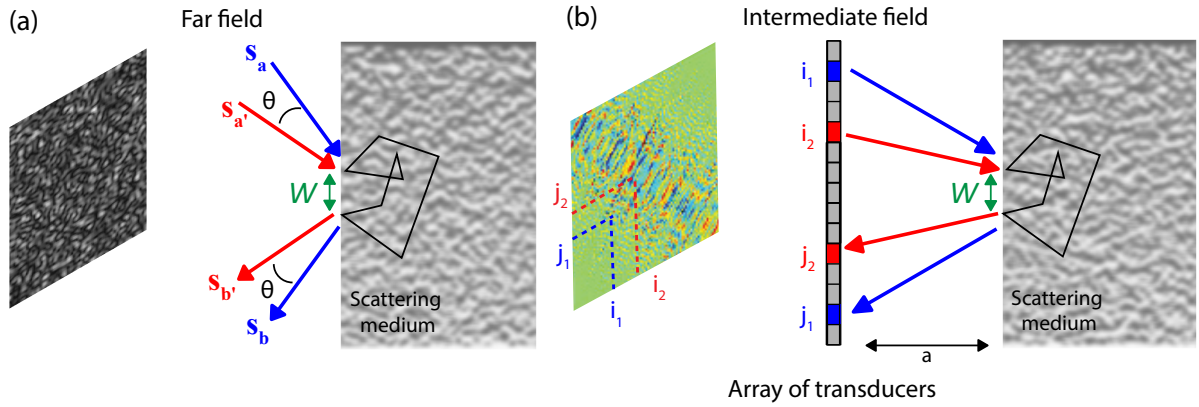

Figure 3.2: Memory effect in reflection. (a) Memory effect in optics (illumination and recording of the reflected wave-field from the plane wave basis): When an incident plane wave is tilted by an angle θ, the speckle wave-field reflected by the scattering layer is tilted by the opposite angle $-\theta$. The correlation width $\Delta\theta$ scales as λ/W, with W the mean distance between the first and last scattering events in the scattering layer. (b) Memory effect in acoustics (array of transducers placed at a finite distance a from the sample): The memory effect manifests itself along the antidiagonals of the reflection matrix. The correlation length scales as $\lambda a/W$.

this operation is performed, target detection is achieved by applying the DORT method (French acronym for decomposition of the time reversal operator). Initially developed for ultrasound [15, 100] and then extended to microwaves [101, 196] and optics [19], the DORT method (French acronym for Decomposition of the Time Reversal Operator) takes advantage of the reflection matrix to focus iteratively by time reversal processing on each scatterer of a multi-target medium even in presence of strong aberrations. Coupled to a multiple scattering filter, the DORT method can lead to the detection of targets at a penetration depth of 3 ℓ_s using a linear array of transducers. During the last ten years, we first applied this approach for the detection of flaws embedded deeply into a polycrystalline materials [25].

Since then, we generalized this approach by implementing the multiple scattering filter in the focused basis introduced in Chapter 2. Interestingly, the focused basis appears more flexible compared to the canonical one. Indeed, the time-gating operation in this basis enables an optimal selection of singly-scattered echoes associated with reflectors located at a given depth. Furthermore, it does not require any paraxial approximation on which relied the initial method [24]. In the following, we show the application of this approach to: (*i*) optical microscopy with the detection of targets through a multiple scattering medium [27] [Fig. 3.3(a)]; (*ii*) seismic imaging by considering the the extreme case of the Erebus volcano in Antarctica [28], in which the scattering mean free path ℓ_s for body waves is smaller than their wavelength λ. In each case, our matrix approach allows us to push back the multiple scattering limit to a depth of $12\ell_s$, extending by at least a factor 2 the penetration depth of conventional reflection imaging methods [29].

1.1 Ultra deep optical detection through turbid media

Inspired by our previous works in ultrasound imaging through strongly scattering media [18, 24, 25], we proposed a matrix approach of optical imaging to push back the fundamental limit of multiple scattering. Experimentally, this approach relies on the measurement of a time-gated reflection matrix from the scattering medium [see Fig. 2.19]. The multiple scattering filter consists in filtering the focused reflection matrix $\mathbf{R_{rr}}$ [Fig. 3.3(e)], as follows:

$$R_S(\mathbf{r_{out}}, \mathbf{r_{in}}) = R(\mathbf{r_{out}}, \mathbf{r_{in}}) \times \exp\left(-|\mathbf{r_{in}} - \mathbf{r_{out}}|^2 / l_c^2\right) \tag{3.1}$$

l_c is a tunable parametric length that accounts for the fact that the ballistic signal does not only emerge along the diagonal of the $\mathbf{R}-$matrix but also along off-diagonal elements. l_c is governed by two factors: (*i*) the coherence length of the singly-scattered wave-field in the focal plane that is degraded by aberrations; (*ii*) the size of the target. Equation 3.1 thus consists in keeping the diagonal and closed-diagonal coefficients of $\mathbf{R_{rr}}$ where the single scattering contribution arises and filtering the off-diagonal elements of $\mathbf{R_{rr}}$ mainly associated with the multiple scattering contribution. It can be seen as a digital confocal operation with a virtual pinhole mask of size l_c [197]. The result is displayed in Fig. 3.3(f). $\mathbf{R}_S$ contains the single scattering contribution as wanted plus a residual multiple scattering contribution [see the comparison with the reference matrix in Fig. 3.3(d)]. This term persists because MS signals also arise along and close to the diagonal of $\mathbf{R_{rr}}$. Compared to a single/multiple scattering separation performed in the far-field [18, 21], a single scattering projection in a point-to-point basis [Eq.3.1] is much more flexible since the tunable parameter l_c can be adapted as a function of the aberration level or the expected target size.

Once $\mathbf{R}_S$ is obtained, one can apply the DORT method. Mathematically, the time-reversal invariants can be deduced from the eigenvalue decomposition of the time reversal operator $\mathbf{R}\mathbf{R}^\dagger$ or, equivalently, from the singular value decomposition of $\mathbf{R}$ (the superscript $\dagger$ stands for transpose conjugate). A one-to-one association between each eigenstate of $\mathbf{R}$ and each scatterer does exist. On the one hand, the eigenvectors of $\mathbf{R}$ allow selective focusing and imaging of each scatterer. On the other hand, the associated eigenvalue directly yields the scatterer reflectivity. Nevertheless, this one-to-one association is only valid under a SS approximation. Hence the DORT method cannot be applied to the raw matrix $\mathbf{R}$ since it contains an extremely predominant MS contribution. The trick here is to take advantage of the single scattering matrix $\mathbf{R_S}$.

An eigenvalue decomposition of $\mathbf{R}_S\mathbf{R}_S^\dagger$ is performed. Fig. 3.3(c) displays the histogram of the eigenvalues σ_i^2 normalized by their average. It is compared to the distribution that would be obtained in a fully multiple scattering regime. The histogram of $\sigma_i^2 / < \sigma_i^2 >$ in Fig. 3.3(c) follows this distribution except for the largest eigenvalue σ_1^2. The latter one is actually beyond the superior bound of the multiple scattering continuum of eigenvalues. This means that the first eigenspace is associated with the target [18, 25, 26]. The first eigenvector, $\mathbf{U}_1$, forms the smart-OCT image displayed in Fig. 3.3(f). The image of the target is nicely recovered. The comparison with the *en-face* OCT image displayed in Fig. 3.3(e) unambiguously demonstrates

the benefit of smart-OCT in detecting a target in the deep multiple scattering regime ($L = 12.25$ l_s). Note that the target image does not match exactly with the reference image [Fig. 3.3(a)]. This difference can be accounted for by residual aberration effects induced by the scattering layer itself.

In parallel of this experimental demonstration, we performed a theoretical study that consisted in predicting the evolution of the single-to-multiple scattering ratio and the penetration depth for different optical imaging techniques [29]. In the conditions of the reported experiment, the imaging thickness-limit (SMR$\sim$ 1) is found to be of $1.5\ell_s$ for conventional microscopy, $3.5\ell_s$ for confocal microscopy and $7\ell_s$ for OCT. This explains the failure of OCT in detecting the target [Fig. 3.3(e)]. On the contrary, the predicted imaging-thickness limit is of $12\ell_s$ for the smart-OCT approach. This accounts for the successful detection of the target in our experimental configuration [Fig. 3.3(f)]. Our approach goes beyond OCT as it involves a subsequent iterative time-reversal processing of the reflection matrix. It results in an additional gain in SMR that scales with N, the number of input wave-fronts. If $N \sim 10^6$, this could lead to a detection-depth limit of $20\ell_s$. Such an imaging improvement is drastic if we keep in mind that the ballistic contribution decreases by a factor $\exp(-2L/\ell_s)$ in a reflection configuration. The smart-OCT approach is thus particularly suited for ultra-deep target detection. Of course, a trade-off will have to be made in practice between the imaging depth and the measurement time that also scales linearly with N. Note also that the imaging depth can be limited by the dynamic range of the CCD camera. For instance, a dynamic range of 75 dB would be required to reach the theoretical imaging depth-limit of $20\ell_s$.

1.2 Deep imaging in geophysics: The Erebus volcano

Beyond target detection though a multiple scattering layer, one can wonder whether this method can be applied to imaging highly scattering media. As a proof-of-concept, we thus applied the developed method to passive seismic imaging, and more precisely to the imaging of volcanoes. Indeed, volcanoes are among the most challenging media for seismic imaging given their highly localized and abrupt variations in physical parameters, extreme landforms, extensive fractures and the additional presence of magma and other fluids. In that respect, the case of the Erebus volcano is extreme since the scattering mean free path ℓ_s for body waves is smaller than their wavelength λ in the 1-4 Hz bandwidth [198].

To do so, we take advantage of a high-density network of 76 seismographs that was deployed on the upper plateau of the volcano as part of the TOMO-Erebus project (2007-2009) [Fig. 3.4(a)]. The coda generated by shallow icequakes [199] is used to retrieve the vertical component of the Green's functions between the geophones. The associated reflection matrix is then investigated for imaging purposes following the same method that we developed for optical microscopy [27]. As a whole, the process can be summarized as a combination of four building blocks:

- (B1) Based on a rough estimate of wave velocity c, a focused reflection matrix is built at each depth z [Fig. 3.4(b)]. As displayed in Fig. 3.5(b), $\mathbf{R_{rr}}$ exhibits a strong off-diagonal energy induced by aberrations and multiple scattering events.

- (B2) An Adaptive confocal filtering enables the removal of most of the multiple scattering contribution [Fig. 3.5(c)].
- (B3) Iterative time reversal (*i.e* DORT method) is applied to overcome the residual multiple scattering contribution as well as the aberration effects induced by the scattering medium itself, and detect possible reflectors [Fig. 3.5(d)].
- (B4) A statistical analysis of the matrix singular values [Fig. 3.5(e)] permits attribution of a likelihood index to each detected structure [24, 26] [Fig. 3.6(b)].

As a result of these four steps, we are able to push back the multiple scattering limit beyond 10 ℓ_s and an image of the internal structure of the Erebus volcano is obtained [Fig. 3.6(b)]. While conventional migration methods lead to a fully blurred image due to multiple scattering [Fig. 3.6(a)], the matrix approach developed here manages to detect internal structures in a reliable way, and reveal a chimney-shaped structure feeding the lava lake that bifurcates sharply towards the north-west and then seems to set centrally in a shallow magma chamber near 2500 m elevation. Some particular features also emerge from the sea level to 5000 m below it. A structural interpretation of the obtained image is finally built on the existing literature about Erebus [28].

Beforehand, however, it should be noted that the velocity model used for emission and reception is a bulk approximation and thus the depth is likely to be inaccurate. Yet a correct model would dilate the structure up or down but would not change significantly its geometrical shape. One great advantage of iterative time reversal is the ability to detect scatterers in presence of the strong wave-front distortions. However, the associated image still suffers from aberrations and multiple reverberations as the wave velocity model used for the back-propagation is inaccurate. A perspective of this work will be to tackle these aberration issues by coupling the current method with the distortion matrix approach presented in Chapter 1. A first step will be to incorporate the existing wave velocity model over the first km depths [200], before improving and extending it to larger depths thanks to the distortion matrix approach. The removal of multiple reflections due to geological layering is also a challenge [201]. A solution will be proposed further by investigating the distortion matrix beyond the ballistic time. Another limit of the current method is the iterative time reversal process. It assumes that the rank of the target subspace is of rank 1. Yet this is only true if the object can be considered as point-like and non-resonant [202, 203]. To go beyond and adapt the detection process to the complex spatio-temporal signature of any target, an optimal matrix beamforming process is proposed in the next section.

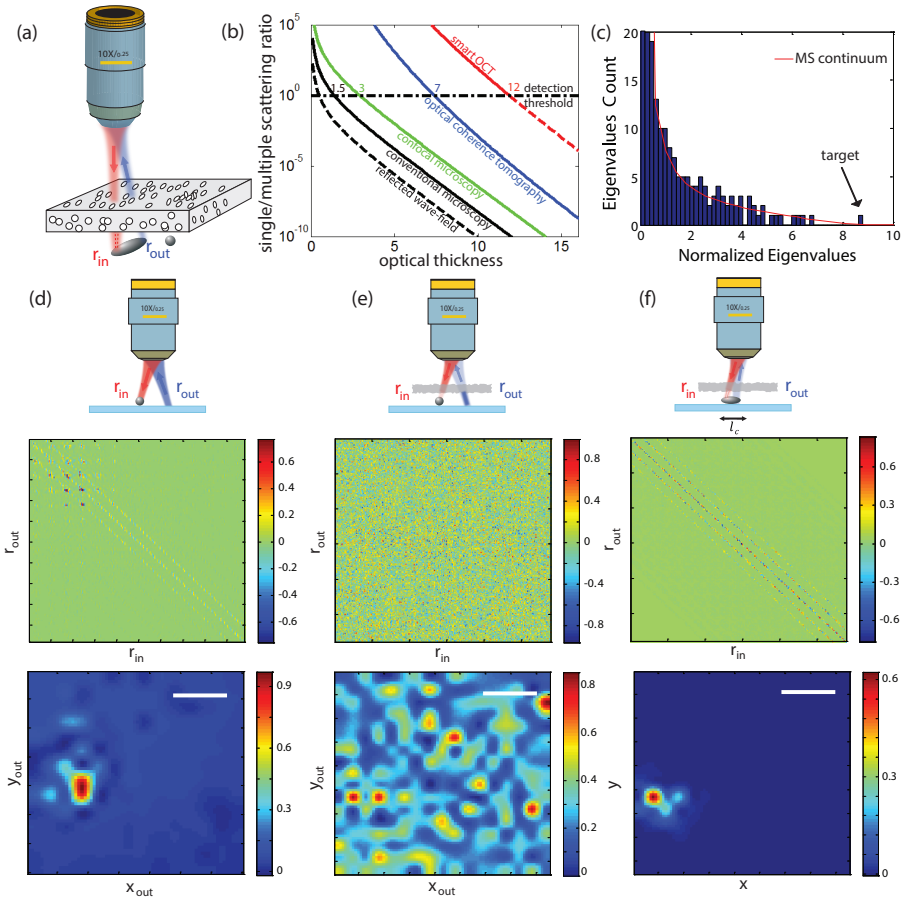

Figure 3.3: Optical target detection in the deep multiple scattering regime. (a) Experimental configuration. (b) Theoretical evolution of the single-to-multiple scattering ratio as a function of the optical thickness L/ℓ_s considering the parameters of the experiment [27]. (c) Eigenvalue histogram of $\mathbf{R_S R_S^\dagger}$ compared to the random matrix prediction (red line): The largest eigenvalue σ_1^2 clearly emerges from the multiple scattering continuum. (d) Reference time-gated reflection matrix $\mathbf{R_0}$ measured for a ZnO bead deposited on a glass slide (top) and corresponding confocal image (bottom). (e) Time-gated reflection matrix $\mathbf{R_{rr}}$ in presence of a strongly scattering layer ($L = 12.25\ \ell_s$) and corresponding confocal image (bottom). (e) Single scattering matrix $\mathbf{R_S}$ deduced from $\mathbf{R}$ with $l_c = 5\ \mu$m [Eq. (3.1)] and smart-OCT image deduced from the first eigenstate of $\mathbf{R_S}$. Scale bar: 10 μm. Figure inspired from [27].

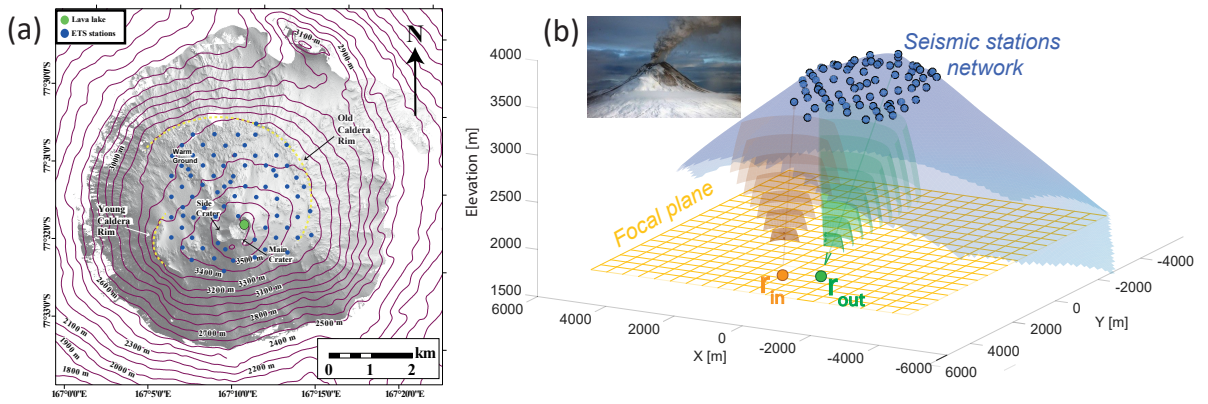

Figure 3.4: (a) Map of the Erebus volcano upper edifice with some principal geographic and geological features and showing the locations of the ETS Erebus stations. (b) Post-processing focusing of the recorded reflection matrix at emission and reception on two points $\mathbf{r_{in}}$ and $\mathbf{r_{out}}$ of the focal plane ($z = ct/2$). The same operation is repeated for any couple of points in the focal plane and yields the focused reflection matrix $\mathbf{R_{rr}}$

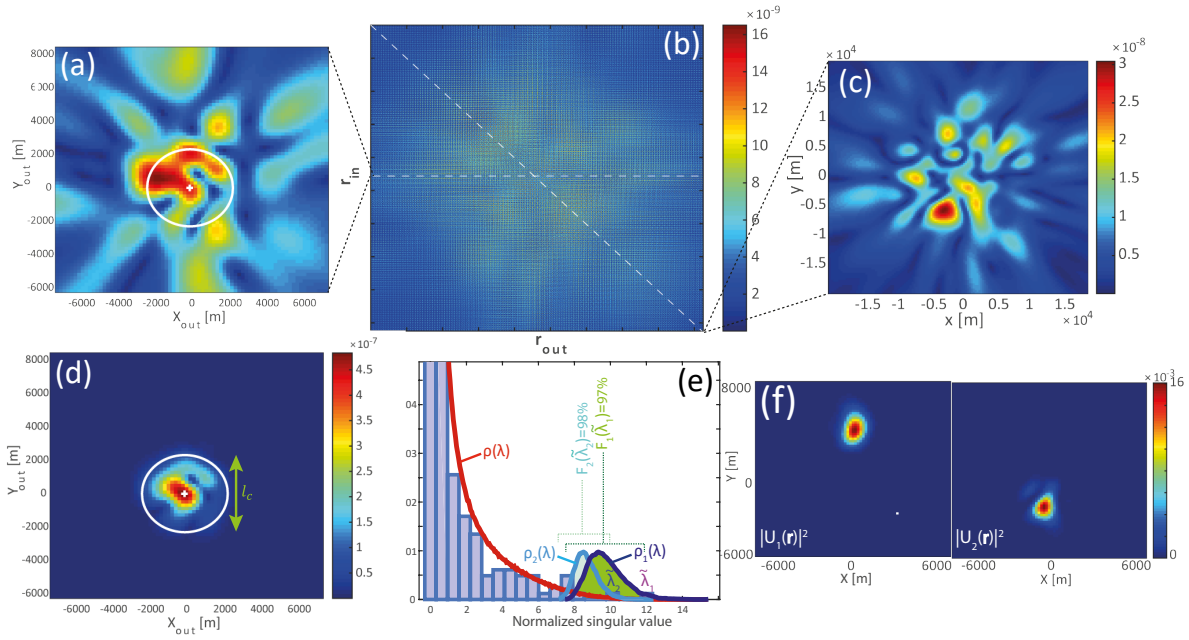

Figure 3.5: Matrix imaging process at time-of-flight $t = 5$ s. (a) Every line or column corresponds to the reflected wave-field for an input or output focusing point, $\mathbf{r_{in}}$ or $\mathbf{r_{out}}$, respectively. (b) The 2D representation of $\mathbf{R_{rr}}$ corresponds to a set of block matrices that represents the reflection matrix between two lines of virtual geophones in the focal plane. (c) The diagonal of $\mathbf{R_{rr}}$ provides the raw confocal image of the volcano at effective depth $z = ct/2$. (d) Adaptive confocal filter [Eq. 3.1] applied to the wave-field displayed in (a). (e) Histogram of the experimental singular values compared with the probability density functions $\rho(\lambda)$ (red line), $\rho_1(\lambda)$ (dark blue line) and $\rho_2(\lambda)$ (light blue line) that would be obtained in a fully developed multiple scattering regime. The integration of $\rho_1(\lambda)$ (green shaded area) and $\rho_2(\lambda)$ (blue shaded area) from 0 to $\tilde{\lambda}_1$ and $\tilde{\lambda}_2$, respectively, yields the likelihood index of the corresponding eigenspaces. (d,e) Images associated with the two first eigenstates of matrix $\mathbf{R}_S$, respectively.

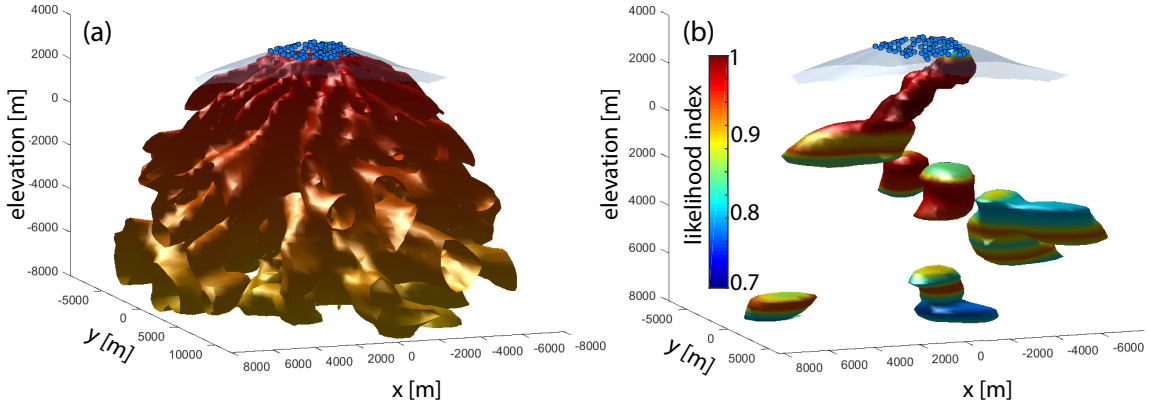

Figure 3.6: Isosurface plots of the three dimensional images of the volcano built from (a) confocal focusing and (b) matrix imaging. For all these isosurface plots, the images are multiplied in depth by a factor z^2 to compensate for the geometrical decrease of singly-scattered body waves. The isosurface is fixed to be 4% of the maximum of each image. The color scale in panel (b) accounts for the likelihood index associated with the singular vector at each depth

2 Matrix beamforming in the multiple scattering regime

This reflection matrix beamforming process is inspired by my collaboration with the group of Stefan Rotter and the scattering invariant operator $\mathbf{T}\mathbf{T}_\mathbf{0}^\dagger$ they developed in transmission to determine the mode that propagate through a complex medium of transmission matrix $\mathbf{T}$ as if they were propagating in free space (modeled by the reference matrix $\mathbf{T}_0$). The implementation of this idea in reflection has been performed by Antton Goicoechea and Arthur Le Ber in the framework of their post-doc and PhD thesis in my team.

The complex spatio-temporal signature of a target is grasped by its reflection matrix $\mathbf{R}_0(\mathbf{r}_0, f)$ recorded for a given position $\mathbf{r}_0$ of the target inside an homogeneous medium. $\mathbf{R}_0(\mathbf{r}_0, f)$ contains the backscattered echoes induced by the target for a given set of illuminations at each frequency f of a given bandwidth Δf. Thanks to projections between the acquisition bases and the focused basis of $\mathbf{R}_0(\mathbf{r}_0, f)$, one can virtually shift the object in the field-of-view and emulate the reflection matrix $\mathbf{R}_0(\mathbf{r}, f)$ that we would measure if it was located at any point $\mathbf{r}$ in the medium. To retrieve now the same object buried inside a heterogeneous medium, one can record its associated reflection matrix $\mathbf{R}(f)$, except that it now contains a detrimental multiple scattering contribution that prevents us from imaging the target via conventional beamforming methods. However, a matrix beamforming process can be built by considering the scalar product between $\mathbf{R}(f)$ and $\mathbf{R}_0(\mathbf{r}, f)$, such that

$$\mathcal{I}(\mathbf{r}) = \int_{\Delta f} df \, \mathrm{Tr}\left\{\mathbf{R}(f)\mathbf{R}_0^\dagger(\mathbf{r}, f)\right\} \tag{3.2}$$

This procedure yields a position likelihood map $\mathcal{I}(\mathbf{r})$ of the object within the medium. By compressing the originally dispersed specific signature of the buried target at a single point, the target signal can be increased up by a gain that scales as the number $M = N_s^2 \times N_t$ of spatio-temporal degrees of freedom exhibited by the reference reflection matrix $\mathbf{R}_0(\mathbf{r}_0, f)$. The number N_s of spatial degrees of freedom scales as the number of resolution cells contained in the target. The number N_t of temporal degrees of freedom scales as the product between the reverberation time of the target and the frequency bandwidth. The more complex the target is, the better the gain in terms of signal-to-multiple scattering ratio will be. This could lead to a retrieval of the object position as if the medium had been made suddenly homogeneous.

The experimental proof-of-concept has been provided by Arthur Le Ber during his PhD thesis in collaboration with Xiaoping Jia and Arnaud Tourin, the experts of acoustic waves in granular media at the Langevin Institute. The experimental set up consists in a 2D matrix probe (32×32 elements; 0.5 mm pitch; 3 MHz; 80% bandwidth) placed in front of a strongly scattering granular suspension, i.e., random packings of 350 μm-diameter glass bead immersed in water [204]. From transmission measurements of the coherent pulse [205] and of the mean intensity [205], we estimate the longitudinal phase velocity $c_\phi \sim 1.8$ mm/μs and the scattering/transport mean free path $\ell_s \sim \ell_t \sim 1.8$ mm. The intruders that we want to image are two 8-mm and 10-mm-diameter steel spheres buried at $z \sim 4\ell_s$ and $5\ell_s$ mm below the medium surface [Fig. 3.7(a)]. These imaging conditions are thus particularly desperate. Fig. 3.7(b) shows the confocal image of the whole medium. The presence of two targets is not revealed because

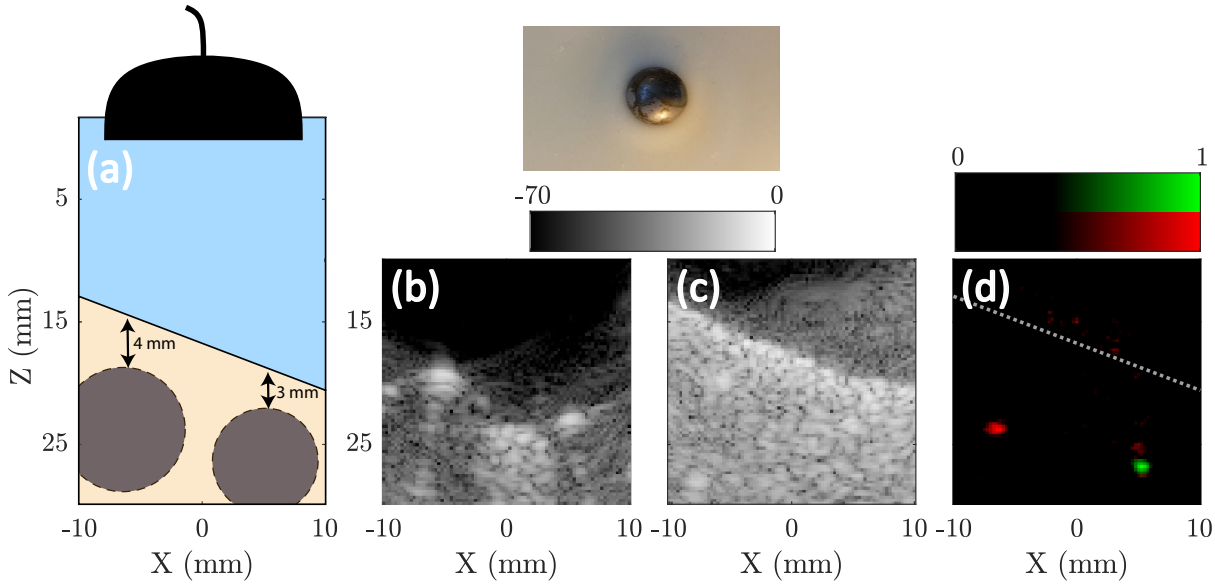

Figure 3.7: Matrix imaging of sinking steel spheres in strongly scattering granular media. (a) Experimental set up. (b,c) Ultrasound image of the two spheres in absence and presence of the granular medium, respectively. (d) Position likelihood map for each intruder by means of matrix beamforming. Green and red channels respectively correspond to the 8-mm and 10-mm diameter steel spheres. Figure courtesy of Arthur Le Ber.

of a largely predominant multiple scattering background. On the contrary, matrix beamforming enables to build a likelihood map for each target position [Fig. 3.7(c)] and their exact positions are unambiguously retrieved.

The complex spatio-temporal signature of the beads accounts for this spectacular result and is highlighted in Fig. 3.8 for the 8-mm steel sphere in water. Its confocal signal exhibits a long reverberation time [Fig. 3.8(c)] due to Mie (bulk) [Fig. 3.8(d)] and Rayleigh (surface) wave resonances [Fig. 3.8(f)] [206, 207]. The reflection matrix also displays a complex spatial signature [208, 209] highlighted by a strong off-diagonal energy of $\mathbf{R}_0$ in the focused basis [Fig. 3.8(e)]. The extended size of the targets ($N_s \sim 12-20$) in hand with their long temporal tail ($N_t \sim 32$) give rise to a high number of spatio-temporal degrees of freedom ($M \sim 380-640$) that allows us compensate for the drastic decrease of singly-scattered waves in the granular medium by a factor ($\exp(F/\ell_s) \sim 50-150$).

This proof-of-concept experiment is spectacular and opens great perspectives for imaging in wave physics. Indeed it can be applied to any field for which multi-element technology is available (bio-medical imaging, non-destructive testing, seismology, sonars etc.). Compared to an iterative time reversal process, a prior information on the target is required but it makes the best to exploit all the spatio-temporal degrees of freedom provided by the target. Note that this matrix beamforming process is closely related to the method proposed by Ammari *et al.* [210–212] that was dedicated to target detection using a dictionary of precomputed reflection matrices. One limit of the current approach is that we only exploit singly-scattered waves to detect the target. To go beyond and harness the scattering events induced by the surrounding medium, a combination of the matrix beamforming process along with the distortion matrix

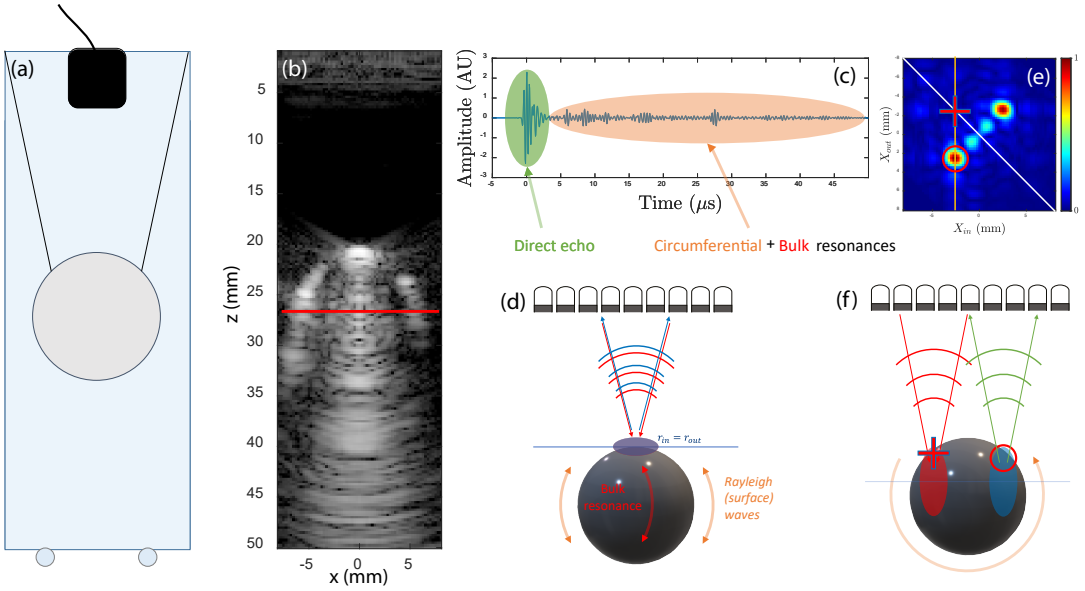

Figure 3.8: Spatio-temporal degrees of freedom exhibited by the reference matrix $\mathbf{R}_0$ of the steel sphere ($\phi = 8$ mm). (a) Experimental set up used for the recording of the reference reflection matrix. (b) Cross-sectional view of the ultrasound image. (c) Time-dependence of the confocal signal at the cap of the sphere. (d) Bulk and surface wave resonances accounting for the long signal tail in (b) and (c). (e) Focused $\mathbf{R}_0$-matrix at depth $z = 27$ mm of the ultrasound image (red line) in (b). (f) Surface waves accounting for the off-diagonal echoes in panel (e). Figure courtesy of Arthur Le Ber.

approach can be rewarding. The target can indeed be used as a guide star in the MI process. In the next section, we describe a first step towards this ambitious goal by investigating the time-dependence of $\mathbf{D}-$matrix, in contrast with the first Chapter in which the $\mathbf{D}-$matrix was considered at the single ballistic time.

3 Towards a compensation of multiple scattering paths

3.1 Iterative time reversal of the distortion matrix

The time-dependence of the $\mathbf{D}$-matrix is currently investigated by Elsa Giraudat. Here, I present some preliminary results we obtained in ultrasound imaging that will allow us to draw perspectives for my research project in the next few years.

The experimental set up is described in Fig. 3.9(a). The sample under study is a tissue-mimicking phantom ($c_0 = 1542$ m.s^{-1}). It is composed of a random distribution of unresolved scatterers, which generate an ultrasonic speckle characteristic of human tissue (gray background in Fig. Fig. 3.9(a)). The phantom also contains eight sub-wavelength nylon monofilaments placed perpendicularly to the probe (white point-like targets). The bright circular targets located at depth z=50 mm on the image (Fig. 3.9(b)) is a section of a hyperechoic cylinders composed of a higher density of unresolved scatterers. A 15-mm-thick layer of plexiglass ($c_0 = 1542$ m.s^{-1}) is placed on top of the phantom and is responsible for both the strong aberrations and multiple

reflections displayed by the ultrasound image [Fig. 3.9(b)].

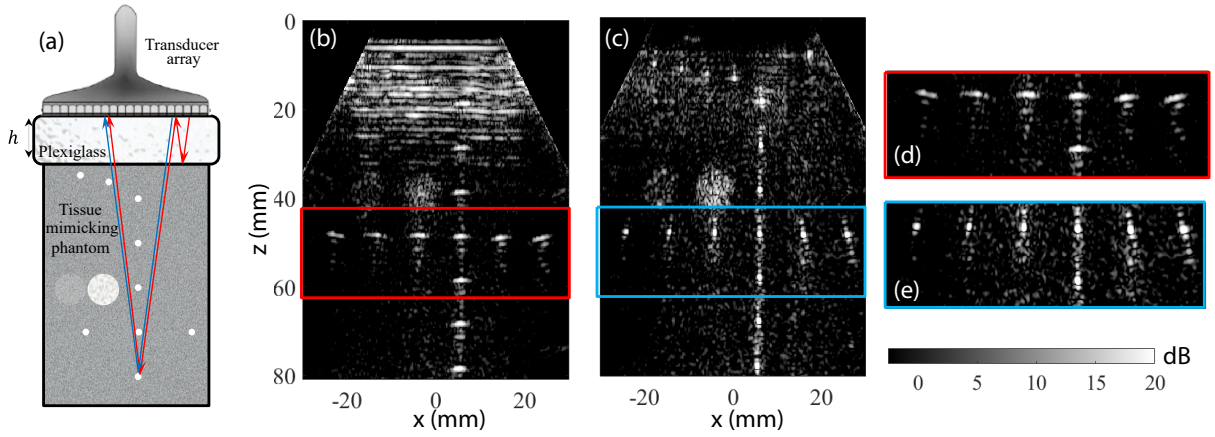

Figure 3.9: Time of the **D**-matrix for compensation of multiple reflections in ultrasound imaging. (a) Experimental configuration. (b,c) Ultrasound image before and after compensation of multiple reflections. (d,e) Zooms on the initial and corrected UMI images displayed in (b,c), respectively. Figure courtesy of Elsa Giraudat.

To compensate for the multiple reverberations induced the plexiglas layer, the $\mathbf{D}-$matrix is considered in a speckle area (white rectangle in Fig. 3.9(a) and investigated in the time domain. The spatio-temporal focusing law required to compensate for aberrations and multiple reverberations is determined by a virtual iterative phase reversal process applied to the $\mathbf{D}-$matrix sketched in Fig. 3.10. This procedure sketched in Fig. 3.9 is the matrix equivalent of the delay-and-sum method proposed by Montaldo *et al.* [113] to compensate for aberrations in ultrasound speckle noise and that we here exploit to compensate for multiple reverberations. The result is displayed in Fig. 3.9(c). The matrix image shows a clear improvement compared to its standard counterpart with the revelation of bright scatterers at shallow depth ($z < 25$ mm) that were originally completely hidden by the multiple reverberations in the plexiglas layer. At larger depths, the contrast of the hyperechoic structures is drastically enhanced. The image resolution highlighted by the apparent size of each point-like target is restored as if the plexiglass layer had been removed.

The spurious echoes observed behind each point-like target in Fig. 3.9(b) are also partially eliminated by the extracted spatio-temporal focusing laws. The residual secondary lobes are inherent to the time reversal process which can be seen as a matched filter. Let $H(\mathbf{r},\mathbf{r}_{\text{in}},t)$ be the focused wave-field at point $\mathbf{r}$ when trying to focus at point $\mathbf{r}_{\text{in}}$ [Fig. 3.10(a)]. The time reversed wave at the focal point can be expressed as the auto-correlation of the initial transmitted wave-field: $[H \overset{r}{\circledast}\overset{t}{\circledast} H](\mathbf{r},\mathbf{r}_{\text{in}},t)$ [Fig. 3.10(e)]. If the transmitted wave-field $H(\mathbf{r},\mathbf{r}_{\text{in}},t)$ is a random speckle wave-field (as it would be in a multiple scattering regime), the focused wave shows a central peak only limited by the bandwidth of our initial measurement. If $H(\mathbf{r},\mathbf{r}_{\text{in}},t)$ exhibits deterministic arrivals [see Fig. 3.10(a)], the time-reversed pulse shows strong secondary lobes [see Fig. 3.10(e)]. In that case, an inverse filter process should thus be considered to eliminate those secondary lobes. This will be the next step for the removal of reverberations but some questions naturally arise about the ability of the **D**-matrix approach for the compensation of

multiple scattering paths.

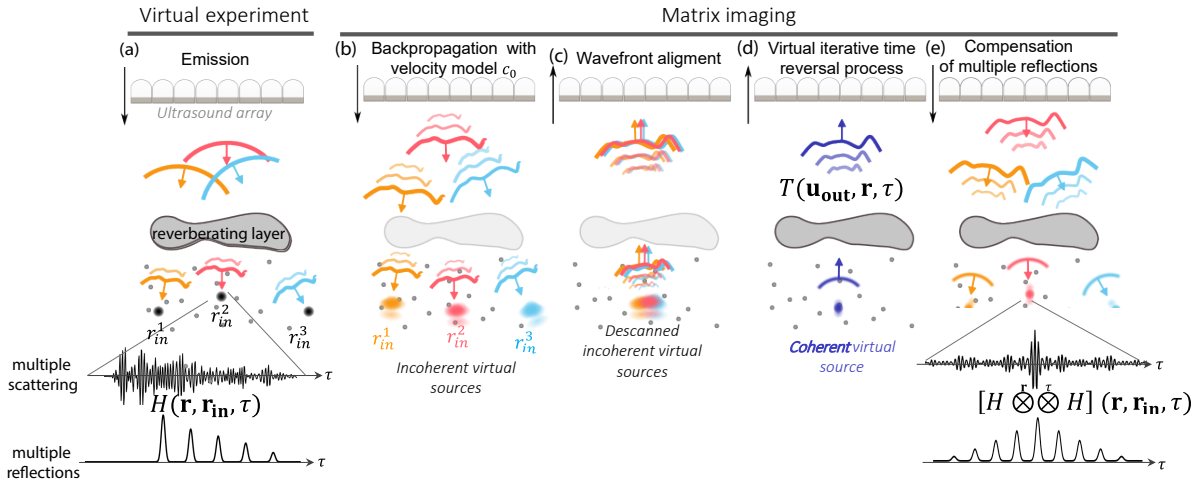

Figure 3.10: Sketch of the iterative phase reversal process applied to a time-dependent **D**-matrix through a reverberating layer. (a,b) Virtual experiment that would consist in focusing waves at specific locations $\mathbf{r}_{\text{in}}$ and recording the time-dependent multiply scattered wave-field $H(\mathbf{r}, \mathbf{r}_{\text{in}}, t)$ inside the medium. (b) The focused **R**-matrix consists in backpropagating the recorded reflection matrix considering the available wave velocity model. (c) The **D**-matrix consists in realiging the reflected wave-fronts, thereby virtually shifting each input focusing beam at the same location. (d) Iterative time reversal applied to **D** synthesizes a coherent virtual source and yields the time-dependent **T**-matrix between points **r** in the medium and transducers $\mathbf{u}_{\text{out}}$. (e) The time-reversed wave-field is then equal to the spatio-temporal cross-correlation of the initial transmitted wave-field in (a). Figure courtesy of Elsa Giraudat.

In the experiment described in Fig. 3.9, the plexiglass layer exhibits a lateral invariance such that the whole phantom belongs to the same isoplanatic patch. This enabled us to consider the $\mathbf{D}-$matrix over a sufficiently large number N_{in} of input focusing points such that we can converge towards a satisfying spatio-temporal focusing law. The condition for this convergence is that N_{in} is one order of magnitude larger than the number M of independent spatio-temporal coherence grains exhibited by the broadband aberration transmittance. In other words, the more complex the aberration is ($M >> 1$), the larger the isoplanatic patch should be ($N_{\text{in}} >> M$). This is a fundamental issue for deep imaging since the size of isoplanatic patches drastically decreases with depth [97] while the spatio-temporal focusing laws to retrieve become more and more complex because of multiple scattering. In the next section, we establish established a roadmap for the next years to circumvent that fundamental problem.

3.2 Perspectives

As seen above, one will have to play with both spatial and temporal degrees of freedom in order to harness multiply-scattered waves. The measurement of a broadband **D**-matrix and a spatio-frequency analysis of its correlations should be coupled to learning based methods in order to retrieve a time-dependent **T**-matrix that will allow using the medium heterogeneities as a scattering lens and extend the penetration depth of MI beyond the transport mean free

path ℓ_t [see Fig. 2.23(g)]. Such an approach can also be rewarding in terms of resolution since scattering can increase the effective numerical aperture of the imaging system and lead to super-resolution [38]. In the next few years, I plan to work on the incorporation of these learning based methods in the general framework of MI in collaboration with Sébastien Popoff [213] and Victor Barolle, two experts of optimization, inversion and learning approaches at the Langevin Institute.

The training of numerical models designed to incorporate physical insights has already shown promising results, e.g by demonstrating the compensation of aberration in optical measurements [14] or predicting the transmission properties of thin diffusers [214]. Exploiting those insights has two interesting consequences: (i) by drastically restricting the space of solutions, it limits overfitting and reduces the amount of information required for the training process; (ii) accessing the model parameters after training could allow predicting various properties of the physical system.

Finding a way to efficiently combine physical insights and learning approaches may be the key to retrieve transmission information from the **R**-matrix in multiple scattering media. Using deep learning frameworks one can create physics inspired models for light propagation inside inhomogeneous media. The propagation equation, its invariants and/or its statistical properties can be incorporated into numerical models. For instance, for biological tissues in optics, where the scattering is anisotropic, light propagation is well modeled by a series of diffraction events by thin diffusers with free space propagation in between [215]. One could then envision models that mimic these effects using layers with trainable parameters. Once trained on a measured **D**-matrix, it can be used to predict the associated **T**-matrix.

Besides the specific case of biological media in optics, a layered approach is also particularly appropriate to develop an iterative reconstruction of the medium properties. Our strategy will be actually the following. Use the properties extracted at shallow layers to improve the propagation model at deeper layers. Preliminary ultrasound experiments in granular media have shown the merit of this strategy. In that perspective, the wave velocity tomography that we are currently developing in the framework of MI is crucial [31]. A precise knowledge of the wave velocity distribution at shallow layers favors the range of the memory effect at deeper layers and our ability to retrieve a precise estimation of the **T**-matrix beyond the transport mean free path.

Besides the precise estimation of the forward scattering component of the **T**-matrix, its Born development will be required to cope with the multiple scattering regime. To that aim, the idea is to decompose the **R**-matrix into its higher scattering orders, as we recently did in a weaker scattering regime [50]. Again, inversion algorithms and/or learning based methods will be relevant tools to unscramble the different scattering orders of the **T**-matrix from the Born series of the **R**-matrix.

The mapping of the wave velocity and scattering parameters is thus particularly important to build an accurate estimator of the $\mathbf{T}-$matrix inside the medium. Those quantities are also quantitative markers for biomedical diagnosis and also important monitoring parameters of tectonic motion and volcanic eruption in geophysics. In the next Chapter, we show how the information contained in the refection matrix can lead to a tomography of these parameters, thereby going beyond a simple image of the medium reflectivity.

CHAPTER 4

Quantitative Matrix Imaging

Publications

- A. Badon, D. Li, G. Lerosey, A. C. Boccara, M. Fink, and A. Aubry, *Spatio-Temporal Imaging of Light Transport in Highly Scattering Media under White Light Illumination*, Optica **3**, 1160-1166 (2016)
- W. Lambert, L. A. Cobus, M. Couade, M. Fink, and A. Aubry, *Reflection Matrix Approach for Quantitative Imaging of Scattering Media*, Phys. Rev. X **10**, 021048 (2020)
- W. Lambert, F.Bureau, T. Frappart, and A. Aubry, *Method and system for ultrasonic characterization of a medium*, US Patent n° US20220082527 (2022)
- L. A. Cobus, G. Maret, and A. Aubry, *Crossover from renormalized to conventional diffusion near the 3D Anderson localization transition for light*, Phys. Rev. B **106**, 014208 (2022)
- C. Brütt, A. Aubry, B. Gérardin, A. Derode, and C. Prada, *Weight of single and recurrent scattering in the reflection matrix of complex media*, Phys. Rev. E **106**, 025001 (2022)

The idea of this Chapter is to exploit effects which are detrimental to reflectivity imaging (such as distortion and scattering) to create different imaging modalities. In the ballistic regime (where single scattering dominates), the refractive index can be estimated by analyzing the distortion undergone by the wave as it passes through the medium. This is the principle of quantitative phase imaging [216] in optics and computed tomography [217] in ultrasound imaging. Most such approaches, however, require a transmission configuration, which is not practical for thick scattering media, and which is impossible for most *in-vivo* or *in-situ* applications in which only one side of the medium is accessible. In reflection, recent works in ultrasound imaging have leveraged the relationship between the speed of sound c and wavefront distortion to measure c [117, 218, 219]. Based on a study of the spatial or temporal coherence between emitted and detected signals at a transducer array, such approaches are promising for mapping the wave velocity $c(\mathbf{r})$ when single scattering dominates. In the multiple scattering regime, optical diffuse tomography [152] is a well-established technique to reconstruct the spatial distribution of transport parameters at each point of a volume from intensity measurements at the surface. Unfortunately, this inverse problem is intrinsically nonlinear with respect to the optical properties of the medium. This method is thus computationally intensive and limited in terms of spatial resolution [220–222] since the latter one scales with the imaging depth.

In this Chapter, we show how the reflection matrix approach can be a powerful tool to map physical parameters such as the wave velocity or transport parameters such as the scattering and transport mean free paths, or the diffusion coefficient. Not only are these parameters quantitative markers for biomedical diagnosis in ultrasound imaging [107, 223–227] and optical microscopy [152], but they are also important observables for non-destructive evaluation [228–230] and geophysics [198, 231, 232]. During the PhD thesis of William Lambert, we showed how the focusing factor introduced in Chapter 2 could be used to retrieve the depth evolution of the wave velocity in multi-layered media [31]. A map of a multiple scattering rate can also superimposed to the ultrasound image [31, 32]. Such a map can be an important observable for clinicians since it can be used as a reliability index of the image. Nevertheless, this quantity cannot be directly related to the local scattering parameters of tissues since multiply-scattered echoes arrive after the ballistic time. Our objective here is to exploit the multiple scattering contribution for mapping transport parameters. These physical quantities are actually directly related to the micro-architecture of tissues [233] and can provide novel bio-markers for ultrasound diagnosis [234, 235].

To provide a quantitative mapping of the wave velocity and transport parameters, we here extend the study of the focused reflection matrix beyond the ballistic time and show how its time evolution can provide a self-portrait of the wave inside the scattering medium [236, 237]. In the single scattering regime, such a propagation movie is exploited to map the local wave velocity throughout the field-of-view. The experimental proof-of-concept is provided by means of an *in-vivo* ultrasound experiment performed on the liver of a difficult-to-image patient. In the multiple scattering regime, the temporal growth of the diffusive halo can be retrieved at the surface of the scattering sample [30, 234]. A proof-of-concept is provided for optical microscopy and relies on the passive measurement of the reflection matrix by low-coherence interferometry [40, 173].

It shows our ability to map the transverse evolution of the diffusion coefficient with a spatial resolution not given by the thickness of the sample, as it would be in transmission, but of the order of the transport mean-free path ℓ_t. At the end of the Chapter, we discuss about the future of quantitative MI by mentioning, in particular, the other physical parameters we can map with the reflection matrix and discuss its extension to 3D imaging in different fields of wave physics.

1 Self-portrait of the wave by itself

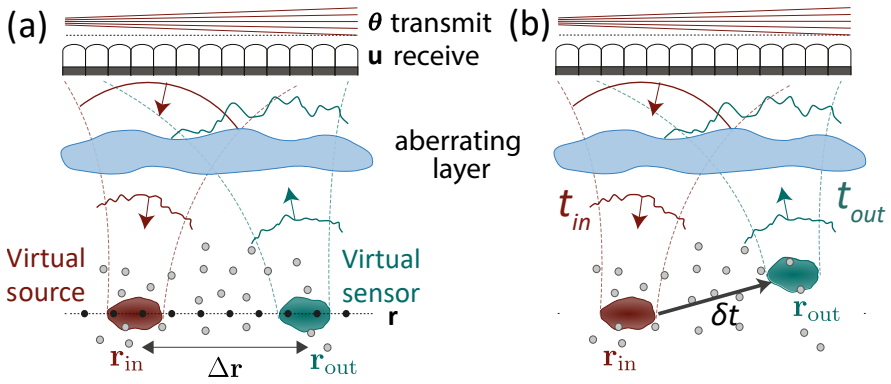

Figure 4.1: Time-dependence of the focused reflection matrix. (a) While the focused reflection matrix $\mathbf{R_{rr}}$ was originally considered in Chapter 2 at the single ballistic time ($\tau = 0$) and for virtual source/receiver located at the same depth ($z_{\text{in}} = z_{\text{out}}$), (b) its temporal response is now investigated between input and output focusing points at any depth. Figure courtesy of William Lambert.

While, in Chapter 2, focusing parameters and single/multiple scattering rates have been extracted from the focused reflection matrix considered at the single ballistic time, we here show how to exploit its time-dependence to map the wave velocity [236]. $\mathbf{R_{rr}}(\delta t)$ can be thought of as a matrix of impulse responses between virtual transducers located inside the medium [see Fig. 4.1]. In this time-dependent frame studied by William Lambert during his PhD thesis, each virtual source is associated with a focused incident wave while each virtual sensor enables to probe the propagation of this wave through the medium in the time domain.

Figure 4.2(b)-(f) shows the snapshots of a wave-field focused at a given point $\mathbf{r}_{\text{in}}$ and probed by virtual sensors at $\mathbf{r}_{\text{out}}$ in a tissue-mimicking phantom. The ballistic component of the wave-field can be detected [surrounded by a white dashed circle in Fig. 4.2(b)-(f)]. However, it is modulated by the random reflectivity of the medium. Moreover, the focused reflected wave-field also shows a random speckle background due to scattering events taking place outside the input focal spot. To circumvent these two detrimental effects and isolate the ballistic component, one can exploit the local isoplanicity of the wave-field. The coherent component of the wave-field can be extracted from a cross-correlation between the propagation movies obtained for input focal spots contained in the same isoplanatic patch. Mathematically, this can be done by means of a SVD of the de-scanned focused reflection matrix $\mathbf{R}_{\Delta\mathbf{r},\mathbf{r}}(t) = [R(\{\Delta\mathbf{r}_{\text{out}}, t\}, \mathbf{r}_{\text{in}})]$, with $\Delta\mathbf{r}_{\text{out}} = \mathbf{r}_{\text{out}} - \mathbf{r}_{\text{in}}$ the relative position between output and input focusing points. This operation

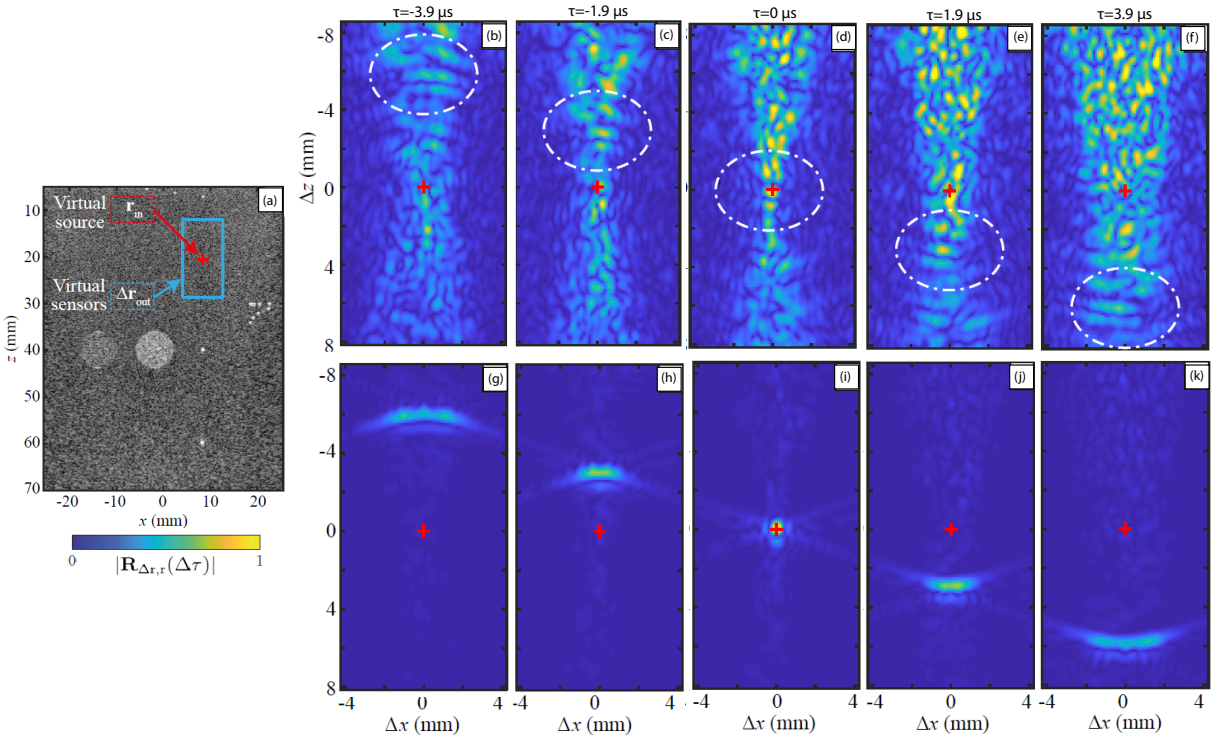

Figure 4.2: Propagation movie of a wave-field focused at a given point $\mathbf{r}_{\text{in}}$ in a tissue mimicking phantom. (a) Ultrasound image of the probed medium. (b)-(f) Snapshots of the movie at different lapse time τ for a virtual source whose position $\mathbf{r}_{\text{in}}$ is indicated by a red cross in (a). The wave-field is shown in a descanned basis ($\boldsymbol{\Delta r} = \mathbf{r}_{\text{out}} - \mathbf{r}_{\text{in}}$). (g)-(h) Shapshots of the first eigenvector $\mathbf{U}_1$ of $\mathbf{R}_{\boldsymbol{\Delta r},\mathbf{r}}(t)$ considered over a set of input focusing points contained in the blue rectangle in (a). Figure courtesy of William Lambert.

amounts to average the focused wave-field over multiple realizations of disorder and synthesize coherent virtual sources and detectors that allow to map the time propagation of the coherent wave inside the medium. The first eigenstate $\mathbf{U}_1 = [U_1(\boldsymbol{\Delta r}, t)]$ is displayed in Figs. 4.2(g)-(k). It highlights the spatio-temporal focusing of the ballistic wave inside the medium. A self-portrait of the ultrasonic compressional wave is thereby obtained using the scatterers as local microphones inside the medium.

2 Mapping the wave velocity

By analogy with the shear wave propagation films in tissues [238] that can provide an image of the shear modulus [239], a map of the speed-of-sound can be extracted from compressional wave movies. In Figs. 4.2(g)-(k), the coherent wave focuses at $\boldsymbol{\Delta r} = \mathbf{0}$ (red cross) at the expected ballistic time ($\tau = 0$) because the wave velocity model matches with its actual distribution. Interestingly, this is no longer true when the wave velocity model c_0 goes away from the true speed-of-sound c_t [Figs. 4.3]. For $c_0 < c_t$, the coherent wave is delayed and the focus takes place beyond the targeted focusing point [Figs. 4.3(b)-(c)]. For $c_0 > c_t$, the focusing time and depth are, on the contrary, smaller than expected [Figs. 4.3(d)-(e)]. By finely tuning the wave

velocity model, one can shift the position of the focal spot at the origin and retrieve the true wave velocity.

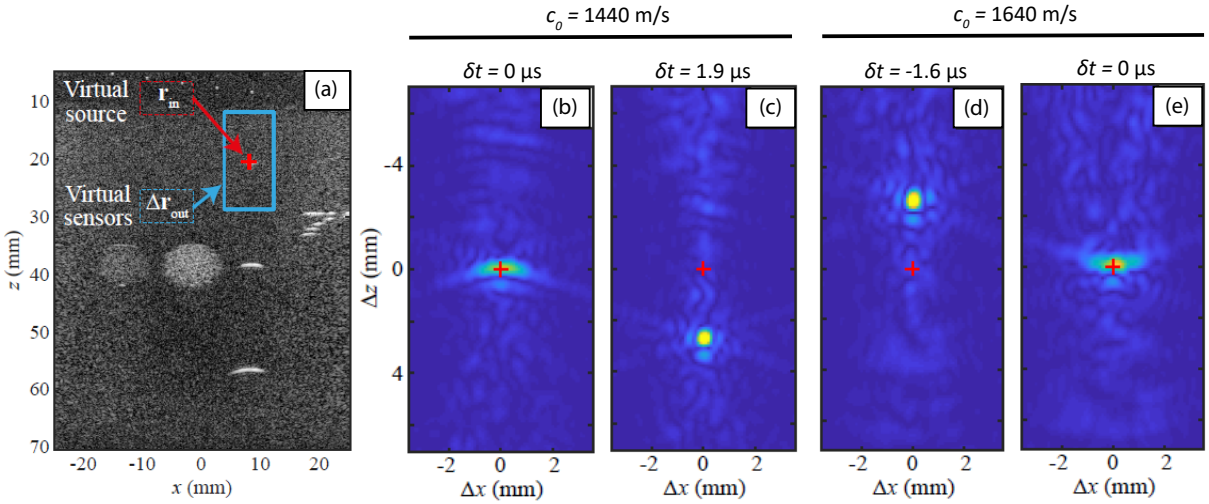

Figure 4.3: Extracting the medium speed-of-sound from the self-portrait of the focused wavefield. (a) Ultrasound image of the probed medium built using a wrong speed-of-sound model ($c_0 = 1440$ m/s). (b)-(c) Snapshots of the propagation movie for $c_0 = 1440$ m/s. (d)-(e) Shapshots of the first eigenvector $\mathbf{U}_1$ of $\mathbf{R}_{\Delta\mathbf{r},\mathbf{r}}(t)$ considered over a set of input focusing points contained in the blue rectangle in (a)Snapshots of the propagation movie for $c_0 = 1440$ m/s. Figure courtesy of William Lambert.

This striking property can be leveraged for mapping the speed-of-sound of heterogeneous media. An experimental proof-of-concept has been provided by Flavien Bureau during his PhD thesis. The medium under study is the liver of a difficult-to-image patient. A quantitative measurement of the speed-of-sound in liver is particularly important for the early detection of liver disease, such as hepatic steatosis [218]. This disease consists in an accumulation of fat droplets that results in a low speed-of-sound ($c \sim 1480$ m.s^{-1}) compared to its usual value in liver ($c \sim 1600$ m.s^{-1}). The effectiveness of ultrasound for diagnosing hepatic steatosis is reduced in obese patients [240]. Indeed, because the ultrasonic waves must travel through successive layers of skin, fat, and muscle tissue before reaching the liver, both the incident and reflected wave-fronts undergo strong aberrations [108, 241] and multiple scattering (clutter noise) [242]. The estimation of the speed-of-sound in liver is thus particularly difficult for such patients.

Figure 4.4 shows the result of the time-dependent MI process in liver. The acquisition was performed using a curve probe (XC6-1, Supersonic Imagine) with a sequence of 41 curved incident waves on the liver of a difficult-to-image patient. Figure 4.4(a) displays the conventional image that suffers from a lack of contrast and resolution due to important variations of speed-of-sound between the fat layer, muscle fibers and liver. Figure 4.4(b) displays the speed-of-sound integrated between the probe and each pixel using the process described above:

$$\bar{c}(x,\bar{z}(x)) = \frac{1}{\bar{z}(x)} \int_0^{\bar{z}(x)} \frac{dz}{c(x,z)} \tag{4.1}$$

with $\bar{z}(x) = \bar{c}(x,z)t/2$ and t the echo time associated with each pixel of the ultrasound image. To retrieve a map of the local speed-of-sound $c(\mathbf{r})$ from the integrated wave velocity, one has to inverse the previous equation (Eq. 4.1) that links both quantities. Using the tomographic sound speed reconstruction developed by Ali *et al.* [243], a local speed-of-sound distribution can be retrieved [Fig. 4.4(c)]. It highlights the different layers (fat and muscle fibers) that the ultrasonic wave has to go through before reaching the liver. A particularly weak speed-of-sound is estimated in the liver, which could be a manifestation of hepatic steatosis.

Based on this speed-of-sound distribution, a novel ultrasound image can be built by re-assigning to each pixel of the image its true depth [Fig. 4.4(e)]. The obtained image shows a much better contrast and resolution, thus enhancing structures such as muscle fibers and vessels inside the liver [Fig. 4.4(f)]. Compared with the initial ultrasound image [Fig. 4.4(d)] whose axial dimension is dictated by the echoes' time-of-flight, each pixel in the matrix image is shifted to its real position in depth, thereby giving access to absolute distances. This feature can be a major breakthrough in ultrasound imaging since a lot of diagnoses rely on distance measurements [244] as, for instance, in obstetrics to monitor fetal growth or detect chromosomal abnormality [245, 246]. This experimental proof-of-concept highlights the potential of MI for a quantitative characterization of tissues via a local mapping of the speed-of-sound.

Of course, further efforts are needed to fully validate the method, compare it with existing approaches [219, 243] and explore its limits. In particular, the reconstruction of the local sound speed could be improved by including it in the forward propagation model [243] and iterating the whole process. Beyond ultrasound imaging, an optical tomography of the refractive index in thick scattering media could be a paradigm shift with respect to quantitative phase imaging that generally only applies to thin layers of tissues. In seismic imaging, a 3D tomography of the bulk wave velocity could be also a relevant observable to improve the image of the subsoil reflectivity in complex areas and probe locally the mechanical properties of the underground [151].

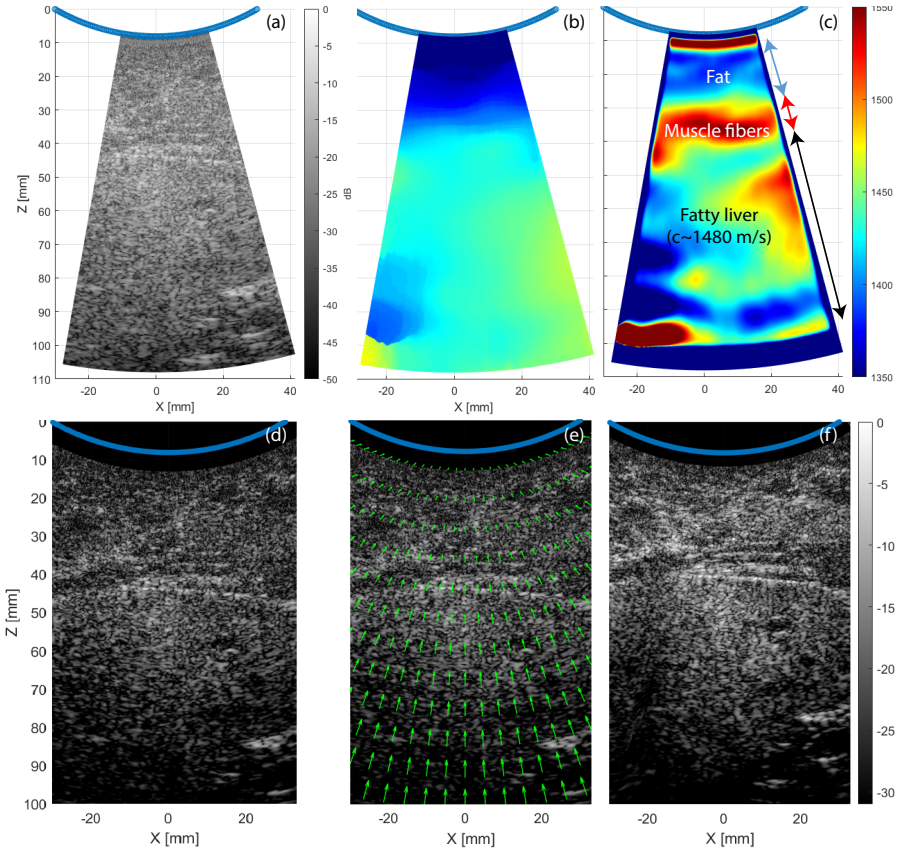

Figure 4.4: Mapping the local speed-of-sound in liver. (a) Initial ultrasound image of a difficult-to-image patient liver. (b) Map of the integrated speed-of-sound $\bar{c}(\mathbf{r})$ extracted from propagation movies of focused wave-fields. (c) Map of the local speed-of-sound $\bar{c}(\mathbf{r})$ retrieved from inversion of Eq. 4.1. (d) Same image as in (a) but with a different field-of-view. (e) Displacement field that shall be applied to each pixel to reposition them at their true depth. (f) Final ultrasound image. Figure courtesy of Flavien Bureau.

3 Measurement of transport parameters in a weakly scattering regime

Apart from the wave velocity, the single scattering contribution can also be leveraged to measure the attenuation coefficient in tissues. For instance, knowing that fat affects ultrasound propagation, this parameter has been used to detect and quantify steatosis in ultrasound imaging. This parameter can be extracted from a time-frequency analysis of the ultrasound image. Different methods have been developed to discriminate the intrinsic attenuation of the medium from diffraction effects and reflectivity fluctuations of the medium [247, 248]. The measured attenuation parameter is however affected by both scattering and absorption losses. The attenuation parameter is actually the inverse of the extinction length ℓ_{ext} that depends on both the absorption length ℓ_a and the scattering mean free path ℓ_s, such that:

$$\ell_{\text{ext}}^{-1} = \ell_a^{-1} + \ell_s^{-1}. \tag{4.2}$$

In the single scattering regime, a discrimination between absorption and scattering losses is thus illusory.

However, as demonstrated in Chapter 2, multiple scattering is actually far from being negligible in ultrasound imaging of soft tissues. Studying it may bring additional information about the scattering structure. In particular, the separation of single and multiple scattering components may allow us to discriminate between absorption and scattering losses. To extract the multiple scattering component, the reflection matrix formalism is particularly fruitful. Originally, single and multiple scattering were shown to exhibit different correlation properties in the far-field reflection matrix measured on a random medium [18, 24] [see Fig. 3.1]. Building on this difference, an algorithm was proposed to separate the single and multiple-scattering contributions in the reflection matrices. Estimators of the multiple and single scattering rates were built by Aubry and Derode [102] and Baelde *et al.* [249]. A temporal fit of both components with radiative transfer theory enabled an independent estimation of ℓ_a and ℓ_s in a weakly scattering medium [102] but this measurement was not local.

More recently, several studies built local estimators of the single/multiple scattering ratios from the focused reflection matrix [31, 50, 250]. Nevertheless, these estimators are biased by recurrent scattering paths whose first and last scattering events take place in the same resolution cell [see Fig. 5.3(a)] [50]. Hence, single scattering estimators $\hat{\alpha}_S$ should rather be termed confocal scattering ratios. Interestingly, in collaboration with Cécile Brütt, Claire Prada, Arnaud Derode and Benoît Gérardin [50], we recently showed by means of numerical simulations that the depth evolution of $\hat{\alpha}_S$ scales as the inverse of the scattering mean free path ℓ_s. Hence, this parameter could be used as a local probe for ℓ_s in a reflection geometry and independently from absorption losses. However, this numerical observation remains to be demonstrated analytically and investigated in the case of scattering media statistically heterogeneous in terms of disorder. An ambitious aim will be to provide a map of transport parameters for a quantitative and local characterization of the medium.

4 Mapping transport parameters in the diffusive regime

In that respect, a first step has been achieved during the PhD thesis of Amaury Badon in the context of optical microscopy [40]. Based on low-coherence interferometry, a Michelson interferometer has been used to compute the focused reflection matrix at the surface of a strongly scattering sample [Fig. 4.5(a)] [173]. This sample is here a heterogeneously disordered layer of ZnO nanoparticles. Variations in the concentration of scatterers are visible at a scale smaller than 100 μm in the microscopic image [see Fig.4.6(a)].

In the diffusive regime, the focused $\mathbf{R}$-matrix recorded at the sample surface provides a unique signature of the complicated trajectories experienced by light in the medium. Here, we exploit it to investigate the mean intensity,

$$P(\Delta r, t) \equiv \langle |R(\mathbf{r}_{\text{out}}, \mathbf{r}_{\text{in}}, t)|^2 \rangle_{\{(\mathbf{r}_{\text{in}}, \mathbf{r}_{\text{out}}) | \| \mathbf{r}_{\text{out}} - \mathbf{r}_{\text{in}} \| = \Delta r\}}, \tag{4.3}$$

as a function of time-of-flight t and distance Δr between $\mathbf{r}_{\text{out}}$ and $\mathbf{r}_{\text{in}}$.

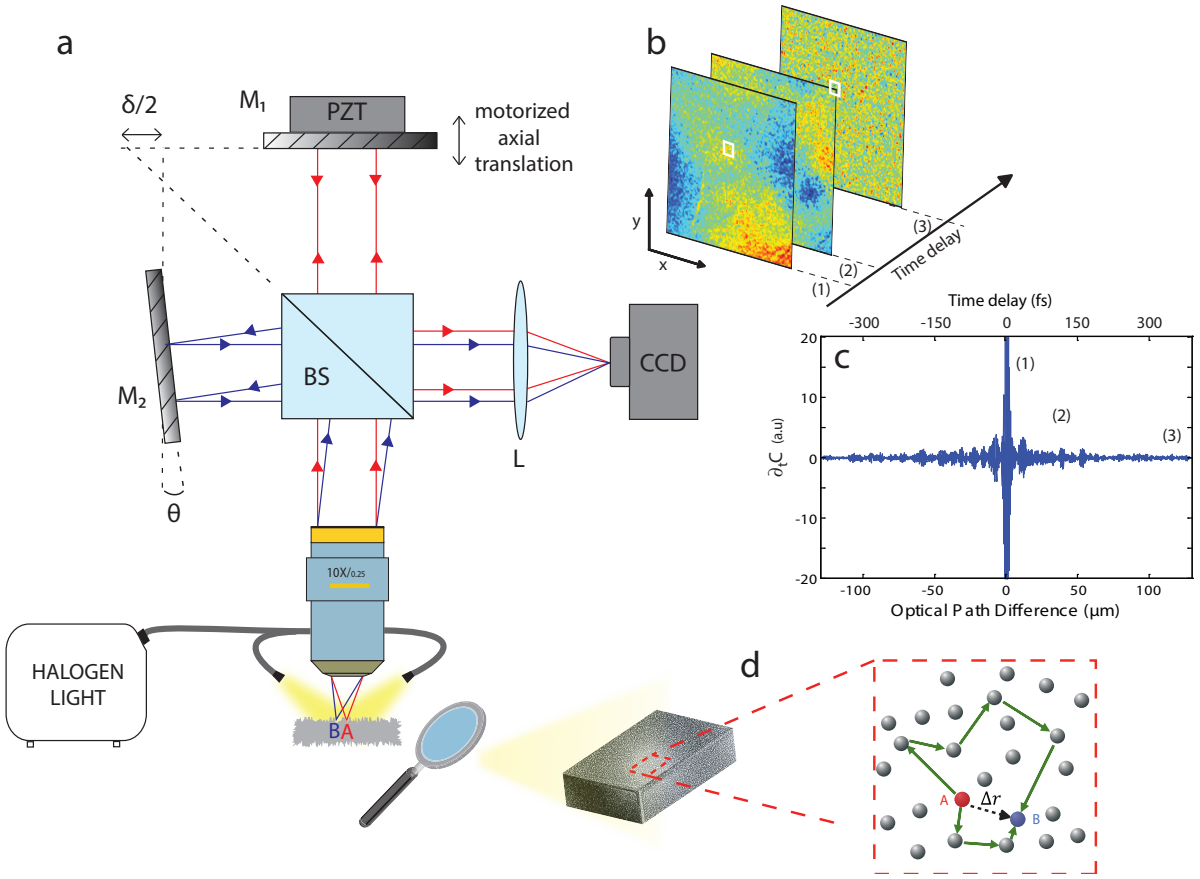

Figure 4.5: Passive measurement of the focused reflection matrix at the surface of a diffusive sample [40]. (a) Experimental set up: a broadband incoherent light source isotropically illuminates a scattering sample. The spatio-temporal correlation of the scattered wave field is extracted by means of a Michelson interferometer and recorded by a CCD camera. (b) Examples of full-field interferograms acquired at different OPDs. (d) Example of correlation function $C(\mathbf{r}_A, \mathbf{r}_B, t)$ acquired by one pixel of the CCD camera. (e) For infinite integration time, this quantity converges towards the impulse response $R(\mathbf{r}_A, \mathbf{r}_B, t)$ between these two virtual sensors A and B located at the surface of the sample and conjugated with the same pixel of the camera.

To eliminate the effect of absorption, we normalize the measured intensity by $P(\Delta r = 0, t)$ [251]. Figure 4.6(c) shows the resulting normalized intensity profile, $P(\Delta r, t)/P(0, t)$, at different times of flight. Not surprisingly, we retrieve the feature of a diffusive halo whose spatial extent increases with time. Now that we have qualitatively observed the diffusive spreading of the mean intensity, we aim to precisely characterize the scattering properties of the medium with a quantitative measurement of a transport parameter, the diffusion constant D.

In the diffusive regime, $P(\Delta r, t)$ can be expressed as the sum of two components. The first contribution is the incoherent average of the intensity of each individual scattering path, P_{inc}. In real (position) space, P_{inc} describes the spatio-temporal spreading of the wave energy density inside the sample – the so-called *diffuse halo*. This spreading can be directly quantified by measuring $w(t)$, the *transverse width* of $P_{\text{inc}}(\Delta r, t)$ [30, 251]. $P_{\text{inc}}(\Delta r, t)$ can be expressed as

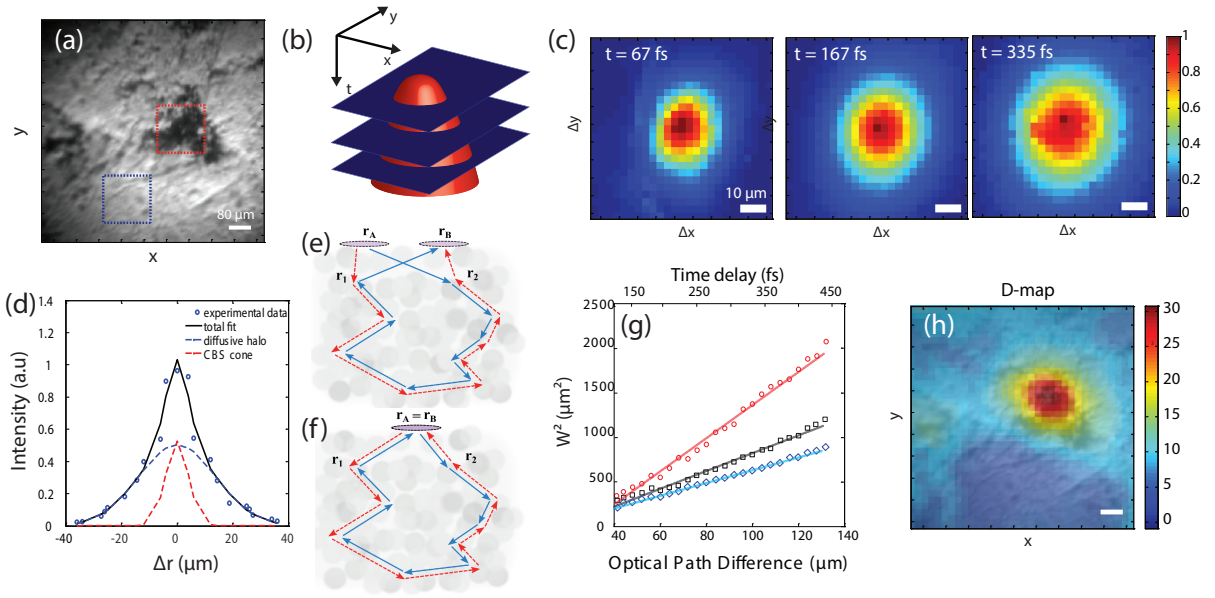

Figure 4.6: Imaging of the diffusion constant in a scattering layer heterogeneous in disorder. (a) Microscopic image of the ZnO scattering layer. (b) Sketch of the spatio-temporal diffuse intensity and its 2D spatial sections for different times of flight. (c) Measured spatial distribution of the mean intensity at different times-of-flight t. Each intensity map has been renormalized with its maximum. (d) Spatial intensity profile (blue disks) obtained at t =150 fs fitted with the sum of two gaussian curves (continuous black line) that account for the incoherent intensity (blue dashed line) and the coherent backscattering peak (red dashed line). (e) Coherent backscattering arises from interference between reciprocal paths. Pink oblongs represent the size of virtual sources/receivers at $\mathbf{r}_A$ and $\mathbf{r}_B$. (f) When source and receiver coincide, constructive interference is maximized. Sketch of the spatio-temporal diffuse intensity and its section for $\Delta r = 0$. (g) Time evolution of the mean-squared width $w^2(t)$ of the diffusive halo averaged over the whole sample surface (black squares), over areas surrounded by the blue dashed square (blue diamonds) and the red dashed square (red circles) in (a). (h) Superimposition of the measured diffusion constant map onto the sample image. The color scale is in $\mathrm{m}^2.\mathrm{s}^{-1}$.

follows [252]:

$$P_{\mathrm{inc}}(\Delta r, t) = P(0,t)\exp\left[-\Delta r^2/w^2(t)\right], \tag{4.4}$$

with

$$P(0,t) = (ce^{-t/\tau_a})/[(2\pi^{3/2})w^3(t)], \tag{4.5}$$

the probability of return to the origin, and

$$w^2(t) = 4D_B t. \tag{4.6}$$

D_B is the Boltzmann diffusion coefficient [251, 252], τ_a is the absorption time, and c the speed of light in the sample.

The second contribution to $P(\Delta r, t)$ is the coherent intensity

$$P_{\mathrm{coh}}(\Delta r, t) = P_{\mathrm{coh}}(0,t)F(\Delta r).$$

This factor is a correction to the diffusion approximation to account for *weak localization* [41, 42] in which waves travelling along pairs of reciprocal paths in opposite directions undergo constructive interference [Figs. 4.6(e) and (f)]. Experimentally, the effect of weak localization can be observed as *coherent backscattering* (CBS) [41, 42] – a peak-shaped enhancement $F(\Delta r)$ in the spatial distribution of average backscattered intensity. The CBS peak is maximum at $\Delta r = 0$, and its enhancement factor, A, can be defined by the relation $P_{\text{coh}}(0,t) = (A-1)P_{\text{inc}}(0,t)$. While in **k**-space this coherent back-scattering peak narrows as time increases [43, 253–255], in real-space its shape is stationary [30, 256, 257]. Ideally, for an experiment with point-like sources and detectors on the medium surface, this real-space CBS peak would have the form [256]

$$F(\Delta r) = [\sin(k\Delta r)/k\Delta r]^2 \exp(-\Delta r/\ell_s). \tag{4.7}$$

The width of the CBS peak would then scale as $\lambda/2$ or ℓ_s, the scattering mean free path. The enhancement factor is theoretically of $A = 2$ in the diffusive regime. Here, however, the CBS peak shape is dictated by the impulse response H of our imaging system such that the peak is widened [49]:

$$F(\Delta\mathbf{r}) \propto |H{*}H|^2(\Delta\mathbf{r}), \tag{4.8}$$

and the enhancement factor is reduced:

$$A = 1 + |H{*}H|^2(\Delta\mathbf{r}=\mathbf{0})/[|H|^2 \circledast |H|^2](\Delta\mathbf{r}=\mathbf{0}), \tag{4.9}$$

The symbols $*$ and $\circledast$ denote convolution and correlation products over $\Delta\mathbf{r}$, respectively.

Thus, for conventional diffusion, $P(\Delta r, t)$ has time-dependent diffuse halo such that:

$$\frac{P(\Delta r,t)}{P(0,t)} = \frac{1}{A} e^{-\Delta r^2/w^2(t)} + \left(1 - \frac{1}{A}\right) F(\Delta r). \tag{4.10}$$

In our configuration, this quantity has the following shape at a given time-of-flight [see Fig. 4.6(d)]: a narrow, steep peak (the coherent contribution), on top of a wider pedestal that widens with time (the incoherent contribution). To quantify the energy spread in each sample, the experimental $P(\Delta r,t)/P(0,t)$ was fit with Eq. 4.10. The characteristic size w^2 of the incoherent background directly accounts for the spatial extent of the diffusive halo. A linear fit of W^2 versus time [Fig. 4.6(g)] allows an estimation of the diffusion constant average over a field-of-view of 5 mm^2: $< D(\mathbf{r}) >= 1425$ m^2.s^{-1}. The field-of-view being at least one order of magnitude larger than the typical scale at which the concentration of scatterers fluctuates [Fig. 4.6(a)], such a measurement does not provide a satisfying characterization of the disorder in the scattering sample. To cope with this issue, a local approach is needed. Instead of considering the mean intensity over the whole sample surface, one can average the intensity over over sliding windows of 100×100 μm^2. The spatial extent w^2 of the diffusive halo in each window is fitted linearly over time and yields an estimation of the diffusion constant at the center of each window. The map of the diffusion constant is superimposed to the reflectivity image of the scattering medium in Fig. 4.6(h). A qualitative agreement is found between the two images since the diffusion

constant is larger in areas where the concentration in scatterers is lower. D is actually proportional to the transport mean free path l_t which itself scales as the inverse of the concentration of scatterers [258]. However, both images bring different information since the microscope image is only related to the concentration of scatterers at the surface of the medium whereas the diffusion constant also depends on the nature of disorder below the surface. A 3D image could thus be built from the focused reflection matrix but it would require inversion schemes like in optical diffuse tomography [152].

5 Perspectives

In this Chapter, we have shown how the focused reflection matrix paves the way towards a quantitative imaging process of the inspected medium. On the one hand, the long-scale fluctuations of the wave velocity $c(\mathbf{r})$ can be imaged in the single scattering regime through a self-portrait of the focusing process at any point $\mathbf{r}$ of the medium. On the other hand, in the multiple scattering regime, a map of the diffusion constant $D(\mathbf{r})$ can be measured by investigating the focused reflection matrix at the sample surface.

Beyond the optimization of each approach through more elaborated inversion schemes, a longer-term perspective for quantitative MI is to fill the gap between these two asymptotic scattering regimes by coupling both approaches. To that aim, the following strategy can be envisioned: (i) use the available wave velocity model to build a focused reflection matrix $\mathbf{R_{rr}}$ associated with a set of resolution cells mapping the volume of interest; (ii) perform a Born development of $\mathbf{R_{rr}}$ to retrieve the Green's matrix between each of those cells [50]. From this set of Green's functions, a high-resolution map of the wave celerity and transport parameters could be obtained throughout the medium. Of course, the crucial point of this strategy is the Born series of $\mathbf{R_{rr}}$ that requires the optimization of a large set of free parameters, namely the $\mathbf{t}-$matrix of each resolution cell [259] and the whole coefficients of the Green's matrix. Nevertheless, a perturbative approach in a weakly scattering regime would be an adequate starting point for this ambitious aim.

CHAPTER 5

Matrix approach of Wave Transport: From the Diffusive Regime to Anderson Localization

Publications

- A. Aubry, L.A. Cobus, S.E. Skipetrov, B.A. van Tiggelen, A. Derode, and J.H. Page, *Recurrent Scattering and Memory Effect at the Anderson Localization Transition*, Phys. Rev. Lett. **112**, 043903 (2014)
- B. Gérardin, J. Laurent, A. Derode, C. Prada, and A. Aubry, *Full Transmission and Reflection of Waves Propagating through a Maze of Disorder*, Phys. Rev. Lett. **113**, 173901 (2014)
- L. A. Cobus, S. E. Skipetrov, A. Aubry, B. A. van Tiggelen, A. Derode, and J. H. Page, *Anderson mobility gap probed by dynamic coherent backscattering*, Phys. Rev. Lett. **116**, 193901 (2016)
- B. Gérardin, J. Laurent, P. Ambichl, C. Prada, S. Rotter, and A. Aubry, *Particle-like wave packets in complex scattering systems*, Phys. Rev. B **94**, 014209, (2016)
- L. A. Cobus, G. Maret, and A. Aubry, *Crossover from renormalized to conventional diffusion near the 3D Anderson localization transition for light*, Phys. Rev. B **106**, 014208 (2022)

In a disordered medium, a classical approach is to consider the trajectory followed by a wave as a Brownian random walk. After a few scattering events, the spatio-temporal evolution of the mean intensity is governed by the diffusion equation. However, this classical picture neglects interference effects that may resist the influence of disorder. On the one hand, constructive interference between reciprocal multiple scattering paths enhances the probability for a wave to come back close to its starting point as compared to classical predictions: this phenomenon is known as weak localization. Hence, interference can slow down and eventually stop the diffusion process, giving rise to Anderson localization [44, 45, 260–262]. On the other hand, it can also help waves to find a way through a maze of disorder [263]. Actually, a properly designed combination of incident waves can be completely transmitted through or reflected by a strongly scattering medium, as suggested by Dorokhov and others more than thirty years ago [3, 264–266]. To investigate those intriguing phenomena, a matrix formalism is particularly appropriate when the wave field can be controlled by transmission or reception arrays of independent elements. Since an inhomogeneous medium can be treated as one realization of a random process, some aspects of random matrix theory [3, 4] may be fruitfully applied to wave transport, in particular to retrieve the open and close scattering channels [5]. Moreover, the reflection matrix provides many fundamental insights to study the transition between the diffusive and localized regimes. In particular, we will show how it provides a unique tool to probe the recurrent scattering loops [47], the coherent back-scattering cone [48] and the renormalization of the diffusion constant [49] at the onset of 3D Anderson localization.

1 Full transmission and reflection of waves in the diffusive regime

In order to address the open or closed channels (*i.e.*, to achieve full energy transmission or reflection) across a diffusive medium, one has to perform a complete measurement of the scattering matrix $\mathbf{S}$. The $\mathbf{S}$-matrix relates the input and output of the medium [3]:

$$\mathbf{S} = \begin{pmatrix} \mathbf{R} & \mathbf{T'} \\ \mathbf{T} & \mathbf{R'} \end{pmatrix} \tag{5.1}$$

It fully describes wave propagation across a scattering medium. It can be generally divided into blocks containing transmission and reflection matrices, $\mathbf{T}$ and $\mathbf{R}$, with a certain number N of input and output channels. Initially, random matrix theory has been successfully applied to the transport of electrons through chaotic systems and disordered wires [3]. However, the confrontation between theory and experiment has remained quite restrictive since specific input electron states cannot be addressed in practice. On the contrary, a coherent control of the incident wave-field is possible in classical wave physics. Several works have demontrated the ability of measuring the $\mathbf{S}$-matrix, or at least some of its subspaces, in disordered media, whether it be in acoutics [8, 18, 267], electromagnetism [268, 269] or optics [10, 11, 19, 104, 270].

The existence of open channels has been revealed by investigating the eigenvalues τ of the Hermitian matrix $\mathbf{T}\mathbf{T}^\dagger$. Theoretically, their distribution should follow a bimodal law [3, 264,

265]:

$$\rho_b(\tau) = \frac{g}{2\tau\sqrt{1-\tau}} \tag{5.2}$$

The bimodal law exhibits two peaks [see Figs. 5.1(c)].. The highest one, around $\tau \sim 0$, correspond to closed (*i.e.* strongly reflected) eigenchannels. At the other end of the spectrum ($\tau \sim 1$), there are g open eigenchannels. $g = N\ell_t/L$ is the dimensionless conductance [271], L is the sample thickness. By exciting selectively open or closed channels, a nearly complete transmission [272], reflection or absorption [273] of waves can be achieved. It means that a designed wave-front can be fully transmitted or, on the contrary, fully reflected by a scattering medium, which is in total contradiction with the classical diffusion picture. Although some indirect evidence of bimodality have been pointed out experimentally [270, 274–276], these remarkable interference effects had never been directly observed so far. Indeed, the bimodal distribution relies on the conservation of energy (*i.e.* $\mathbf{S}$ is a unitary matrix). In other words, all the channels should be addressed at the input and measured at the output [277]. In optical experiments, the finite numerical aperture of the illumination and detection systems limits the angular coverage of the input and output channels [278]. In acoustics or electromagnetism, the spatial sampling of measurements has not been sufficient to have access to the full $\mathbf{S}-$matrix so far [18, 267, 268].

During his PhD thesis [5, 279], Benoît Gérardin performed with Jérôme Laurent experimental measurements of the full $\mathbf{S}$-matrix across a disordered elastic wave guide [see Figs. 5.1(a) and (b)]. To that aim, laser-ultrasonic techniques have been used in order to obtain a satisfying spatial sampling of the field at the input and output of the scattering medium. The unitarity of the $\mathbf{S}-$matrix is investigated [Fig. 5.1(c)] and the eigenvalues of the transmission matrix are shown to follow the expected bimodal distribution [Fig. 5.1(d)]. Moreover, full experimental transmission and reflection of waves propagating through disorder have been achieved. The wave-fields associated to the open and closed channels are monitored within the scattering medium by laser interferometry to highlight the interference effects operating in each case [Fig. 5.2].

In a follow-up study [7] and in collaboration with Stefan Rotter, we then showed how a system-specific combination of fully open or closed channels can lead to particle-like wave packets that remain focused in time and space throughout the entire scattering process. Such particle-like scattering states [6] are eigenstates of the Wigner-Smith time-delay matrix [280, 281]:

$$\mathbf{Q} = \frac{i}{2\pi}\mathbf{S}^\dagger\partial_f\mathbf{S}, \tag{5.3}$$

where ∂_f denotes the derivative with respect to the frequency f.

Beyond the diffusive regime, the transition towards Anderson localization leads to an extinction of fully opened eigenchannels [3, 264, 265], as experimentally confirmed by [268], with electromagnetic waves. Subsequently, we extended this matrix approach of wave transport by investigating the 3D Anderson transition in a reflection configuration. The reflection matrix is actually a key tool to highlight interference phenomena such as recurrent scattering and coherent backscattering at the onset of Anderson localization.

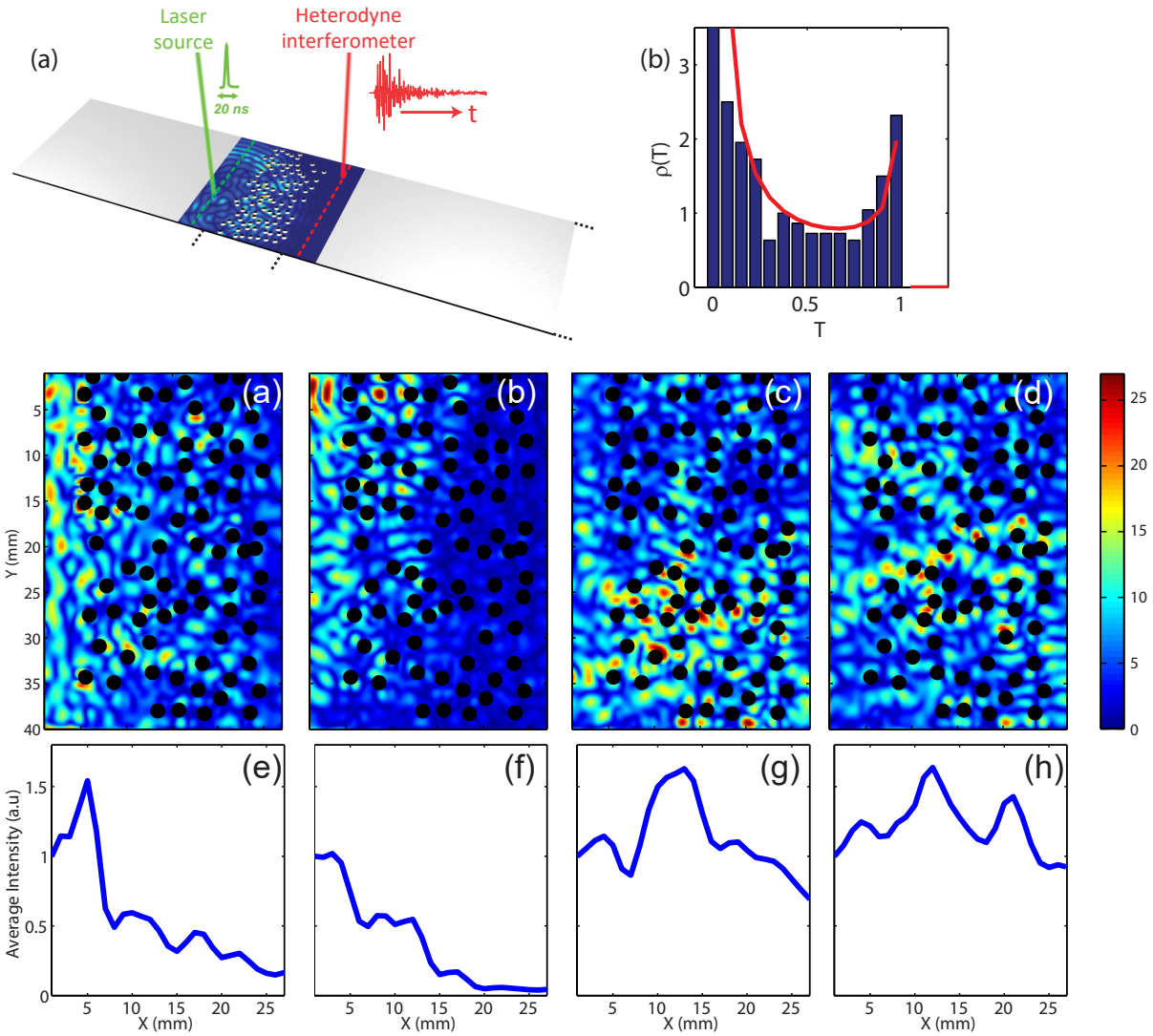

Figure 5.1: Measuring the scattering matrix with laser-ultrasonic techniques [5]. (a) Experimental set up. The $\mathbf{S}-$matrix is measured in the time-domain, between two arrays of points placed 5 mm away from each side of the disordered slab. Flexural waves are generated on each point by a pulsed laser *via* thermo-elastic conversion. The normal component of the plate vibration is measured with an interferometric optical probe. (b) Real part of the $\mathbf{S}$-matrix measured at $f = 0.36$ MHz. The black lines delimit transmission and reflection matrices as depicted in Eq. 5.1. (c) Eigenvalues in the complex plane of the measured (red dots) and normalized (blue squares) scattering matrices, respectively. The black continuous line denotes the unit circle. (c) Transmission eigenvalue histogram, $\rho_b(T)$, is compared to the bimodal law ρ_b (red continuous line, Eq. 5.2).

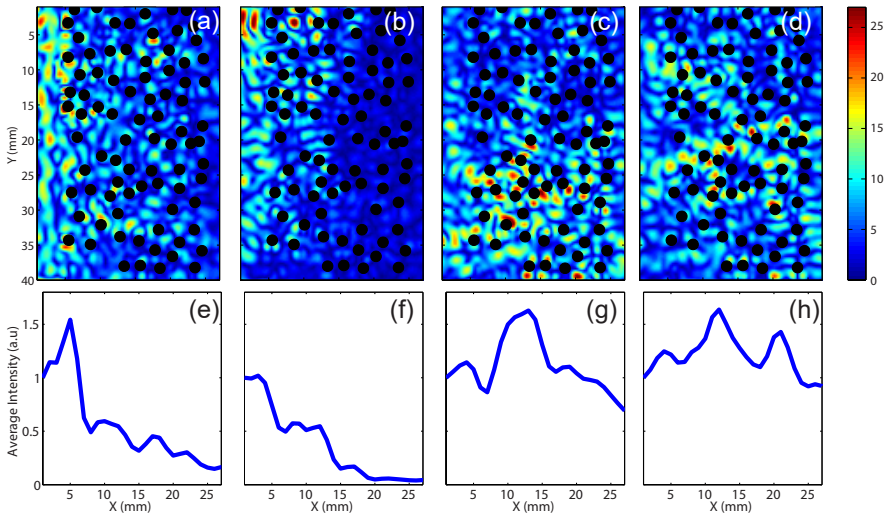

Figure 5.2: Probing the wave-fields of open and closed eigenchannels within the scattering medium [5]. Absolute value of the wave-field in the scattering medium at $f = 0.36$ MHz associated with (a) an incident plane wave, (b) a closed eigenchannel, (c) an open eigenchannel deduced from the measured $\mathbf{S}$-matrix and (d) an open eigenchannel deduced from the normalized $\hat{\mathbf{S}}$-matrix. The corresponding intensities averaged over the wave guide section (y-axis) are shown versus depth x in lower panels (e)-(h).

2 Recurrent Scattering and Coherent Backscattering at the Anderson transition

Since its discovery in 1958 [44], Anderson localization has been the subject of intense research and debate. This unusual phenomenon can be described as the suppression or halting of wave propagation, arising solely from wave interference effects caused by disorder [44, 282, 283]: instead of spreading diffusely from the source, a wave packet remains localized in its vicinity on a length scale given by the localization length ξ. The transition at a mobility edge between diffuse and localized behavior is predicted to exist only in three-dimensional media [284] and occurs when the scattering is sufficiently strong, i.e., when $k\ell_t sim1$ (with k the wave number in the scattering medium) [45]. The requirement that waves must interact with a critical amount of disorder makes the experimental observation of localization in 3D notoriously difficult. Several experiments in optics have shown deviations from diffuse behavior in 3D strongly scattering samples [285–288] but had been subject to controversy. However, later reinterpretation of all of these experiments found that the results could also be explained either by absorption [289, 290] or fluorescence [291], both of which can mimic signatures of localization. Meanwhile, Anderson localization in 3D was unambiguously observed using with cold atoms in random potentials [254, 292, 293] and acoustic vibrations in elastic networks [46].

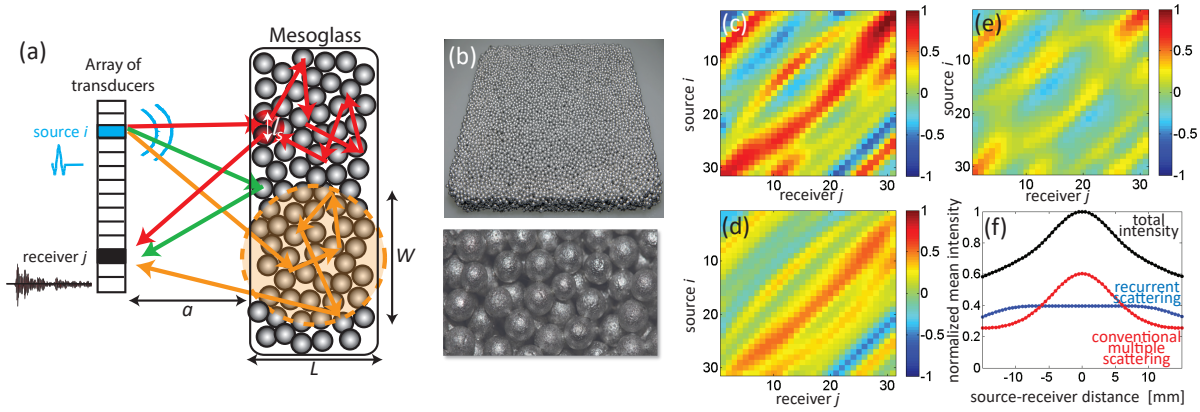

Figure 5.3: Recurrent scattering and memory effect at the Anderson transition [47]. (a) Experimental set up. Examples of a single scattering path (green arrows), of a recurrent scattering path (red arrows) and of a conventional multiple scattering path (orange arrows) are drawn. (b) Mesoglass (sample L1). (c) Real part of the matrix $\mathbf{R}_{uu}$ at time $t = 185$ μs and frequency $f = 1.25$ MHz for a given realization of disorder. (d) Real part of the recurrent scattering contribution $\mathbf{R}_{\mathrm{RS}}$. (e) Real part of the conventional multiple scattering contribution $\mathbf{R}_{\mathrm{MS}}$. (d) Spatial mean intensity profiles at the same time and frequency.

During these last ten years, in collaboration with Laura Cobus, John Page, Sergey Skipetrov, Bart van Tiggelen, and Arnaud Derode, we highlighted new mesoscopic aspects of Anderson localization by investigating the reflection matrix $\mathbf{R}_{uu}$ associated with such a mesoglass [47]. The sample under study [Fig .5.3(b)] had been priorly characterized by means of transmission measurements [205]: phase velocity $v_p \sim 2.8$ mm/μs and mean free path $\ell_s \sim 1.3$ mm, such that $k\ell_s \sim 3$. Transverse confinement measurements [46] indicated that the waves are localized

between 1.2 and 1.25 MHz (mobility edges), with $\xi < L$ in the middle of this band. ξ here designs the localization length.

The experimental set up and procedure are described in Ref. [47]. Surprisingly, $\mathbf{R}_{uu}$ displays, in the far-field, a deterministic coherence along its antidiagonals in a way similar to single scattering[18] [see Fig. 3.1(d)], but at much longer times of flight. Another surprising result is shown by Fig. 5.3(f) which displays the corresponding backscattered intensity,

$$I(\Delta\theta, t) = \left\langle |R(\mathbf{u}_{\text{out}}, \mathbf{u}_{\text{in}}, t)|^2 \right\rangle_{\{(\mathbf{u}_{\text{out}}, \mathbf{u}_{\text{in}}) || \mathbf{u}_{\text{out}} - \mathbf{u}_{\text{in}}| = \Delta u\}} \tag{5.4}$$

as a function of the backscattering angle $\Delta\theta = \Delta u/a$. In the multiple scattering regime ($v_p t \gg \ell_s$) and far from localization ($k\ell_s \gg 1$), the intensity backscattered at the source is expected to be twice as large as the intensity far from the source because of the coherent backscattering phenomenon [41–43, 294]. Although we do indeed obtain this coherent backscattering peak, the enhancement factor is clearly smaller than 2. We interpret this as a sign of a large contribution from recurrent scattering trajectories [red arrows in Fig. 5.3(a)] for which the first and the last scatterers are separated by less than one mean free path ℓ_s. Recurrent scattering, just like single scattering, contributes to a background intensity that is independent of the distance between source and receiver. The interference between a wave and its reciprocal counterpart is indeed always constructive for these two contributions.

The very large recurrent scattering contribution seen in our experiment sheds new light on the long-range spatial coherence observed in Fig. 5.3(c). In the strongly scattering regime, the backscattered field can be decomposed into a sum of two terms:

• A recurrent scattering contribution [red arrows in Fig. 5.3(a)] which displays the same statistical properties as the single scattering one. This contribution accounts for the deterministic coherence along the antidiagonals of $\mathbf{R}_{uu}$ in Fig. 5.3(c).

• A *conventional* multiple scattering contribution [orange arrows in Fig. 5.3(a)] for which the first and last scattering events are separated by more than one mean free path. In this case, the memory effect is restricted to the angular width of the backscattering cone [295, 296].

Previous studies have taken advantage of the memory effect to separate single and multiple scattering [18, 24, 102]. Here, the previous method is significantly extended to enable $\mathbf{R}_{uu}$ [Fig. 5.3(c)] to be separated into a recurrent scattering component $\mathbf{R}_{RS}$ [Fig. 5.3(d)] and a conventional multiple scattering component $\mathbf{R}_{MS}$ [Fig. 5.3(e)]. Once the separation of these two contributions is performed, one can compute the corresponding mean backscattered intensity [Fig. 5.3(d)]. Whereas recurrent scattering leads to a flat intensity profile, the conventional multiple scattering intensity exhibits a coherent backscattering cone. The recovery of an enhancement factor close to two demonstrates that recurrent scattering was indeed responsible for reducing the enhancement factor seen for the total intensity I [297] [Fig. 5.3(d)].

The recurrent scattering intensity I_{RS} is here a far-field reflectance that can be directly related to the probability $P(\Delta r = 0, z = 0, t)$ [Eq. 4.5] for a wave to return to the spot at which it entered the scattering sample, such that $I_{RS} = D|\partial_z P(\Delta r = 0, z, t)|_{z=0}|$ [252]. From a theoretical point of view, this return probability is a key quantity in the description of the

renormalization of the diffusion constant in the self-consistent theory of localization [260, 261]. The decay of the recurrent scattering intensity with time bears particular signatures of Anderson localization. In the diffusive regime, the following power law decay is expected for the return probability at the surface of the sample and the recurrent scattering intensity [287]:

$$P(\Delta r = 0, t) \propto 1/t^{3/2} \text{ and } I_{RS}(t) \propto 1/t^{5/2}. \tag{5.5}$$

For stronger disorder ($k\ell_t \sim 1$), an increase in the return probability can cause a renormalization (decrease) of the diffusion coefficient D. The self-consistent theory of localization predicts that, in 3D, D scales as [44, 282]

$$D \approx D_0 \ell^* \left(\frac{1}{\xi} + \frac{1}{L} + \frac{1}{L_A} \right), \tag{5.6}$$

where D_0 is the diffusion coefficient before rescaling, ξ is the localization length, L is the system size, and L_A is the absorption length. In reflection, the effective system size L can be said to be the spatial extent of the wave energy $L(t) = \sqrt{6D(t)t}$ [287]. Thus, before reaching localization ($L << \xi$) and if absorption is negligible ($L << L_a$), Eq. 5.6 leads to the following time-dependence for the diffusion coefficient:

$$D(t) \simeq \frac{(D_0 \ell^*)^{2/3}}{(6t)^{1/3}}. \tag{5.7}$$

This expression corresponds to a sub-diffusive regime in which the diffusion coefficient is successively renormalized as the propagating waves undergo recurrent scattering events – a process which goes hand in hand with an increase in the return probability and which, in principle, results in Anderson localization [260, 261]. Replacing D_B in Eq. 4.4 by the renormalized diffusion coefficient $D(t)$ gives the following scaling for the return probability in the sub-diffusive regime:

$$P(\Delta r = 0, t) \propto t^{-1} \text{ and } I_R(t) \propto t^{-3/2}. \tag{5.8}$$

Figure 5.4(a) displays the typical time dependence of $I_R(t)$ in the 1–2 MHz frequency range. At all frequencies, $I_R(t)$ can be described by a power law $1/t^\alpha$. We recover the exponent $\alpha = 5/2$ at 1.8 MHz, characteristic of the diffuse regime, and observe its shift to 2 at 1.225 MHz as expected in the localized regime. Furthermore, we observe a strikingly slower decay at $f = 1.2$ MHz, which corresponds to a mobility edge and where α reaches a value close to 1. This extremely slow decay at the mobility edge may result from an interplay of criticality with the band structure of the sample [298].

To probe the Anderson transition, one can also investigate the conventional multiple scattering contribution and probe the dynamics of the coherent back-scattering cone [48]. Indeed, in far-field conditions, its shape is the transverse Fourier transform of the mean intensity Green's function $P(\Delta r, t)$ inside the medium. In other words, the width $\Delta\theta(t)$ of the dynamic coherent back-scattering peak behaves, roughly speaking, as the inverse width $w(t)$ of the diffuse halo at the surface of the sample: $\Delta\theta(t) \sim \lambda/w(t)$. In the diffusive regime [see green curve in

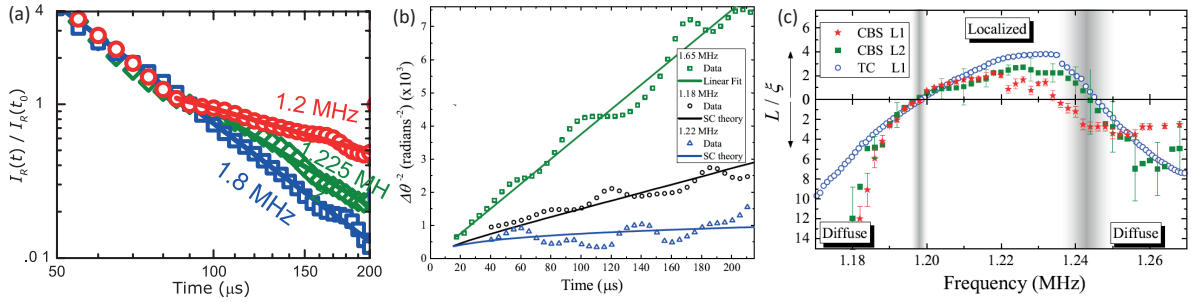

Figure 5.4: Probing recurrent scattering and coherent backscattering at the onset of Anderson localization [47, 48]. (a) Time evolution of the recurrent scattering intensity $I_R(t)$ in the diffusive regime ($I_R(t) \propto t^{-2.5}$ at 1.8 MHz), in the localized regime ($I_R(t) \propto t^{-2}$ at 1.225 MHz) and in the critical regime ($I_R(t) \propto t^{-1}$ at 1.2 MHz). (b) Inverse square of the coherent back-scattering peak width $\Delta\theta^{-2}$ versus time in the diffusive regime ($f = 1.65$ MHz, $D_B = 0.7$ mm$^2/mu$s extracted from the fit of Eq. 5.9), sub-diffusive regime ($f = 1.18MHz$, Eq. 5.10), and localized regime ($f = 1.22$ MHz, Eq. 5.11). (c) The ratio of sample thickness L to the localization (correlation) length ξ obtained from fits to experimental coherent back-scattering profiles (red stars, green squares) and transverse confinement (transmission) data (open circles). Fuzzy vertical gray lines show our estimates of mobility edges.

Fig. 5.4(b)], the cone width shrinks with time, as expected by the diffusion theory [Eq. 4.6]:

$$\Delta\theta^{-2}(t) \sim \frac{4D_B t}{\lambda^2} \tag{5.9}$$

In the sub-diffusive regime [see black curve in Fig. 5.4(b)], the halo growth and cone shrinking slow down due to the renormalization of the diffusion constant [Eq. 5.7] induced by recurrent scattering loops:

$$\Delta\theta^{-2}(t) \sim \left(\frac{w(t)}{\lambda}\right)^2 \propto \frac{(D_o \ell_t t)^{2/3}}{\lambda^2}. \tag{5.10}$$

At last, in the localized regime [see blue curve in Fig. 5.4(b)], $w(t)$ cannot exceed a value on the order of the localization length ξ in the localized regime and the cone width saturates:

$$\Delta\theta^{-2}(t) \sim \left(\frac{\xi}{\lambda}\right)^2. \tag{5.11}$$

More quantitatively, systematic fits of self consistence theory [261] to the data [48] allowed to determine the frequency dependence of the localization (correlation) length ξ [see Fig. 5.4(c)]. The Anderson mobility gap is clearly visible in between, whereas the wave transport is subdiffusive for frequencies below 1.20 and above 1.24 MHz. The study of Anderson transition by means of the reflection matrix instead of transmission measurements [46, 299] ensured a sufficiently strong signal throughout the mobility gap. This is a significant advance, as previous experiments were only able to reveal a single mobility edge. This approach, made possible by a combination of modern experimental techniques with a careful theoretical description, can be extended to other classical waves and a natural question is whether similar phenomena could

also be observed for light.

3 Cross-over from renormalized to conventional diffusion near the 3D Anderson localization transition for light

Indeed, the ongoing lack of evidence for 3D localization of light motivated a resurgence of theoretical work in search of explanations. Some argued that none of the materials tested so far scatter light strongly enough to achieve localization [291, 300, 301]. Others proposed that the onset of localization is prevented by the dipole-dipole interactions between close-packed scatterers [**John1992**, 302–307] which are inherent to the vector nature of light [302, 308]. This is in fact a relatively old idea [**John1992**], recently revived by Skipetrov and Sokolov to predict that 3D localization should exist for (vector) elastic waves, but not necessarily for light [302, 309]. Around the same time, Naraghi *et al.* proposed a theory in which localization and near-field coupling are modeled as competing effects [304, 305]. The model predicts multiple regimes of transport as the waves explore the medium. In particular, this includes a crossover from a subdiffusive/critical regime to conventional diffusion, which is brought about when near-field effects induce an opposing energy 'leak' which destroys localization. Supporting this picture are experimental measurements of the path length distribution of the optical energy flux reflected from white powder [305]. These measurements, however, are not necessarily independent of absorption or fluorescence, and can not indicate whether or not localization is attained prior to the crossover.

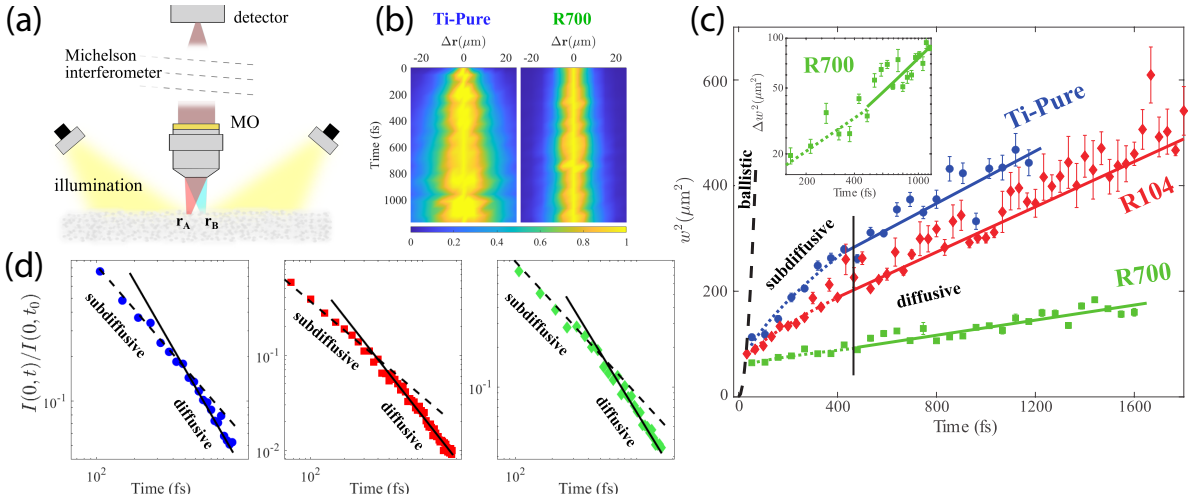

Figure 5.5: Probing the cross-over from renormalized to conventional diffusion [49]. (a) Low-coherence interferometry measures the cross-correlation between points $\mathbf{r_A}$ and $\mathbf{r_B}$ at the sample surface [40]. (b) $I(\Delta r, t)/I(0, t)$ shown for samples Ti-Pure and R700. (c) Transverse width $w^2(t)$ for all three samples (symbols). Linear fits to the data (solid lines) give D for each sample. In the subdiffusive regime ($t < \tau_c$), the data is fit with Eq. 5.11 (dotted lines). The ballistic light line (dashed black line), indicates the lower limit for $w^2(t)$. Inset: Δw^2 through the subdiffusion-diffusion crossover for R700 (log-log scale). (d) Return probability $P_R(t)$ normalized by its value at time $t_0 = 53$ fs for Ti-Pure (blue), R104 (red) and R700 (green). Lines following $t^{-3/2}$ (solid, diffusive) and t^{-1} (dashed, subdiffusive) are guides to the eye, not fits

To prove the existence of this crossover, Laura Cobus, during her post-doc, performed passive measurements of the reflection matrix [40] [see Fig. 4.5] for three different types of compressed TiO_2 powders: a pure anatase phase (Ti-Pure, $k_0\ell^* \sim 5-6$), and two types of rutile phase powders, R104 ($k_0\ell^* \sim 3-4$) and R700 ($k_0\ell^* \sim 2-3$) [310, 311]. Based on this measurement, the spatio-temporal behaviour of the wave energy density, $P(\Delta r, t)$, at the surface of the sample can investigated [Eq. 4.3]. Our experimental approach allows observations over an unprecedented range of times, and does not suffer from shot noise [49] and fluorescence effects which hampered previous experiments [300].

Figure 5.5(b) show the resulting normalized intensity profile, $P(\Delta r, t)/P(0, t)$, for samples Ti-Pure and R700. The difference between samples is immediately obvious: energy spreads more slowly in R700, the more strongly-scattering sample. To quantify the energy spread in each sample, the experimental $P(\Delta r, t)/P(0, t)$ was fit with Eq. 4.10. Figure 5.5(c) shows experimental resutls for $w^2(t)$ (solid symbols). We observe that $w^2(t)$ does not agree with the diffusive prediction of Eq. 4.6, especially at short times-of-flight ($t < 500$ fs). Compared with conventional diffusion, a key feature of the strong scattering regime ($k\ell^* \sim 1$) is the predominance of recurrent scattering 'loops', *i.e* an increased probability for waves to pass nearby areas that they have previously visited [47, 260, 261]. The time-dependence of this *return probability* can thus be directly quantified in the reflection geometry by observing the time-dependence of the back-scattered intensity at the source location. Figure 5.5(d) shows $P(\Delta r = 0, t)$ for all three samples. Comparison of our theoretical predictions [Eqs. 5.5 and 5.8] with the experimental data reveals the existence of a crossover between two transport regimes at a characteristic time $\tau_c \sim 450$ fs [Fig. 5.5(c)]. Before τ_c, $P(0, t) \propto t^{-1}$ which is characteristic of a regime in which the diffusion coefficient is continuously renormalized (falling into the more general category of *subdiffusion*). After the crossover ($t > \tau_c$), $P(0, t) \propto t^{-3/2}$ as expected for diffusion. Naraghi *et al.* [305] have predicted such a crossover, proposing that near-field coupling between scatterers constitutes a 'leak' of energy from propagating paths to evanescent channels. Contrary to theoretical predictions [305], the observed values of τ_c do not differ significantly in the different samples and do not scale with ℓ_t. This is likely due to variation in the near-field scattering cross-section in each sample; although each sample was compressed with the same force, differences in particle size/shape/chemical composition could cause these near-field losses to vary between samples.

In the study of localization, the return probability $P(0, t)$ is valuable as it is a key quantity in the theoretical description of the process of renormalization of the diffusion coefficient [260, 261]. However, $P(0, t)$ is not necessarily free from absorption, and can exhibit surprising results in the critical regime due to boundary conditions and source shape [47, 298]. It is thus unwise to rely on only $P(0, t)$ to distinguish between regimes. For this task, $w^2(t)$ is more reliable, being independent of all of the above issues [48, 251, 312], closely linked to D [251, 252, 312], and giving access to the very earliest times.

Figure 5.5(c) shows experimental results for $w^2(t)$. At long times of flight ($t > \tau_c$), $w^2(t)$ increases linearly with time, as expected in the diffusive regime. Linear fits to $w^2(t)$ give a direct measurement of D. The measured value of D for R700 ($D = 18 \pm 9$ m^2/s) is in excellent

agreement with previous wavelength-dependent measurements performed in transmission [310]. For $t < \tau_c$, $w^2(t)$ appears to be first quasi-ballistic ($t < 50$ fs), and then subdiffusive [287]. Fitting the experimental $w^2(t)$ curves with Eq. 5.10 confirms the scaling of $w^2(t)$ as $t^{2/3}$ for $t < \tau_c$. The subdiffusion-diffusion crossover can be more clearly seen by plotting $\Delta w^2 = w^2 - w_0^2$ on a log-log scale – this is shown for R700 in the inset of Fig. 5.5(c).

In conclusion, we have observed a clear crossover from a subdiffusive regime at early times to conventional diffusion at later times. By comparing both the return probability and $w^2(t)$ with predictions from the scaling theory of localization, we can conclude that the early-time subdiffusion arises from the renormalization of the diffusion coefficient, and thus falls into the more specific category of renormalized diffusion (a precursor to Anderson localization). This conclusion is supported by the near-field coupling model proposed by Naraghi *et al.* [304] to explain the subdiffusion-diffusion crossover. However, it remains unclear whether 3D localization of light can never be reached because the energy leak destroys the requisite long scattering paths, or if this effect can be overcome by structuring disorder, as a way of cancelling the impact of near-field coupling [306, 309, 313]. Interestingly, 3D Anderson localization has been recently predicted in hyperuniform dielectric networks [314], a new class of highly correlated but disordered photonic band gap materials. More generally, correlated disorder implies a complex transport phase diagram [315] whose transitions could in principle be revealed by our passive imaging method.

4 Perspectives

In this Chapter, we have shown how a matrix approach of wave propagation in complex media was a particularly relevant observable to chase after spectacular interference phenomena that survive to disorder. While these works have been originally motivated by a strictly fundamental interest, one can discuss about their potential relevance for imaging applications. Recurrent scattering loops that play a fundamental role in the Anderson transition are also far from being negligible in a much weaker scattering regime [50]. In particular, their contribution to the confocal signal in reflection imaging methods raises fundamental questions about the impact of recurrent scattering on the bias induced on our estimation of the medium reflectivity. Recurrent scattering loops are also responsible for the coherent back-scattering peak observed in the focused reflection matrix when virtual sensors are synthesized inside medium [31]. Preliminary works in granular media have shown that the width of this coherent backscattering peak is sensitive on aberrations undergone by the incident and reflected wave-fields. One exciting perspective is thus to investigate whether the coherent backscattering peak can be used as a guide star in the $\mathbf{D}-$matrix approach presented in Chapter 2.

With regards to random matrix theory, a recent study has investigated the deposition matrix $\mathbf{Z}$ [316] that links each input wavefront to the field distribution inside the medium. This matrix is actually closely related to the transmission matrix that we defined between the sensor and voxel bases in Chapter 2 and constitutes the Holy Grail for MI. In this work, Bender *et al.* [316] investigated the eigenvalue distribution of the operator $\mathbf{Z}\mathbf{Z}^\dagger$. On the one hand, they showed

that its eigenvalue distribution ρ_z is far from the bimodal law ρ_b [Eq. 5.2] which is only valid when input and output sensors are placed outside of the scattering medium. On the other hand, they showed that the eigenvalue distribution is far from the Marčenko-Pastur distribution [317] expected for a fully random matrix $\mathbf{Z}$. This discrepancy is the manifestation of long-range (C_2) correlations [318, 319] between the entries of the $\mathbf{Z}$-matrix. A future perspective would be to exploit such long-range correlations for wave imaging. In analogy with the distortion matrix that exploit the memory effect (C_1 correlations) [94, 95] to extract local focusing laws, the challenge will consist in defining a novel operator relying on those long-range correlations to build a satisfying estimator of the $\mathbf{Z}$-matrix.

At last, as already mentioned in Chapter 2, the generalized Wigner Smith operator introduced by the team of Stefan Rotter can be a powerful tool for imaging applications [192]. Instead of considering the frequency derivative of the $\mathbf{S}-$matrix in Eq. 5.3, this operator considers the derivative of $\mathbf{S}$ or of its subspaces over any control parameter in the experiment. For instance, it can be the position [192] or tilt [320] of a moving object, the measurement time [321] in dynamic scattering media, or the incident wave amplitude in non-linear media. The eigenvalue decomposition of $\mathbf{Q}$ enables to determine the wave-fronts that are the less or most sensitive to the variation of the control parameter. For imaging applications, time and amplitude will be particularly relevant parameters to probe the dynamics of the medium and map its non-linearities.

CHAPTER 6

Perspectives

In the next years, we will tackle the challenge of wave imaging in the deep diffusive regime. To that aim, we will extend the matrix tool we started to develop these last few years to the time domain. Indeed, to cope with multiple scattering, one should control all the spatial and temporal degrees of freedom provided by the scattering medium that we aim to image. The main goal is to overcome the penetration depth limit of conventional reflection imaging methods that typically scales as the transport mean free path ℓ_t at best [156]. To do so, several challenges remain to be addressed.

Ultra-fast measurement of a high-dimension reflection matrix

Ther first challenge is experimental and lies in the ultra-fast measurement of a high-dimension reflection matrix, especially for in-vivo imaging. With regards to ultrasound imaging, the frame rate was drastically increased ten years ago by the emergence of plane wave compounding [110]. Nevertheless, this is at the cost of a loss in resolution and contrast since the number of spatial degrees of freedom is limited by the number of plane waves used to insonify the medium. To reach a high-frame rate without sacrificing the image quality, one can take advantage of passive imaging methods developed in seismology. The same idea can be applied to ultrasound imaging. More precisely, we want to take advantage of spurious reflections and multiple scattering to retrieve a full reflection matrix from a single or a few illuminations with the aim of getting an optimized image quality at a high frame rate.

Passive imaging has already been applied to optical microscopy. Such a measurement gives access to a particularly high number of spatial degrees of freedom but the measurement time remains particularly prohibitive for in-vivo volumetric imaging ($\sim$mm^3). To circumvent this

problem, a novel apparatus, the so-called Matriscope, is currently developed for ultra-fast 3D matrix imaging [177]. It combines a set of incident wave-fronts at various optical wavelengths in order to measure a polychromatic reflection matrix in record time. In contrast with previous optical studies that recorded the reflection matrix at a single frequency [19] or time-of-flight [21, 23, 27], this polychromatic reflection matrix allows us to realize in post-processing: (*i*) a 3D confocal image of the sample reflectivity on millimetric volumes (1 mm^3 = 10^9 pixels) in an ultra-fast acquisition time (<1 s); (*ii*) an optimized compensation of both transverse and axial aberrations in post-processing. Compared to a time-gated reflection matrix that only allows a compensation of transverse aberrations (lateral variations of the optical index), the polychromatic reflection matrix gives access to many temporal degrees of freedom that can be exploited for tailoring complex spatio-temporal focusing laws. Such a complexity is required to focus light in depth whether it be numerically in post-processing or physically with wave-front shaping techniques.

Information theory for wave imaging

Indeed, the medium can be seen as a spatio-temporal lens that can typically convert the time information into spatial degrees of freedom [2], thereby potentially providing an enhanced spatial resolution compared to free space [38]. Before exploiting multiple scattering for focusing, one should beforehand assessed the medium complexity, *i.e* the number C of spatial and temporal coherence grains exhibited by the spatio-temporal focusing laws. To that aim, an information theory of wave imaging is needed. Our goal is to define an entropy based on the statistical properties of the reflection matrix [27]. This entropy would actually yield the equivalent of a Shannon number, i.e. the number C of spatial and temporal degrees of freedom that the medium can provide. By analogy with Shannon's general theory of communication [322], it would lead to a definition of the imaging capacity (or complexity) of the probed medium.

Deep matrix imaging

Once the number C of unknowns is assessed, the main challenge is, of course, the determination of complex spatio-temporal focusing laws for deep imaging. In sparse scattering media, one can use an iterative time reversal process on each scatterer that can be used as a guide star to converge towards the **T**-matrix linking each scatterer and sensors outside the medium. In random scattering media, the estimation of such complex wave-fronts is more problematic since it require isoplanatic patches whose dimension should be one order of magnitude larger than C in terms of resolutions cells. Yet, isoplanatic patches become smaller and smaller at large penetration depths and tends to a single speckle grain in the diffusive regime. To circumvent this fundamental problem, several strategies can be considered.

First, the training of numerical models designed to incorporate physical insights has already shown promising results, e.g by demonstrating the compensation of aberration in optical measurements [14] or predicting the transmission properties of thin diffusers [214]. Finding a way to

efficiently combine physical insights and learning approaches may be the key to retrieve transmission information from the **R**-matrix in multiple scattering media [213]. Using deep learning frameworks one can create physics inspired models for light propagation inside inhomogeneous media. The propagation equation, its invariants and/or its statistical properties can be incorporated into numerical models. For instance, for biological tissues in optics, where the scattering is anisotropic, light propagation is well modeled by a series of diffraction events by thin diffusers with free space propagation in between [215]. One could then envision models that mimic these effects using layers with trainable parameters. Once trained on a measured **D**-matrix, it can be used to predict the associated **T**-matrix.

Besides the specific case of biological media in optics, a layered approach is also particularly appropriate to develop an iterative reconstruction of the medium properties. Our strategy will be actually the following. Use the properties extracted at shallow layers to improve the propagation model at deeper layers. Preliminary ultrasound experiments in granular media have shown the merit of this strategy. In that perspective, the wave velocity tomography that we are currently developing in the framework of matrix imaging is crucial [31]. A precise knowledge of the wave velocity distribution at shallow layers favors the range of the memory effect at deeper layers and our ability to retrieve a precise estimation of the **T**-matrix beyond the transport mean free path.

Quantitative matrix imaging

The mapping of the wave velocity and scattering parameters is thus particularly important to build an accurate estimator of the $\mathbf{T}-$matrix inside the medium. Those quantities are also quantitative markers for biomedical diagnosis and also important monitoring parameters of tectonic motion and volcanic eruption in geophysics.

Chapter 3 has shown how the time-dependent focused reflection matrix paves the way towards a quantitative imaging process of the inspected medium. On the one hand, the long-scale fluctuations of the wave velocity $c(\mathbf{r})$ can be imaged in the single scattering regime through a self-portrait of the focusing process at any point $\mathbf{r}$ of the medium. On the other hand, in the multiple scattering regime, a map of the diffusion constant $D(\mathbf{r})$ can be measured by investigating the focused reflection matrix at the sample surface. Beyond the optimization of each approach through more elaborated inversion schemes, a longer-term perspective for quantitative matrix imaging is to fill the gap between these two asymptotic scattering regimes by coupling both approaches. Using the propagation movies as a feed-back, our strategy will be to make the propagation model converge towards the true wave velocity distribution. This will go in hand with a better estimation of the **T**-matrix, an optimized focusing process and, therefore, an ability to probe wave diffusion in depth.

Besides the precise estimation of the forward scattering component of the **T**-matrix, its Born development will be required to cope with the multiple scattering regime. To that aim, the idea is to decompose the **R**-matrix into its higher scattering orders, as we recently did in a weaker scattering regime [50]. Again, inversion algorithms and/or learning based methods will

be relevant tools to unscramble the different scattering orders of the **T**-matrix from the Born series of the **R**-matrix.

Dynamic matrix imaging

Beyond the fundamental multiple scattering issue, another problem we have not considered yet is the movement of the medium during the acquisition of the reflection matrix. Of course, the assumption of a static medium is everything but true especially for in-vivo applications, whether it be in optical microscopy or, to a lesser extent, in ultrasound imaging. In seismology, passive MI also implies the cross-correlation of seismic noise recorded over several months. Yet tides and temperature changes, for instance, can induce seismic velocity changes at a sub-daily time scale.

To cope with the dynamic features of the medium, two strategies can be followed. The first one is to limit the measurement time of the **R**-matrix at its minimum, as discussed above. The second one is to develop algorithms that consider the movement of the medium during the measurement of the **R**-matrix. Yet, for deep imaging, the latter number should be high in order to harness all the multiple scattering paths that the wave can undertake to focus deep inside the medium. Hence, a dynamic matrix approach of wave imaging is required for deep imaging. The movement of the medium can be characterized during the illumination sequence by cross-correlating each output image. Movement can then be compensated in order to build a beamforming adapted to the object trajectory.

Moving speckle can also be taken advantage of to optimally extract the **T**-matrix between sensors and medium voxels from reflection measurements. Moving speckle actually gives access to large number of speckle realizations at each voxel which can be used in return to extract an aberration phase law for each voxel of the medium without relying on any isoplanatic assumption [187].

Imaging the temporal fluctuations of the medium's reflectivity and wave velocity can provide a key information for probing the multicellular dynamics in optical microscopy [188], the blood flow or hemodynamic changes in functional ultrasound imaging [323]. Similarly, in seismology, the monitoring of the subsoil's mechanical properties over time is crucial for: (i) the prediction of hazardous events (volcanic eruption [324], earthquake [189], landslide, etc.); (ii) the evaluation of the impact of climate change on the glaciers [191]. For these various applications, our aim is to develop a Doppler mode of matrix imaging that would consist in mapping the temporal variations of the medium. Compared to standard differential imaging or speckle tracking methods, a matrix formalism can benefit from dedicated operators such as the generalized Wigner-Smith matrix [192] in order to discriminate the temporal fluctuations of reflectivity from the variations of the wave velocity distribution inside the medium. A matrix approach of dynamic imaging can thus provide a fine monitoring of the dynamics at work in the inspected medium. As a post-doc at the university of Auckland, Laura Cobus is currently investigating this topic in the context of ultrasound imaging.

A pluri-disciplinary approach

Based on these achievements, the final output of this research project will be to use our matrix formalism to build a universal information theory of wave imaging. From a practical point-of-view, applications to both optical microscopy, ultrasound imaging, seismology and radar technology will be aimed. This multi-disciplinary approach is actually one strength of this research project since ultrasound imaging is more flexible experimentally and can be used as a platform test for the other fields. Moreover, each domain of application investigates different kind of scattering regimes and objects to image. Each field can thus benefit from the experience acquired in other domains of wave physics, as already shown in this manuscript.

Curriculum Vitae

pdfpages

ALEXANDRE AUBRY

Date of birth: 05/20/1982 - Nationality: French

Affiliation : Institut Langevin (IL) - ESPCI Paris, PSL Research University, CNRS – 1 rue Jussieu – 75005 Paris, France

E-mail : alexandre.aubry@espci.fr - Tel : +33(0)180963066

URL: https://www.institut-langevin.espci.fr/alexandre_aubry

EDUCATION

2008	PhD in Physics *with first-class honours* – Université Pierre et Marie Curie / Paris, France - PhD Supervisor: Pr. **Arnaud DERODE**
2005	Master of Science, Major: Physics – ESPCI Paris, France Graduate Level Institute of Physics, Chemistry and Biology (www.espci.fr)
2005	Master of Science, Acoustical Physics - Université Denis Diderot / Paris, France

RESEARCH EXPERIENCE

2011 – Now	CNRS Research Scientist - Langevin Institute, CNRS (UMR7587)
2008 – 2011	Post-doc – Supervisor: Pr. Sir **John PENDRY** Blackett Laboratory, Imperial College London, United Kingdom
2005 – 2008	PhD student – Dissertation topic: Ultrasound imaging in random media. Supervisor: Pr. **Arnaud DERODE** - Waves and Acoustics Laboratory – ESPCI Paris, France

RESEARCH ACTIVITIES

Matrix approach of waves in complex media

- **Matrix approach of ultrasound imaging**

Development of a reflection matrix method for aberration correction, wave velocity tomography, scattering characterization, target-specific beamforming in the deep multiple scattering regime
Supervision of three post-docs (L. Cobus / 2016-2017, S. Vilov / 2020, J. Robin / 2021, A. Goicoechea / 2021-2022) and four PhD students (W. Lambert / 2017-2020, F. Bureau / since 2019, E. Giraudat / since 2020, A. Le Ber / since 2020)
Academic collaboration: Mathias Fink, Xiaoping Jia, Arnaud Tourin (IL), Stefan Rotter (TU Wien)
Industry Partnership: Hologic - SuperSonic Imagine (since 2017 / C. Fraschini, W. Lambert)
Funding: ERC Reminiscence (PI)

- **Matrix approach of non-destructive testing**

Development of a smart radar separating single and multiple scattering. Application to the detection of flaws in particularly heterogeneous media (coarse grain steels)
Ultrasound imaging, detection, characterization in strongly scattering media (coarse grain steels, polycrystalline media)
Academic collaboration: Arnaud Derode, Claire Prada (IL)
Co-supervision (25%) of two PhD students (C. Trottier / 2013-2016, C. Brütt / 2018-2021)
Industry Partnerships: EDF (2010-2016 / F. Rupin, A. Schumm) – SAFRAN (since 2018 / B. Gérardin)

- **Matrix approach of seismic wave imaging**

Development of a matrix approach based on diffuse wave correlations. Application to the in-depth

imaging of heterogeneous regions in the Earth's crust (volcanoes, fault zones)
Academic collaboration: Michel Campillo (ISTERRE), Arnaud Derode (IL), Arnaud Burtin (IPGP)
Supervision of three PhD students (T. Blondel / 2016-2019, R. Touma / 2018-2021, E. Giraudat / since 2020) and one post-doc (R. Touma / since 2022)
Funding: ERC F-Image (participant), ERC Reminiscence (PI)
Industry Partnership: TOTAL (2016-2019)

- Matrix approach of optical imaging

Development of a matrix approach of optical coherence tomography. In-depth imaging of biological tissues (Aberration correction, multiple scattering compensation and characterization)
Academic collaboration: Claude Boccara, Mathias Fink, Geoffroy Lerosey (IL), Serge Meimon (ONERA)
Supervision of four PhD students (Amaury Badon / 2013-2016 - Victor Barolle / 2016-2019 – Paul Balondrade / 2018-2021 – Ulysse Najar / since 2019 – Jad Aoun / since 2021 and four post-docs (Dayan Li / 2013-2015 – Victor Barolle / since 2021 – Paul Balondrade / since 2022 – Nicolas Guigui / since 2022)
Funding: ERC Reminiscence (PI), ERC Helmholtz (participant), LABEX WIFI, DGA

- Matrix approach of wave transport

Spatio-temporal imaging of wave transport in the diffusive regime (open/closed scattering channels, particle-like wave packets) and at the Anderson transition (recurrent scattering and coherent backscattering).
Academic collaboration: Stefan Rotter (TU Wien, Austria), John Page (University of Manitoba, Canada), Sergey Skipetrov, Bart van Tiggelen (LPMMC, Grenoble), Arnaud Derode, Claire Prada (IL), Georg Maret (Konstanz University)
Supervision of one PhD student (B. Gérardin / 2013-2016) and one post-doc (L. Cobus / 2017-2019)
Funding: ANR LOVE (participant), Marie Curie fellowship (Laura Cobus), LABEX, DGA

Control and focusing of waves through complex media

- Negative refraction and complementary media

Negative refraction and reflection of guided elastic waves in complex environments
Academic collaboration: Claire Prada, Jérôme Laurent (IL)
Co-supervision (50%) of two PhD students (B. Gérardin / 2013-2016 – F. Legrand / 2016-2020)
Funding: ANR COPPOLA (coordinator), LABEX, DGA

- Meta-surface and smart indoor communication

Smart algorithms for indoor imaging and communication with microwaves (WIFI, LTE)
Supervision of one PhD student (Hussam Hanouni / since 2022)
Industry Partnership: GreenerWave (Geoffroy Lerosey, Victor Barolle / since 2016)

TEACHING ACTIVITIES

Since 2011	**Tutoring** (15-30 hours/year) – Master degree – Wave Physics – ESPCI Paris, France
2012 – 2016	**Tutoring** (15 hours/year) – Master degree – Acoustical Physics – Université Denis Diderot, Paris, France

CONSULTING ACTIVITIES

Since 2016	**Consultant for a startup** *Greenerwave* which aims at developing and valorizing the research and patents developed at the Langevin institute in wireless communications.

DIRECTION OF SCIENTIFIC SOCIETIES

Since 2017 **Co-founder** and **co-director** of the **national research network "*GDR Complexe*"** on the physics of waves in complex media

ORGANISATION OF SCIENTIFIC MEETINGS

2023 Organizer of the spring school "Waves in complex media: From theory to practice" – 70 participants – Les Houches, France

2021 Organizer of the GDR Complexe Annual Workshop "Waves in complex media" – 100 participants – Paris, France

2020 Organizer of the GDR Complexe Annual Workshop "Waves in complex media" – 100 participants – *in remote*

2019 Organizer of the summer school "Imaging in Wave Physics : Multi-Wave and Large Sensor Networks 2019" – 100 participants – Cargèse, France

2019 Organizer of the GDR Complexe Annual Workshop "Waves in complex media" – 100 participants – *Paris, France*

2018 Organizer of the summer school "*Transport, Mesoscopy and Imaging of waves in complex media*" – 100 participants – Cargèse, France

2018 Committee member of the "*OSA Imaging and Applied Optics Congress*"

2017 Organizer of the ICERM Fall 2017 semester program "*Mathematical and Computational Challenges in Radar and Seismic Reconstruction*"

2017 Organizer of the summer school "*Spatio-Temporal Control of Waves: From Imaging to Sensing*" – 100 participants – Cargèse, France

2015 Organizer of the summer school "*Imaging, focusing and sensing in wave physics*" – 80 participants – Cargèse, France

2013 Organizer of the summer school "*Controlling the propagation of waves in complex media: from shaping wave fields to designing materials*" – 100 participants – Cargèse, France

EDITORIAL ACTIVITIES

Reviewer for various journals: Nature, Nature Physics, Nature Photonics, Nature Communications, Physical Review Letters, Physical Review X, Physical Review A-B-E, Optics Express, Optics Letters, Scientific Reports, JOSA, JASA, Waves in Random and Complex Media

PUBLICATIONS

- *h-index*: 29, citations 3016 (Google Scholar statistics).
- 50 publications in peer-reviewed international journals (16 as first author, 36 as corresponding author, 19 as last author). Among them: 1 in **Science**, 2 in **Science Advances**, 1 in **PNAS**, **1** in **Physical Review X**, **7** in **Physical Review Letters**, 10 in Physical Review, 2 in IEEE TMI, 2 in Sci. Rep., 2 in Nano Letters, 2 in ACS Nano, 2 in Opt. Express, 2 in Applied Physics Letters, 1 in New J. Phys., 1 in J. Appl. Phys, 1 in Ultrasound Med. Biol.
- 11 proceedings
- 2 book chapters.
- 13 patent applications, 12 issued.
- 30 invited conferences, 10 invited seminars.

International peer-reviewed publications (50)

1. W. Lambert, J. Robin, L. A. Cobus, M. Fink, and **A. Aubry**, *Ultrasound Matrix Imaging -- Part I: The focused reflection matrix , the F-factor and the role of multiple scattering*, IEEE Trans. Med. Imag., 2022
2. W. Lambert, L. A. Cobus, J. Robin, M. Fink, and **A. Aubry**, *Ultrasound matrix imaging -- Part II: The distortion matrix for aberration correction over multiple isoplanatic patches*, IEEE Trans. Med. Imag., 2022
3. C. Brütt, **A. Aubry**, B. Gérardin, A. Derode, and C. Prada, *Weight of single and recurrent scattering in the reflection matrix of complex media*, Phys. Rev. E 106, 025001, 2022
4. L. A. Cobus, G. Maret, and **A. Aubry**, *Crossover from renormalized to conventional diffusion near the 3D Anderson localization transition for light*, Phys. Rev. B 106, 014208, 2022
5. S. Gigan, O. Katz, H. B. de Aguiar, E. Andresen, **A. Aubry** et al., *Roadmap on wavefront shaping and deep imaging in complex media*, J. Phys. Photonics 4, 042501, 2022
6. U. Soysal, P. N. Azevedo, F. Bureau, **A. Aubry**, M. S. Carvalho, A. C. S. N. Pessoa, L. G. De La Torre, O. Couture, A. Tourin, M. Fink, P. Tabeling, *Freeze-dried microfluidic monodisperse microbubbles as a new generation of ultrasound contrast agents*, Ultrasound Med. Biol. 48, 1484-1495, 2022
7. R. Touma, **A. Aubry**, Y. Ben-Zion, and M. Campillo, *Distribution of seismic scatterers in the San Jacinto fault zone, southeast of Anza, california, based on passive matrix imaging*, Earth Planet. Sci. Lett. 578, 117304, 2022
8. F. Legrand, B. Gérardin, F. Bruno, J. Laurent, F. Lemoult, C. Prada, and **A. Aubry**, *Cloaking, trapping and superlensing of lamb waves with negative refraction,* Sci. Rep. 11*,* 23901, 2021
9. V. Barolle, J. Schoeller, P. Mecê, K. Groux, J.-M. Chassot, M. Fink, A. C. Boccara, and **A. Aubry**, *Manifestation of aberrations in full-field optical coherence tomography*", Opt. Express 29, 22044-22065, 2021
10. R. Touma, T. Blondel, A. Derode, M. Campillo, **A. Aubry**, *A Distortion Matrix Framework for High-Resolution Passive Seismic 3D Imaging: Application to the San Jacinto Fault Zone, California*, Geophys. J. Int. 226, 780-794, 2021
11. A. Badon, V. Barolle, K. Irsch, A.C. Boccara, M. Fink, **A. Aubry**, *Distortion matrix concept for deep imaging in scattering media*, Science Advances 6, eaay7170, 2020
12. W. Lambert, L. A. Cobus, T. Frappart, M. Fink, **A. Aubry**, *Distortion matrix approach for ultrasound imaging of random scattering media*, Proc. Natl. Acad. Sci. USA 117, 14645–14656, 2020
13. W. Lambert, L. A. Cobus, M. Couade, M. Fink, **A. Aubry**, *Reflection matrix approach for quantitative imaging of scattering media*, Phys. Rev. X 10, 021048, 2020
14. B. Gérardin, J. Laurent, F. Legrand, C. Prada, **A. Aubry**, *Negative reflection of guided elastic waves in random and chaotic media*, Sci. Rep. 9, 2135, 2019
15. F. Legrand, B. Gérardin, J. Laurent, F. Legrand, C. Prada, **A. Aubry**, *Negative reflection of Lamb modes: A theoretical study*, Phys. Rev. B **98**, 214114, 2018
16. T. Blondel, J. Chaput, A. Derode, M. Campillo, **A. Aubry**, *Matrix Approach of Seismic Imaging: Application to the Erebus Volcano, Antarctica,* J. Geophys. Res.: Solid Earth 123, 10936-10950, 2018
17. A. Badon, A. C. Boccara, G. Lerosey, M. Fink, **A. Aubry**, *Multiple scattering limit in optical microscopy*, Opt. Exp. 25, 28914-28934, 2017
18. S. Shahjahan, F. Rupin, **A. Aubry**, A. Derode, Evaluation of a multiple scattering filter to enhance defect detection in heterogeneous media, J. Acoust. Soc. Am. 141, 624-640,2017
19. A. Badon, D. Li, G. Lerosey, A. C. Boccara, M. Fink, **A. Aubry**, *Smart optical coherence tomography for ultra-deep imaging through highly scattering media*, Science Adv. 2, e1600370, 2016
20. A. Badon, D. Li, G. Lerosey, A. C. Boccara, M. Fink, **A. Aubry**, *Spatio-Temporal Imaging of Light Transport in Highly Scattering Media under White Light Illumination*, Optica 3, 1160-1166, 2016
21. B. Gérardin, J. Laurent, P. Ambichl, C. Prada, S. Rotter, **A. Aubry**, *Particle-like wave packets in complex scattering systems*, Phys. Rev. B 94, 014209, 2016

22. L. A. Cobus, S. E. Skipetrov, **A. Aubry**, B. A. van Tiggelen, A. Derode, J. H. Page, *Anderson mobility gap probed by dynamic coherent backscattering*, Phys. Rev. Lett. 116, 193901, 2016
23. B. Gérardin, J. Laurent, C. Prada, **A. Aubry**, *Negative reflection of Lamb waves at a free edge: Tunable focusing and mimicking phase conjugation*, J. Acoust. Soc. Am. 140, 591, 2016
24. A. Badon, G. Lerosey, A. C. Boccara, M. Fink, **A. Aubry**, *Retrieving time-dependent Green's functions in optics with low-coherence interferometry*, Phys. Rev. Lett. 114, 023901, 2015
25. B. Gérardin, J. Laurent, A. Derode, C. Prada, **A. Aubry**, *Full Transmission and Reflection of Waves Propagating through a Maze of Disorder*, Phys. Rev. Lett. 113, 173901, 2014
26. **A. Aubry**, L.A. Cobus, S.E. Skipetrov, B.A. van Tiggelen, A. Derode, and J.H. Page, *Recurrent Scattering and Memory Effect at the Anderson Localization Transition*, Phys. Rev. Lett. 112, 043903, 2014
27. S. Shahjahan, **A. Aubry**, F. Rupin, B. Chassignole, A. Derode, *A random matrix approach to detect defects in a strongly scattering polycrystal: How the memory effect can help overcome multiple scattering*, Appl. Phys. Lett. 104, 234105, 2014
28. S. Shahjahan, F. Rupin, **A. Aubry**, B. Chassignole, T. Fouquet, and A. Derode, *Comparison between experimental and 2-D numerical studies of multiple scattering in Inconel600 (R) by means of array probes*, Ultrasonics 54, 358-367, 2014
29. J.B. Pendry, **A. Aubry**, D.S. Smith and S.A. Maier, *Transformation optics and subwavelength control of light*, Science 337, 549-552, 2012
30. S.M. Popoff, **A. Aubry**, G. Lerosey, M. Fink, A.C. Boccara and S. Gigan, *Exploiting the time-reversal operator for adaptive optics, selective focusing, and scattering pattern analysis*, Phys. Rev. Lett. 107, 263901, 2011
31. **A. Aubry**, A. Derode, *Multiple scattering of ultrasound in weakly inhomogeneous media: Application to human soft tissues*, J. Acoust. Soc. Am. 129 , 225-233, 2011
32. **A. Aubry**, D.Y. Lei, S.A. Maier and J.B. Pendry , *Plasmonic hybridization between nanowires and a metallic surface : A transformation optics approach*, ACS Nano 5, 3293-3308, 2011
33. Y. Luo, **A. Aubry** and J.B. Pendry, *Electromagnetic contribution to surface-enhanced Raman scattering from rough metal surfaces: A transformation optics approach*, Phys. Rev. B 83, 155422, 2011
34. D. Y. Lei, **A. Aubry**, Y. Luo, S. A. Maier and J. B. Pendry, *Plasmonic interaction between overlapping nanowires*, ACS Nano 5, 597-607, 2011
35. **A. Aubry**, D.Y. Lei, S.A. Maier and J.B. Pendry, *Interaction between plasmonic nanoparticles revisited with transformation optics*, Phys. Rev. Lett. 105, 233901, 2010 - Nature Materials 10, 82, 2011, Research Highlights
36. **A. Aubry**, D.Y. Lei, A.I. Fernandez-Dominguez, Y. Sonnefraud, S.A. Maier and J.B. Pendry, *Plasmonic light harvesting devices over the whole visible spectrum*, Nano Lett. 10, 2574-2579, 2010 - Nature Materials 9, 534, 2010, Research Highlights
37. **A. Aubry**, D. Y. Lei, S. A. Maier and J. B. Pendry, *Conformal transformation applied to plasmonics beyond the quasistatic limit*, Phys. Rev. B 82, 205109, 2010
38. **A. Aubry**, D. Y. Lei, S. A. Maier and J. B. Pendry, *Broadband plasmonic device concentrating the energy at the nanoscale : The crescent-shaped cylinder*, Phys. Rev. B 82, 125430, 2010
39. **A. Aubry**, J.B. Pendry, *Mimicking a negative refractive slab by combining two phase conjugators*, J. Opt. Soc. Am. B 27, 72-84, 2010
40. Y. Luo, J. B. Pendry and **A. Aubry**, *Surface plasmons and singularities*, Nano Lett. 10, 4186-4191, 2010
41. D. Y. Lei, **A. Aubry**, S. A. Maier and J. B. Pendry, *Broadband nano-focusing of light using kissing nanowires*, New J. Phys. 12, 093030, 2010
42. **A. Aubry**, A. Derode, *Singular value distribution of the propagation matrix in random scattering media*, Waves Random Complex Media 20, 333-363, 2010
43. **A. Aubry**, A. Derode, *Detection and imaging in a random medium: A matrix method to overcome multiple scattering and aberration*, J. Appl. Phys. 106, 044903, 2009
44. **A. Aubry**, A. Derode, *Random matrix theory applied to acoustic backscattering and imaging in complex media*, Phys. Rev. Lett. 102, 084301, 2009

45. A. Aubry, A. Derode, F. Padilla, *Local measurements of the diffusion constant in multiple scattering media: Application to human trabecular bone imaging*, Appl. Phys. Lett. 92, 124101, 2008
46. C. Prada, J. De Rosny, D. Clorennec, J.G. Minonzio, A. Aubry, M. Fink *et al.*, *Experimental detection and focusing in shallow water by decomposition of the Time Reversal Operator*, J. Acoust. Soc. Am. 122, 761-768, 2007
47. A. Aubry, A. Derode., *Ultrasonic imaging of highly scattering media from local measurements of the diffusion constant : Separation of coherent and incoherent intensities*, Phys. Rev. E 75, 026602, 2007
48. A. Aubry, A. Derode, P. Roux, A. Tourin, *Coherent backscattering and far-field beamforming in acoustics*, J. Acoust. Soc. Am. 121, 70-77, 2007
49. A. Aubry, J. de Rosny, J.G. Minonzio, C. Prada, M. Fink, Gaussian beams and Legendre polyno- mials as invariants of the time reversal operator for a large rigid cylinder, J. Acoust. Soc. Am. 120, 2746-2754, 2006
50. J.G. Minonzio, C. Prada, A. Aubry, M. Fink, *Multiple scattering between two elastic cylinders and invariants of the time-reversal operator: Theory and experiment,* J. Acoust. Soc. Am. 120, 875-883, 2006

Proceedings (12)

1. Paul Balondrade; Victor Barolle; Amaury Badon; Ulysse Najar; Kristina Irsch; Mathis Fink; Claude Boccara; Alexandre Aubry, Distortion matrix concept for deep imaging in optical coherence tomography", 2021 IEEE Photonics Conference (IPC), 2021, pp. 1-2, 2021
2. A Schumm, PE Lhuillier, C Trottier, N Paul, A Aubry, A Derode "*Multiple scattering filtering for volumetric and plane defects*", AIP Conference Proceedings 2102, 040014, 2019
3. C. Trottier, S. Shahjhan, A. Schumm, A. Aubry, A. Derode, "*Multiple scattering filter: Application to plane defect detection in a nickel alloy"*, AIP Conference Proceedings 1706, 040004, 2016
4. S. Shahjahan, A. Aubry, F. Rupin, B. Chassignole, and A. Derode, "*Reduction of ultrasonic multiple scattering applied to aw detection with array probes in polycrystalline materials*", Proceedings of Meetings on Acoustics 19, 045039, 2013
5. S. Shahjahan, A. Aubry, F. Rupin, B. Chassignole, and A. Derode, "*Parametrical study of aw detection in polycrystalline materials by reducing the multiple scattering contribution*", Rev. Prog. Quant. Nondestr. Eval., AIP Conf. Proc. 1511, 675-682, 2013
6. S. Shahjahan, A. Aubry, F. Rupin, B. Chassignole, and A. Derode, "*Improvement of aw detection with ultrasonic array probes in multiple scattering polycristalline materials by means of a random matrix approach*", 13th International Symposium on Nondestructive Characterization of Materials, Le Mans, France, 2013
7. S. Shahjahan, F. Rupin, T. Fouquet, A. Aubry, and A. Derode, "*Structural noise and coherent backscattering modelled with the ATHENA 2D finite elements code*", Proceedings of the Acoustics 2012 Nantes Conference, 2012
8. S. Shahjahan, A. Aubry , F. Rupin, B. Chassignole, and A. Derode, "*Flaw detection on Inconel600 R using separation of single and multiple scattering contributions"*, Proceedings of the Acoustics 2012 Nantes Conference, 2012
9. F Rupin, B Chassignole, O Dupond, L Doudet, A Aubry, A Derode, "*Flaw Detection in Cast Stainless Steel Using Advanced Low-Frequency Ultrasonic System and Multi-Scattering Filtering*", Proceedings of the 8th International Conference on NDE in Relation to Structural Integrity for Nuclear and Pressurized Components, 772-781, 2010
10. J. -G. Minonzio, C. Prada, A. Aubry *et al.*, "*Application of the DORT method to the detection and characterization of two targets in a shallow water wave-guide*," Europe Oceans 2005, 1001-1006, 2005
11. R. H. W. Pijnenburg, R. Dekker, C. C. S. Nicole, A. Aubry and E. H. E. C. Eummelen, "Integrated micro-channel cooling in silicon," Proceedings of the 30th European Solid-State Circuits, 129-132, 2004

12. C. C. S. Nicole, R. Dekker, **A. Aubry**, and R. Pijnenburg "*Integrated Micro-Channel Cooling in Industrial Applications*", Proceedings of the ASME 2004 2nd International Conference on Microchannels and Minichannels, 673-677, 2004.

Book chapters (2)

1- A. Badon, **A. Aubry** and M. Fink, Reflection matrix approaches in scattering media: From detection to imaging, Chapter in Wavefront Shaping for Biomedical Imaging, edited by J. Kubby, M. Cui and S. Gigan, Cambridge University Press, UK, 2019

2- **A. Aubry** and J.B. Pendry, *Transformation Optics for Plasmonics*, Chapter in Active Plasmonics and Tuneable Metamaterials, edited by A. Zayats and S.A. Maier, John Wiley & Sons, Inc., Hoboken, NJ, USA, 2013

Patents (13)

1- **A. Aubry**, P. Balondrade, V. Barolle, U. Najar, C. Boccara, M. Fink, " *Procédés et système de caractérisation optique d'un milieu volumique et diffusant* ", FR Patent n°2207334, 2022 (filed)

2- W. Lambert, **A. Aubry**, M.Fink, T. Frappart, "*Method and system for ultrasonic characterization of a medium*", US Patent n° US20220082693, 2022

3- W. Lambert, **A. Aubry**, M.Fink, T. Frappart, " *Method and system for ultrasonic characterization of a medium* ", US Patent n° US20220084496, 2022

4- W. Lambert, **A. Aubry**, M. Fink, T. Frappart, F. Bureau, *Method and system for ultrasonic characterization of a medium* ", US Patent n° US20220082527, 2022

5- W. Lambert, **A. Aubry**, M.Fink, T. Frappart, " *Method and system for ultrasonic characterization of a medium* ", US Patent n° US20220082529, 2022

6- W. Lambert, **A. Aubry**, M.Fink, T. Frappart, " *Method and system for ultrasonic characterization of a medium* ", WO Patent n° WO2022058675, 2022

7- W. Lambert, **A. Aubry**, L.A. Cobus, M.Fink, "*Methods and systems for non-invasively characterizing a heterogeneous medium using ultrasound*", WO Patent n° WO2021023933, 2021

8- **A. Aubry**, M. Fink, A. C. Boccara, A. Badon, V. Barolle, L.A. Cobus, W. Lambert, "*Methods and systems for non-invasively characterizing a heterogeneous medium using ultrasound*", US Patent n° US20220003721, 2022

9- **A. Aubry**, M. Fink, A. C. Boccara, A. Badon, V. Barolle, L.C. Cobus, W. Lambert, "*Methods and systems for the non-invasive optical characterization of a heterogeneous medium*", US Patent n° US20210310787, 2021

10- G. Lerosey, P. del Hougne, M. Fink, **A. Aubry**, *"Method for determining a characteristic of a receiver in a medium and system implementing this method*", US Patent n° US20210167873, 2021

11- G. Lerosey, M. Fink, F. Lemoult, **A. Aubry**, T. Floume, "*Communication network access point, communication network, and method of wireless communication*", US Patent n° US20200153578, 2020

12- C. Trottier, A. Derode, **A. Aubry**, "*Sounding method and device using wave propagation*" US Patent n° 10267914, 2019

13- A. Derode, **A. Aubry**, M. Fink "*Sounding method and device using wave propagation*" US Patent n° 10267914, 2014

Invited conferences (30)

1- A. Aubry, *Ultrasound Matrix Imaging*, Gordon Conference sur Tissue Microstructure Imaging– Easton, MA, USA, 2023 (initially foreseen in 2021 but deferred to 2023 because of pandemia)
2- A. Aubry, *Matrix approach to wave imaging in complex media*, International Workshop "Waves in Complex Media: From spatial to temporal degrees of freedom", Cargèse, France, 2022
3- A. Aubry, *Matrix approach of optical coherence tomography for deep imaging in biological tissues* – SFO Congress School – Nice, France, 2022
4- A. Aubry, *Matrix approach of wave imaging: From the human body to passive seismology* – Spring School – Passive imaging and monitoring in wave physics: From seismology to ultrasound VI – Cargèse, France, 2022
5- A. Aubry, *Distortion matrix concept for deep imaging in optical coherence tomography* – IEEE Photonics Conference – virtual meeting, 2021
6- A. Aubry, *Matrix approach of adaptive optics* – Adaptive Optics European Summer School, Virtual Meeting, 2021
7- A. Aubry, *Matrix approach for deep optical imaging in scattering media* – IEEE Photonics Conference, Vancouver, Canada, 2021 (remote)
8- A. Aubry, *Distortion matrix approach for deep optical imaging in scattering media* – OSA, Imaging and Applied Optics Congress, Vancouver, Canada, 2020 (remote)
9- A. Aubry, *Reflection matrix approach for quantitative ultrasound imaging of scattering media* – International Workshop Wave Propagation and Information Transport in Disordered Heterogeneous Media, Boulder, USA, 2020
10- A. Aubry, *Reflection matrix approach for quantitative ultrasound imaging of scattering media* – Forum Acusticum, Lyon, France, 2020
11- A. Aubry, *Matrix approach to wave imaging in complex media*, International Workshop "Imaging in wave physics", Cargèse, France, 2019
12- A. Aubry, *Matrix approach of optical coherence tomography* – Workshop on Adaptive Optics, Ophtalmoscopy and OCT 2019, Paris, France, 2019
13- A. Aubry, *Matrix approach of optical imaging through highly scattering media* – Physics of quantum electronics, Summer School MOT – Micro and Optical Technologies in Biomedical Science, Fiesch, Switzerland, 2018
14- A. Aubry, *Matrix approach of optical imaging through highly scattering media* – OptoDiag, Paris, France, 2018
15- A. Aubry, *Matrix approach of optical imaging through highly scattering media* – Physics of quantum electronics, Snowbird, Utah, USA, 2018
16- A. Aubry, *Matrix approach of optical imaging through highly scattering media* – Assemblée générale GDR ondes, 2017
17- A. Badon, D. Li, G. Lerosey, A. C. Boccara, M. Fink, and A. Aubry, *Smart optical coherence tomography for ultra-deep imaging through highly scattering media* - Advances in Optics for Biotechnology, Medicine and Surgery XV, Snowmass village, USA, 2017
18- A. Badon, D. Li, G. Lerosey, A. C. Boccara, M. Fink, and A. Aubry - *Smart optical coherence tomography for ultra-deep imaging through highly scattering media* - OSA, Imaging and Applied Optics Congress, San Francisco, 2017
19- A. Aubry, *Retrieving time-dependent Green's functions in optics with low-coherence interferometry, Workshop Imagerie et détection à partir du bruit ambiant ou du champ diffus*, Paris, France, 2016
20- B. Gérardin, J. Laurent, A. Derode, C. Prada, A. Aubry, *Full transmission and reflection of waves through a maze of disorder*, Acoustical Society of America, Salt Lake City, USA, 2016

21- A. Aubry, *Spatio-temporal imaging of light transport*, Workshop "Strongly disordered optical systems: From the white paint to cold atoms", Cargèse, France, 2016
22- B. Gérardin, P. Ambichl, J. Laurent, A. Derode, C. Prada, S. Rotter, A. Aubry, *Particle-like wave packets in complex scattering systems* - URSI International Symposium on Electromagnetic Theory (EMTS), Espoo, Finlande, 2016
23- A. Badon, G. Lerosey, A. C. Boccara, M. Fink, and A. Aubry, *Spatio-temporal imaging of light transport in strongly scattering media* - URSI International Symposium on Electromagnetic Theory (EMTS), Espoo, Finlande, 2016
24- A. Badon, D. Li, G. Lerosey, A. C. Boccara, M. Fink, and A. Aubry, *Overcoming multiple scattering for detection and imaging in strongly scattering media*, BiOS/Photonics West, San Francisco, USA, 2016
25- A. Aubry, *A random matrix approach of optical imaging through highly scattering media* – GDR Mesoimage, Paris, France, 2015
26- A. Aubry, *Full transmission, reflection and trapping of waves through a maze of disorder*, ETOPIM 10, Jerusalem, Israël, 2015
27- A. Aubry, Recurrent scattering and memory effect at the Anderson transition, Workshop Waves in complex media, Grenoble, France, 2013
28- A. Aubry, Separation of single, recurrent and multiple scattering in complex media : Applications to ultrasound imaging and characterization, Workshop Ambient noise Imaging and Monitoring, Cargèse, France, 2013
29- A. Aubry, Separation of single, recurrent and multiple scattering in complex media, Workshop LANL-IPGP-Langevin 2012, Paris, France, 2012
30- A. Aubry, Separation of single, recurrent and multiple scattering in complex media : Applications to ultrasound imaging and characterization, Workshop Waves and Imaging in complex media, Heraklion, Greece, 2012

Invited seminars (11)

1- A. Aubry, Reflection Matrix Imaging in Wave Physics, Institut de Mécanique et d'Ingénierie, Bordeaux, France, 2022
2- A. Aubry, Reflection Matrix Imaging in Wave Physics, IDEFIX Research Team (INRIA, Institut Polytechnique de Paris, EDF R&D), Saclay, France, 2022
3- A. Aubry, Matrix approach to wave Imaging, Delft University (Physics Department), The Netherlands, 2021
4- A. Aubry, Matrix approach to wave Imaging, LIFI Laboratory, Grenoble, France, 2021
5- A. Aubry, Matrix approach of seismic imaging, Seminar IPGP, Paris, France, 2019
6- A. Aubry, Matrix Imaging, Journée Regards Croisés ONERA/ Institut Langevin, Paris France, 2019
7- A. Aubry, Matrix approach of optical imaging, Seminar Institut Fresnel, Marseille, France, 2018
8- A. Aubry, Controlling the propagation of elastic waves with wave-front shaping and negative refraction, Seminar Imperial College, Londres, Royaume-Uni, 2015
9- A. Aubry, Separation of single, recurrent and multiple scattering in complex media, Seminar IPGP, Paris, France, 2011
10- A. Aubry, Separation of single, recurrent and multiple scattering in complex media, Seminar Institut Fresnel, Marseille, France, 2011
11- A. Aubry, Random matrix theory applied to acoustics backscattering, Imperial College London 2008

SUPERVISION OF STUDENTS AND POST-DOCS

For the last ten years, I have supervised or co-supervised 9 post-docs, 17 PhD students, 11 Master students and 9 under-graduate students. In the following, I indicate for each of them the starting and end dates of their stay in my group, the part of the work under my direct supervision and the topic of their work.

9 Post-doctoral fellows (100% under my supervision)

Name	Date	Length	Topic
Nicolas GUIGUI	since 2022	On-going	Information theory of wave imaging
Rita TOUMA	since 2022	On-going	Passive Seismic Matrix Imaging
Paul BALONDRADE	since 2022	On-going	Matriscope: 3D optical utra-fast imaging
Victor BAROLLE	since 2021	On-going	Matriscope: 3D quantitative imaging
Antton GOICOECHEA	since 2021	On-going	Random matrix theory of wave imaging
Justine ROBIN	since 2021	9 months	4D Matrix Imaging
Sergey VILOV	2020	1 year	Quantitative ultrasound imaging
Laura COBUS	2016-2019	3 years	Matrix approach of ultrasound imaging
Dayan LI	2013-2015	2 years	Matrix approach of optical microscopy

16 PhD students:

Name	Date	supervision	Topic	Phd director(s)
Hussam HANOUNI	since 2022	50	Imaging radar based on leaky reconfigurable cavities	Alexandre Aubry
Jad AOUN	since 2021	100	Matrix approach of adaptive optics	Mathias Fink
Elsa GIRAUDAT	since 2020	100	Multiple scattering in ultrasound and seismic imaging	Mathias Fink
Arthur LE BER	since 2020	100	Deep ultrasound imaging in granular media	Arnaud Tourin
Flavien BUREAU	since 2019	100	3D ultrasound matrix imaging	Mathias Fink
Ulysse NAJAR	since 2019	100	Matrix approach of full-field optical coherence tomography	Mathias Fink / Claude Boccara
Cécile BRUTT	2018-2021	30	Contrôle non destructif matriciciel	Claire Prada/Arnaud Derode
Rita TOUMA	2018-2021	50	Passive seismic matrix imaging	Michel Campillo
Paul BALONDRADE	2018-2021	100	Distortion matrix approach of optical microscopy	Mathias Fink
William LAMBERT	2017-2020	100	Matrix approach for ultrasound imaging and quantification	Mathias Fink
François LEGRAND	2016-2020	50	Ondes de Lamb et réfraction négative	Claire Prada
Victor BAROLLE	2016-2019	100	Approche matricielle de la tomographie à cohérence optique	Mathias Fink / Claude Boccara
Thibaud BLONDEL	2016-2019	100	Matrix approach of seismic imaging	Arnaud Derode / Michel Campillo
Amaury BADON	2013-2016	100	Approche matricielle de l'imagerie optique des milieux diffusants	Mathias Fink/ Claude Boccara
Benoît GERARDIN	2013-2016	80	Manipulation d'ondes élastiques guidées en milieux complexes	Arnaud Derode / Claire Prada
Camille TROTTIER	2013-2016	30	Détection de défauts en milieu fortement diffusant	Arnaud Derode

11 Master students (100% under my supervision)

Name	Year	Topic	Master
Jad AOUN	2021	Imagerie matricielle en optique	Laser, optique, matière (Paris Saclay)
Elsa GIRAUDAT	2020	Imagerie sismique du volcan la Souffrière en Guadeloupe	Energie renouvelable (Polytechnique)
Arthur LE BER	2020	Approche matricielle de la correction d'aberration en échographie	Acoustique Physique (Université de Paris)
Marie PALLA	2020	Contrôle des ondes élastiques dans les granulaires	Acoustique Physique (Université de Paris)
Ulysse NAJAR	2019	Approche matricielle de l'imagerie optique des milieux diffusants	Optique (Sorbonne Université)
Paul BALONDRADE	2018	Mesure optique de la matrice distorsion	Nanosciences (Paris Saclay)
William LAMBERT	2017	Approche matricielle de la correction d'aberration en échographie	Acoustique Physique (Université de Paris)
François LEGRAND	2016	Ondes de Lamb et refraction négative	Acoustique Physique (Sorbonne Université)
Thibaud BLONDEL	2014	Retournement temporal itératif appliqué à l'imagerie sismique	ITI (PSL)
Amaury BADON	2013	Extraction des fonctions de Green par corrélation de bruit en optique	CFP, Physique de la Matière Condensée (ENS)
Benoît GERARDIN	2013	Canaux de propagation ouverts et fermés en régime diffusant	Acoustique Physique (Université de Paris)

9 undergraduate trainees (100% under my supervision)

Name	Date	Length (month)	Topic	School
Tanguy BERTELS	2022	3	Subsurface microwave matrix imaging	ESPCI
Nathan ROUGIER	2021	6	Spectral domain OCT	Centrale Paris
Brieuc BEAUSEIGNEUR	2020	3	Adaptive optics	ESPCI
Wei GUO	2015	3	Cloaking of Lamb waves	ESPCI
Samuel METAIS	2014	3	Perfect corner	ESPCI
Samret DI MANNO	2014	3	Sub-wavelength control of waves	ESPCI
Yanis BAHROUN	2012	3	Random matrix theory applied to wave transport	Université de Paris
David METIVIER	2012	3	Matrix approach of wave transport	ENS Lyon
Célia AMABILE	2012	3	Open/closed scattering channels	ESPCI

Bibliography

[1] M. Fink et al., "Time-reversed acoustics", Rep. Prog. Phys. **63**, 1933–1995 (2000).

[2] A. P. Mosk, A. Lagendijk, G. Lerosey, and M. Fink, "Controlling waves in space and time for imaging and focusing in complex media", Nat. Photonics **6**, 283–292 (2012).

[3] C. W. J. Beenakker, "Random-matrix theory of quantum transport", Rev. Mod. Phys. **69**, 731–808 (1997).

[4] S. Rotter and S. Gigan, "Light fields in complex media: mesoscopic scattering meets wave control", Rev. Mod. Phys. **89**, 015005 (2017).

[5] B. Gérardin, J. Laurent, A. Derode, C. Prada, and A. Aubry, "Full transmission and reflection of waves propagating through a maze of disorder", Phys. Rev. Lett. **113**, 173901 (2014).

[6] S. Rotter, P. Ambichl, and F. Libisch, "Generating particlelike scattering states in wave transport", Phys. Rev. Lett. **106**, 120602 (2011).

[7] B. Gérardin, J. Laurent, P. Ambichl, C. Prada, S. Rotter, and A. Aubry, "Particlelike wave packets in complex scattering systems", Phys. Rev. B **94**, 014209 (2016).

[8] M. Tanter, J.-F. Aubry, J. Gerber, J.-L. Thomas, and M. Fink, "Optimal focusing by spatio-temporal inverse filter. i. basic principles", J. Acoust. Soc. Am. **110**, 37–47 (2001).

[9] A. Derode, A. Tourin, J. de Rosny, M. Tanter, S. Yon, and M. Fink, "Taking advantage of multiple scattering to communicate with time-reversal antennas", Phys. Rev. Lett. **90**, 014301 (2003).

[10] S. M. Popoff, G. Lerosey, R. Carminati, M. Fink, A. C. Boccara, and S. Gigan, "Measuring the transmission matrix in optics: an approach to the study and control of light propagation in disordered media", Phys. Rev. Lett. **104**, 100601 (2010).

[11] M. Kim et al., "Maximal energy transport through disordered media with the implementation of transmission eigenchannels", Nat. Photonics **6**, 581–585 (2012).

[12] I. N. Papadopoulos, S. Farahi, C. Moser, and D. Psaltis, "Focusing and scanning light through a multimode optical fiber using digital phase conjugation", Opt. Express **20**, 10583 (2012).

[13] T. Čižmár and K. Dholakia, "Exploiting multimode waveguides for pure fibre-based imaging", Nat. Commun. **3**, 1027 (2012).

[14] M. W. Matthès, Y. Bromberg, J. de Rosny, and S. M. Popoff, "Learning and avoiding disorder in multimode fibers", Phys. Rev. X **11**, 021060 (2021).

[15] C. Prada and M. Fink, "Eigenmodes of the time reversal operator: a solution to selective focusing in multiple-target media", Wave Motion **20**, 151–163 (1994).

[16] V. Lauer, "New approach to optical diffraction tomography yielding a vector equation of diffraction tomography and a novel tomographic microscope", J. Microsc. **205**, 165–176 (2002).

[17] J.-L. Robert and M. Fink, "Green's function estimation in speckle using the decomposition of the time reversal operator: application to aberration correction in medical imaging", J. Acoust. Soc. Am. **123**, 866–877 (2008).

[18] A. Aubry and A. Derode, "Random Matrix Theory Applied to Acoustic Backscattering and Imaging In Complex Media", Phys. Rev. Lett. **102**, 084301 (2009).

[19] S. M. Popoff, A. Aubry, G. Lerosey, M. Fink, A. C. Boccara, and S. Gigan, "Exploiting the time-reversal operator for adaptive optics, selective focusing, and scattering pattern analysis", Phys. Rev. Lett. **107**, 263901 (2011).

[20] T. Zhang, P. C. Chaumet, E. Mudry, A. Sentenac, and K. Belkebir, "Electromagnetic wave imaging of targets buried in a cluttered medium using a hybrid inversion-DORT method", Inverse Problems **28**, 125008 (2012).

[21] S. Kang et al., "Imaging deep within a scattering medium using collective accumulation of single-scattered waves", Nat. Photonics **9**, 253–258 (2015).

[22] S. Kang et al., "High-resolution adaptive optical imaging within thick scattering media using closed-loop accumulation of single scattering", Nat. Commun. **8**, 2157 (2017).

[23] S. Yoon, H. Lee, J. H. Hong, Y.-S. Lim, and W. Choi, "Laser scanning reflection-matrix microscopy for aberration-free imaging through intact mouse skull", Nat. Commun. **11**, 5721 (2020).

[24] A. Aubry and A. Derode, "Detection and imaging in a random medium : a matrix method to overcome multiple scattering and aberration", J. Appl. Phys. **106**, 044903 (2009).

[25] S. Shahjahan, A. Aubry, F. Rupin, B. Chassignole, and A. Derode, "A random matrix approach to detect defects in a strongly scattering polycrystal: how the memory effect can help overcome multiple scattering", Appl. Phys. Lett. **104**, 234105 (2014).

[26] A. Aubry and A. Derode, "Singular value distribution of the propagation matrix in random scattering media", Waves Random Complex Media **20**, 333–363 (2010).

[27] A. Badon, D. Li, G. Lerosey, A. C. Boccara, M. Fink, and A. Aubry, "Smart optical coherence tomography for ultra-deep imaging through highly scattering media", Sci. Adv. **2**, e1600370 (2016).

[28] T. Blondel, J. Chaput, A. Derode, M. Campillo, and A. Aubry, "Matrix approach of seismic imaging: application to the Erebus volcano, Antarctica", J. Geophys. Res.: Solid Earth **123**, 10, 936–10, 950 (2018).

[29] A. Badon, A. C. Boccara, G. Lerosey, M. Fink, and A. Aubry, "Multiple scattering limit in optical microscopy", Opt. Express **25**, 28914 (2017).

[30] A. Aubry and A. Derode, "Ultrasonic imaging of highly scattering media from local measurements of the diffusion constant: separation of coherent and incoherent intensities", Phys. Rev. E **75**, 026602 (2007).

[31] W. Lambert, L. A. Cobus, M. Couade, M. Fink, and A. Aubry, "Reflection matrix approach for quantitative imaging of scattering media", Phys. Rev. X **10**, 021048 (2020).

[32] W. Lambert, L. C. Cobus, M. Fink, and A. Aubry, "Ultrasound matrix imaging – part I: The focused reflection matrix, the F-factor and the role of multiple scattering", IEEE Trans. Med. Imag., 10.1109/TMI.2022.3199498 (2022).

[33] A. Badon, V. Barolle, K. Irsch, A. C. Boccara, M. Fink, and A. Aubry, "Distortion matrix concept for deep imaging in optical coherence microscopy", Sci. Adv. **6**, eaay7170 (2020).

[34] W. Lambert, L. A. Cobus, T. Frappart, M. Fink, and A. Aubry, "Distortion matrix approach for ultrasound imaging of random scattering media", Proc. Natl. Acad. Sci. U. S. A. **117**, 14645–14656 (2020).

[35] W. Lambert, L. C. Cobus, T. Frappart, M. Fink, and A. Aubry, "Ultrasound matrix imaging – part II: the distortion matrix for a local correction of aberrations", IEEE Trans. Med. Imag., 10.1109/TMI.2022.3199483 (2022).

[36] A. Derode, P. Roux, and M. Fink, "Robust acoustic time reversal with high-order multiple scattering", Phys. Rev. Lett. **75**, 4206–4209 (1995).

[37] P. Roux and M. Fink, "Time-reversal in a waveguide", J. Acoust. Soc. Am. **110**, 2631–2631 (2001).

[38] R. Touma, R. Blondel, A. Derode, M. Campillo, and A. Aubry, "A distortion matrix framework for high-resolution passive seismic 3d imaging: Application to the San Jacinto fault zone, California", Geophys. J. Int. **226**, 780–794 (2021).

[39] E. Giraudat, A. Burtin, and A. Aubry, "Passive seismic matrix imaging of La Soufrière of guadeloupe volcano", EGU General Assembly 2021, 10.5194/egusphere-egu21-4516 (2021).

[40] A. Badon, D. Li, G. Lerosey, A. C. Boccara, M. Fink, and A. Aubry, "Spatio-temporal imaging of light transport in highly scattering media under white light illumination", Optica **3**, 1160–1166 (2016).

[41] M. P. V. Albada and A. Lagendijk, "Observation of weak localization of light in a random medium", Phys. Rev. Lett. **55**, 2692–2695 (1985).

[42]P.-E. Wolf and G. Maret, "Weak localization and coherent backscattering of photons in disordered media", Phys. Rev. Lett. **55**, 2696–2699 (1985).

[43]A. Tourin, A. Derode, P. Roux, B. A. van Tiggelen, and M. Fink, "Time-dependent coherent backscattering of acoustic waves", Phys. Rev. Lett. **79**, 3637–3639 (1997).

[44]P. Anderson, "Absence of diffusion in certain random lattices", Phys. Rev. **109**, 1492–1505 (1958).

[45]E. Abrahams, P. W. Anderson, D. C. Licciardello, and T. V. Ramakrishnan, "Scaling theory of localization: absence of quantum diffusion in two dimensions", Phys. Rev. Lett. **42**, 673–676 (1979).

[46]H. Hu, A. Strybulevych, J. H. Page, S. E. Skipetrov, and B. A. van Tiggelen, "Localization of ultrasound in a three-dimensional elastic network", Nat. Phys. **4**, 945 (2008).

[47]A. Aubry, L. Cobus, S. Skipetrov, B. van Tiggelen, A. Derode, and J. Page, "Recurrent scattering and memory effect at the anderson localization transition", Phys. Rev. Lett. **112**, 043903 (2014).

[48]L. Cobus, S. Skipetrov, A. Aubry, B. van Tiggelen, A. Derode, and J. Page, "Anderson mobility gap probed by dynamic coherent backscattering", Phys. Rev. Lett. **116**, 193901 (2016).

[49]L. A. Cobus, G. Maret, and A. Aubry, "Crossover from renormalized to conventional diffusion near the 3d anderson localization transition for light", Phys. Rev. B **106**, 014208 (2022).

[50]C. Brütt, A. Aubry, B. Gérardin, A. Derode, and C. Prada, "Weight of single and recurrent scattering in the reflection matrix of complex media", to be pulished in Phys. Rev. E (2022).

[51]J. B. Pendry, "Negative refraction makes a perfect lens", Phys. Rev. Lett. **85**, 3966–3969 (2000).

[52]J. Pendry, "Negative refraction", Contemp. Phys. **45**, 191–202 (2004).

[53]U. Leonhardt, "Optical conformal mapping", Science **312**, 1777–1780 (2006).

[54]D. Royer and E. Dieulesaint, *Elastic waves in solids—free and guided waves* (Springer, Berlin, 2000).

[55]I. Tolstoy and E. Usdin, "Wave propagation in elastic plates: low and high mode dispersion", J. Acoust. Soc. Am. **29**, 37–42 (1957).

[56]C. Prada, O. Balogun, and T. W. Murray, "Laser-based ultrasonic generation and detection of zero-group velocity lamb waves in thin plates", Appl. Phys. Lett. **87**, 194109 (2005).

[57]S. Bramhavar, C. Prada, A. A. Maznev, A. G. Every, T. B. Norris, and T. W. Murray, "Negative refraction and focusing of elastic lamb waves at an interface", Phys. Rev. B **83**, 014106 (2011).

[58]F. D. Philippe, T. W. Murray, and C. Prada, "Focusing on plates: controlling guided waves using negative refraction", Sci. Rep. **5**, 11112 (2015).

[59]F. Legrand, B. Gérardin, J. Laurent, C. Prada, and A. Aubry, "Negative refraction of lamb modes: a theoretical study", Phys. Rev. B **98**, 214114 (2018).

[60]M. Germano, A. Alippi, A. Bettucci, and G. Mancuso, "Anomalous and negative reflection of lamb waves in mode conversion", Phys. Rev. B **85**, 012102 (2012).

[61]I. A. Veres, C. Grünsteidl, D. M. Stobbe, and T. W. Murray, "Broad-angle negative reflection and focusing of elastic waves from a plate edge", Phys. Rev. B **93**, 174304 (2016).

[62]B. Gérardin, J. Laurent, C. Prada, and A. Aubry, "Negative reflection of lamb waves at a free edge: tunable focusing and mimicking phase conjugation", J. Acoust. Soc. Am. **140**, 591–600 (2016).

[63]B. Gérardin, J. Laurent, F. Legrand, C. Prada, and A. Aubry, "Negative reflection of elastic guided waves in chaotic and random scattering media", Sci. Rep. **9**, 2135 (2019).

[64]F. Legrand et al., "Cloaking, trapping and superlensing of lamb waves with negative refraction", Sci. Rep. **11**, 23901 (2021).

[65]F. Roddier, *Adaptive optics in astronomy* (Cambridge University Press, Cambridge, 1999, 1999).

[66]T. L. Szabo, *Diagnostic ultrasound imaging: inside out* (Academic Press, Elsevier, Amsterdam, 2014).

[67]M. J. Booth, "Adaptive optics in microscopy", Philos. Trans. R. Soc. A **365**, 2829–2843 (2007).

[68]M. Hirama, O. Ikeda, and T. Sato, "Adaptive ultrasonic array imaging system through an inhomogeneous layer", J. Acoust. Soc. Am. **71**, 100–109 (1982).

[69]M. O'Donnell and S. Flax, "Phase-aberration correction using signals from point reflectors and diffuse scatterers: measurements", IEEE Trans. Ultrason., Ferroelectr. Freq. Control **35**, 768–774 (1988).

[70]L. Nock, G. E. Trahey, and S. W. Smith, "Phase aberration correction in medical ultrasound using speckle brightness as a quality factor", J. Acoust. Soc. Am. **85**, 1819–1833 (1989).

[71]R. Mallart and M. Fink, "Adaptive focusing in scattering media through sound-speed inhomogeneities: The van Cittert Zernike approach and focusing criterion.", J. Acoust. Soc. Am. **96**, 3721–3732 (1994).

[72]O. Ikeda, "An image reconstruction algorithm using phase conjugation for diffraction-limited imaging in an inhomogeneous medium", J. Acoust. Soc. Am. **85**, 1602–1606 (1989).

[73]C. Dorme and M. Fink, "Focusing in transmit–receive mode through inhomogeneous media: the time reversal matched filter approach", J. Acoust. Soc. Am. **98**, 1155–1162 (1995).

[74]M. Minsky, "Confocal scanning microscope", U.S. pat. US3013467 (1955).

[75]M. G. L. Gustafsson, "Surpassing the lateral resolution limit by a factor of two using structured illumination microscopy", J. Microsc. **198**, 82–87 (2000).

[76]W. Denk, J. H. Strickler, and W. W. Webb, "Two-photon laser scanning fluorescence microscopy", Science **248**, 73–76 (1990).

[77]D. Huang et al., "Optical coherence tomography", Science **254**, 1178–1181 (1991).

[78]J. M. Girkin, S. Poland, and A. J. Wright, "Adaptive optics for deeper imaging of biological samples", Curr. Opin. Biotechnol. **20**, 106–110 (2009).

[79]J. A. Kubby, *Adaptive optics for biological imaging* (CRC Press, Boca Raton, FL, 2013).

[80]M. J. Booth, "Adaptive optical microscopy: the ongoing quest for a perfect image", Light Sci. Appl. **3**, e165–e165 (2014).

[81]O. Yilmaz, *Seismic data analysis. processing, inversion, and interpretation of seismic data* (Society of Exploration Geophysicists, Tulsa, OK, USA, 2008).

[82]L. Hatton, K. Larner, and B. Gibson, "Migration of seismic data from inhomogeneous media", Geophysics **46**, 751–767 (1981).

[83]A. Labeyrie, "Attainment of diffraction limited resolution in large telescopes by fourier analysing speckle patterns in star images", Astron. Astrophys. **6**, 85–87 (1970).

[84]B. Hermann et al., "Adaptive-optics ultrahigh-resolution optical coherence tomography", Opt. Lett. **29**, 2142 (2004).

[85]M. Rueckel, J. A. Mack-Bucher, and W. Denk, "Adaptive wavefront correction in two-photon microscopy using coherence-gated wavefront sensing", Proc. Natl. Acad. Sci. U. S. A. **103**, 17137–17142 (2006).

[86]D. Débarre, E. J. Botcherby, T. Watanabe, S. Srinivas, M. J. Booth, and T. Wilson, "Image-based adaptive optics for two-photon microscopy", Opt. Lett. **34**, 2495 (2009).

[87]N. Ji, D. E. Milkie, and E. Betzig, "Adaptive optics via pupil segmentation for high-resolution imaging in biological tissues", Nat. Methods **7**, 141–147 (2009).

[88]J. Tang, R. N. Germain, and M. Cui, "Superpenetration optical microscopy by iterative multiphoton adaptive compensation technique", Proc. Natl. Acad. Sci. U. S. A. **109**, 8434–8439 (2012).

[89]J. Jang et al., "Complex wavefront shaping for optimal depth-selective focusing in optical coherence tomography", Opt. Express **21**, 2890 (2013).

[90]J.-H. Park, W. Sun, and M. Cui, "High-resolution in vivo imaging of mouse brain through the intact skull", Proc. Natl. Acad. Sci. U. S. A. **112**, 9236–9241 (2015).

[91]J. Bertolotti, E. G. van Putten, C. Blum, A. Lagendijk, W. L. Vos, and A. P. Mosk, "Non-invasive imaging through opaque scattering layers", Nature **491**, 232–234 (2012).

[92]O. Katz, E. Small, and Y. Silberberg, "Looking around corners and through thin turbid layers in real time with scattered incoherent light", Nat. Photonics **6**, 549–553 (2012).

[93]O. Katz, P. Heidmann, M. Fink, and S. Gigan, "Non-invasive single-shot imaging through scattering layers and around corners via speckle correlations", Nat. Photonics **8**, 784–790 (2014).

[94]I. Freund, M. Rosenbluh, and S. Feng, "Memory effects in propagation of optical waves through disordered media", Phys. Rev. Lett. **61**, 2328–2331 (1988).

[95]S. Feng, C. Kane, P. A. Lee, and A. D. Stone, "Correlations and fluctuations of coherent wave transmission through disordered media", Phys. Rev. Lett. **61**, 834–837 (1988).

[96]G. Osnabrugge, R. Horstmeyer, I. N. Papadopoulos, B. Judkewitz, and I. M. Vellekoop, "Generalized optical memory effect", Optica **4**, 886 (2017).

[97]B. Judkewitz, R. Horstmeyer, I. M. Vellekoop, I. N. Papadopoulos, and C. Yang, "Translation correlations in anisotropically scattering media", Nat. Phys. **11**, 684–689 (2015).

[98]J. J. Dahl, M. S. Soo, and G. E. Trahey, "Spatial and temporal aberrator stability for real-time adaptive imaging.", IEEE Trans. Ultrason. Ferroelectr. Freq. Control **52**, 1504–1517 (2005).

[99]S. Popoff, G. Lerosey, M. Fink, A. C. Boccara, and S. Gigan, "Image transmission through an opaque material", Nat. Commun. **1**, 81 (2010).

[100]C. Prada, S. Manneville, D. Spoliansky, and M. Fink, "Decomposition of the time reversal operator: detection and selective focusing on two scatterers", J. Acoust. Soc. Am. **99**, 2067–2076 (1996).

[101]H. Tortel, G. Micolau, and M. Saillard, "Decomposition of the time reversal operator for electromagnetic scattering", J. Electromagn. Waves Appl. **13**, 687–719 (1999).

[102]A. Aubry and A. Derode, "Multiple scattering of ultrasound in weakly inhomogeneous media: application to human soft tissues", J. Acoust. Soc. Am. **129**, 225–233 (2011).

[103]T. Zhang et al., "Multi-wavelength multi-angle reflection tomography", Opt. Express **26**, 26093 (2018).

[104]Y. Choi et al., "Measurement of the time-resolved reflection matrix for enhancing light energy delivery into a scattering medium", Phys. Rev. Lett. **111**, 243901 (2013).

[105]H. Bendjador, T. Deffieux, and M. Tanter, "The SVD beamformer: physical principles and application to ultrafast adaptive ultrasound", IEEE Trans. Med. Imag. **39**, 3100–3112 (2020).

[106]L. M. Hinkelman, T. L. Szabo, and R. C. Waag, "Measurements of ultrasonic pulse distortion produced by human chest wall", J. Acoust. Soc. Am. **101**, 2365–2373 (1997).

[107]F. A. Duck, *Physical properties of tissues* (Elsevier, Amsterdam, 1990), pp. 73–135.

[108]L. M. Hinkelman, T. D. Mast, L. A. Metlay, and R. C. Waag, "The effect of abdominal wall morphology on ultrasonic pulse distortion. part i. measurements", J. Acoust. Soc. Am. **104**, 3635–3649 (1998).

[109]C. Holmes, B. W. Drinkwater, and P. D. Wilcox, "Post-processing of the full matrix of ultrasonic transmit–receive array data for non-destructive evaluation", NDT &amp E International **38**, 701–711 (2005).

[110]G. Montaldo, M. Tanter, J. Bercoff, N. Benech, and M. Fink, "Coherent plane-wave compounding for very high frame rate ultrasonography and transient elastography", IEEE Trans. Ultrason. Ferroelectr. Freq. Control **56**, 489–506 (2009).

[111]C. Passmann and H. Ermert, "A 100-MHz ultrasound imaging system for dermatologic and ophthalmologic diagnostics", IEEE Trans. Ultrason. Ferroelectr. Freq. Control **43**, 545–552 (1996).

[112]M.-H. Bae and M.-K. Jeong, "A study of synthetic-aperture imaging with virtual source elements in b-mode ultrasound imaging systems", IEEE Trans. Ultrason. Ferroelectr. Freq. Control **47**, 1510–1519 (2000).

[113]G. Montaldo, M. Tanter, and M. Fink, "Time reversal of speckle noise", Phys. Rev. Lett. **106**, 054301 (2011).

[114]M. A. Lediju, G. E. Trahey, B. C. Byram, and J. J. Dahl, "Short-lag spatial coherence of backscattered echoes: imaging characteristics", IEEE Trans. Ultrason. Ferroelectr. Freq. Control **58**, 1377–1388 (2011).

[115]J. J. Dahl et al., "Coherence beamforming and its applications to the difficult-to-image patient", 2017 ieee international ultrasonics symposium (ius) (IEEE, 2017), pp. 1–10.

[116]G. Chau, M. Jakovljevic, R. Lavarello, and J. Dahl, "A locally adaptive phase aberration correction (lapac) method for synthetic aperture sequences", Ultrason. Imaging **41**, 3–16 (2019).

[117]M. Jaeger, E. Robinson, H. Günhan Akarçay, and M. Frenz, "Full correction for spatially distributed speed-of-sound in echo ultrasound based on measuring aberration delays via transmit beam steering", Phys. Med. Biol. **60**, 4497–4515 (2015).

[118]Z. Kam, P. Kner, D. Agard, and J. W. Sedat, "Modelling the application of adaptive optics to wide-field microscope live imaging", J. Microscopy **226**, 33–42 (2007).

[119]R. D. Simmonds and M. J. Booth, "Modelling of multi-conjugate adaptive optics for spatially variant aberrations in microscopy", J. Opt. **15**, 094010 (2013).

[120]O. J. O'Connor and M. M. Maher, "Imaging of cholecystitis", American Journal of Roentgenology **196**, W367–W374 (2011).

[121]R. H. Stolt, "Migration by Fourier transform", Geophysics **43**, 23–48 (1978).

[122]J. Gazdag, "Wave equation migration with the phase-shift method", Geophysics **43**, 1342–1351 (1978).

[123]J. Gazdag and P. Sguazzero, "Migration of seismic data by phase shift plus interpolation", Geophysics **49**, 124–131 (1984).

[124]J. F. Claerbout, *Imaging of of the Earth's interior*, 2d (Blackwell Scientific Publications, 1996).

[125]B. Biondi, *3d seismic imaging* (Society of Exploration Geophysicists, 2006).

[126]R. L. Weaver and O. I. Lobkis, "Ultrasonics without a source: Thermal fluctuation correlations at MHz frequencies", Phys. Rev. Lett. **87**, 134301 (2001).

[127]M. Campillo and A. Paul, "Long-range correlations in the diffuse seismic coda", Science **299**, 547–549 (2003).

[128]A. Derode et al., "Recovering the Green's function from field-field correlations in an open scattering medium", J. Acoust. Soc. Am. **113**, 2973 (2003).

[129]K. Wapenaar, "Retrieving the elastodynamic Green's function of an arbitrary inhomogeneous medium by cross correlation", Phys. Rev. Lett. **93**, 254301 (2004).

[130]R. Snieder, "Extracting the Green's function from the correlation of coda waves: A derivation based on stationary phase", Phys. Rev. E **69**, 046610 (2004).

[131]E. Larose et al., "Correlation of random wavefields: An interdisciplinary review", Geophysics **71**, SI11 (2006).

[132]N. M. Shapiro, M. Campillo, L. Stehly, and M. H. Ritzwoller, "High-resolution surface-wave tomography from ambient seismic noise", Science, 1615–1618 (2005).

[133]K. G. Sabra, P. Gerstoft, P. Roux, W. Kuperman, and M. C. Fehler, "Extracting time-domain green's function estimates from ambient seismic noise", Geophys. Res. Lett. **32**, L03310 (2005).

[134]Y. Yang, M. H. Ritzwoller, A. L. Levshin, and N. M. Shapiro, "Ambient noise Rayleigh wave tomography across Europe", Geophys. J. Int. **168**, 259–274 (2007).

[135]P. Roux, K. G. Sabra, P. Gerstoft, W. Kuperman, and M. C. Fehler, "P-waves from cross-correlation of seismic noise", Geophys. Res. Lett. **32**, L19303 (2005).

[136]D. Draganov, K. Wapenaar, W. Mulder, J. Singer, and A. Verdel, "Retrieval of reflections from seismic background-noise measurements", Geophys. Res. Lett. **34**, L04305 (2007).

[137]D. Draganov, X. Campman, J. Thorbecke, A. Verdel, and K. Wapenaar, "Reflection images from ambient seismic noise", Geophysics **74**, A63–A67 (2009).

[138]P. Poli, H. Pedersen, and M. Campillo, "Emergence of body waves from cross-correlation of short period seismic noise", Geophys. J. Int. **188**, 549–558 (2012).

[139]Y. Ben-Zion et al., "Basic data features and results from a spatially dense seismic array on the San Jacinto fault zone", Geophys. J. Int. **202**, 370–380 (2015).

[140]E. Hauksson, W. Yang, and P. Shearer, "Waveform relocated earthquakecatalog for southern California (1981 to june 2011)", Bull. Seism. Soc. Am. **105**, 2239–2244 (2012).

[141]H. O. Johnson, D. C. Agnew, and F. K. Wyatt, "Present-day crustal deformation in southern California", J. Geophys. Res.: Solid Earth **99**, 23951–23974 (1994).

[142]E. O. Lindsey and Y. Fialko, "Geodetic slip rates in the southern San Andreas Fault system: Effects of elastic heterogeneity and fault geometry", J. Geophys. Res.: Solid Earth **118**, 689–697 (2013).

[143]A. A. Allam and Y. Ben-Zion, "Seismic velocity structures in the southern California plate-boundary environment from double-difference tomography", Geophys. J. Int. **190**, 1181–1196 (2012).

[144]D. Zigone, Y. Ben-Zion, M. Campillo, and P. Roux, "Seismic tomography of the Southern California plate boundary region from noise-based Rayleigh and Love waves", Pure Appl. Geophys. **172**, 1007–1032 (2014).

[145]P. Roux et al., "A methodological approach towards high-resolution surface wave imaging of the San Jacinto Fault Zone using ambient-noise recordings at a spatially dense array", Geophys. J. Int. **206**, 980–992 (2016).

[146]P.-E. Share et al., "Characterizing the uppermost 100 m structure of the San Jacinto fault zone southeast of Anza, California, through joint analysis of geological, topographic, seismic and resistivity data", Geophys. J. Int. **222**, 781–794 (2020).

[147]Y.-G. Li and P. C. Leary, "Fault zone trapped seismic waves", Bull. Seism. Soc. Am. **80**, 1245–1271 (1990).

[148]Y. Ben-Zion and C. G. Sammis, "Characterization of fault zones", Pure Appl. Geophys. **160**, 677–715 (2003).

[149]R. Touma, A. Aubry, Y. Ben-Zion, and M. Campillo, "Distribution of seismic scatterers in the san jacinto fault zone, southeast of anza, california, based on passive matrix imaging", Earth Planet. Sci. Lett. **578**, 117304 (2022).

[150]R. Moretti et al., "The 2018 unrest phase at la soufrière of guadeloupe (french west indies) andesitic volcano: scrutiny of a failed but prodromal phreatic eruption", J. Volcanol. Geotherm. Res. **393**, 106769 (2020).

[151]R. Touma, "Approche matricielle de l'imagerie sismique passive par ondes de volume", PhD thesis (Université Grenoble Alpes, 2022).

[152]T. Durduran, R. Choe, W. B. Baker, and A. G. Yodh, "Diffuse optics for tissue monitoring and tomography", Rep. Prog. Phys. **73**, 076701 (2010).

[153]S. G. Resink, A. C. Boccara, and W. Steenbergen, "State-of-the art of acousto-optic sensing and imaging of turbid media", J. Biomed. Opt. **17**, 040901 (2012).

[154]M. Xu and L. V. Wang, "Photoacoustic imaging in biomedicine", Rev. Sci. Instrum. **77**, 041101 (2006).

[155]J. B. Pawley, ed., *Handbook of biological confocal microscopy* (Springer-Verlag, New York, 2006).

[156]V. Ntziachristos, "Going deeper than microscopy: the optical imaging frontier in biology", Nat. Methods **7**, 603–614 (2010).

[157]P. Theer, M. T. Hasan, and W. Denk, "Two-photon imaging to a depth of 1000 μm in living brains by use of a ti:al2o3 regenerative amplifier", Opt. Lett. **28**, 1022–1024 (2003).

[158]J. G. Fujimoto, S. De Silvestri, E. P. Ippen, C. A. Puliafito, R. Margolis, and A. Oseroff, "Femtosecond optical ranging in biological systems", Opt. Lett. **11**, 150–152 (1986).

[159]J. G. Fujimoto et al., "Optical biopsy and imaging using optical coherence tomography", Nature Med. **1**, 970–972 (1995).

[160]A. F. Fercher, "Optical coherence tomography.", J. Biomed. Opt. **1**, 157–173 (1996).

[161]W. Drexler and J. G. Fujimoto, eds., *Optical coherence tomography. technology and applications.* (Springer-Verlag, New York, 2008).

[162]H. W. Babcock, "The possibility of compensating astronomical seeing", Publ. Astron. Soc. Pac. **65**, 229–236 (1953).

[163]R. Foy and A. Labeyrie, "Feasibility of adaptive telescope with laser probe", Astron. Astrophys. **152**, L29–L31 (1985).

[164]S. T. Thurman and J. R. Fienup, "Correction of anisoplanatic phase errors in digital holography", J. Opt. Soc. Am. A **25**, 995–999 (2008).

[165]A. E. Tippie and J. R. Fienup, "Multiple-plane anisoplanatic phase correction in a laboratory digital holography experiment", Opt. Lett. **35**, 3291–3293 (2010).

[166]M. J. Booth, M. A. Neil, R. Juškaitis, and T. Wilson, "Adaptive aberration correction in a confocal microscope", Proc. Natl. Acad. Sci. U. S. A. **99**, 5788–5792 (2002).

[167]X. Tao et al., "Adaptive optics confocal microscopy using direct wavefront sensing", Opt. Lett. **36**, 1062–1064 (2011).

[168]I. N. Papadopoulos, J.-S. Jouhanneau, J. F. Poulet, and B. Judkewitz, "Scattering compensation by focus scanning holographic aberration probing (f-sharp)", Nat. Photonics **11**, 116–123 (2017).

[169]S. G. Adie, B. W. Graf, A. Ahmad, P. S. Carney, and S. A. Boppart, "Computational adaptive optics for broadband optical interferometric tomography of biological tissue", Proc. Natl. Acad. Sci. U. S. A. **109**, 7175–7180 (2012).

[170]S. Jeong et al., "Focusing of light energy inside a scattering medium by controlling the time-gated multiple light scattering", Nat. Photonics **12**, 277–283 (2018).

[171]A. A. Badon, "Approche matricielle de l'imagerie optique des milieux diffusants", PhD thesis (Sorbonne Paris Cité, 2016).

[172]V. Barolle, "Approche matricielle de la tomographie à cohérence optique", PhD thesis (Université Paris Sciences et Lettres, 2019).

[173]A. Badon, G. Lerosey, A. C. Boccara, M. Fink, and A. Aubry, "Retrieving time-dependent green's functions in optics with low-coherence interferometry", Phys. Rev. Lett. **114**, 023901 (2015).

[174]E. Beaurepaire, A. C. Boccara, M. Lebec, L. Blanchot, and H. Saint-Jalmes, "Full-field optical coherence microscopy", Opt. Lett. **23**, 244–246 (1998).

[175]A. Dubois, K. Grieve, G. Moneron, R. Lecaque, L. Vabre, and C. Boccara, "Ultrahigh-resolution full-field optical coherence tomography", Appl. Opt. **43**, 2874–2883 (2004).

[176]V. Barolle et al., "Manifestation of aberrations in full-field optical coherence tomography", Opt. Express **29**, 22044 (2021).

[177]P. Balondrade, "Approche matricielle de la microscopie optique: quantification et correction des aberrations", PhD thesis (Université Paris Sciences et Lettres, 2021).

[178]B. Považay, A. Unterhuber, B. Hermann, H. Sattmann, H. Arthaber, and W. Drexler, "Full-field time-encoded frequency-domain optical coherence tomography", Opt. Express **14**, 7661–7669 (2006).

[179]R. Leitgeb, C. Hitzenberger, and A. Fercher, "Performance of Fourier domain vs time domain optical coherence tomography", Opt. Express **11**, 889–894 (2003).

[180]J. F. de Boer, B. Cense, B. H. Park, M. C. Pierce, G. J. Tearney, and B. E. Bouma, "Improved signal-to-noise ratio in spectral-domain compared with time-domain optical coherence tomography", Opt. Lett. **28**, 2067–2069 (2003).

[181]M. Choma, M. Sarunic, C. Yang, and J. Izatt, "Sensitivity advantage of swept source and fourier domain optical coherence tomography", Opt. Express **11**, 2183–2189 (2003).

[182]D. Hillmann et al., "Aberration-free volumetric high-speed imaging of in vivo retina", Sci. Rep. **6**, 35209 (2016).

[183]D. Hillmann, H. Spahr, C. Pfäffle, H. Sudkamp, G. Franke, and G. Hüttmann, "In vivo optical imaging of physiological responses to photostimulation in human photoreceptors", Proc. Natl. Acad. Sci. U. S. A. **113**, 13138–13143 (2016).

[184]A. A. Grebenyuk, L. Ginner, and R. A. Leitgeb, "Numerically focused full-field swept-source optical coherence microscopy with structured illumination", Opt. Express **26**, 33772–33782 (2018).

[185]E. Auksorius et al., "In vivo imaging of the human cornea with high-speed and high-resolution fourier-domain full-field optical coherence tomography", Biomed. Opt. Exp. **11**, 2849–2865 (2020).

[186]M. Jang, H. Ruan, I. M. Vellekoop, B. Judkewitz, E. Chung, and C. Yang, "Relation between speckle decorrelation and optical phase conjugation (OPC)-based turbidity suppression through dynamic scattering media: a study on in vivo mouse skin", Biomed. Opt. Express **6**, 72 (2014).

[187]B.-F. Osmanski, G. Montaldo, M. Tanter, and M. Fink, "Aberration correction by time reversal of moving speckle noise", IEEE Trans. Ultrason. Ferroelectr. Freq. Control **59**, 1575–1583 (2012).

[188]C. Apelian, F. Harms, O. Thouvenin, and A. C. Boccara, "Dynamic full field optical coherence tomography: subcellular metabolic contrast revealed in tissues by interferometric signals temporal analysis", Biomed. Opt. Express **7**, 1511–1524 (2016).

[189]H. Nimiya, T. Ikeda, and T. Tsuji, "Spatial and temporal seismic velocity changes on kyushu island during the 2016 kumamoto earthquake", Sci. Adv. **3**, e170081 (2017).

[190]T. Hirose, H. Nakahara, T. Nishimura, and M. Campillo, "Locating spatial changes of seismic scattering property by sparse modeling of seismic ambient noise cross-correlation functions: application to the 2008 iwate-miyagi nairiku (im/i iw/i 6.9), japan, earthquake", J. Geophys. Res. Solid Earth **125**, e2019JB019307 (2020).

[191]C. van der Veen, *Fundamentals of glacier dynamics* (CRC Press, Mar. 2013).

[192]P. Ambichl, A. Brandstötter, J. Böhm, M. Kühmayer, U. Kuhl, and S. Rotter, "Focusing inside disordered media with the generalized wigner-smith operator", Phys. Rev. Lett. **119**, 033903 (2017).

[193]T. A. Whittingham, "Tissue harmonic imaging", Eur. Radiol. **9**, S323–S326 (1999).

[194]A. Boniface, J. Dong, and S. Gigan, "Non-invasive focusing and imaging in scattering media with a fluorescence-based transmission matrix", Nat. Commun. **11**, 6154 (2020).

[195]J. Idier, S. Labouesse, M. Allain, P. Liu, S. Bourguignon, and A. Sentenac, "On the superresolution capacity of imagers using unknown speckle illuminations", IEEE Transactions on Computational Imaging **4**, 87–98 (2018).

[196]G. Micolau, M. Saillard, and P. Borderies, "DORT method as applied to ultrawideband signals for detection of buried objects", IEEE Trans. Geosci. Remote Sens. **41**, 1813–1820 (2003).

[197]D. Psaltis and A. S. Goy, "Digital confocal microscope", Opt. Express **20**, 22720–22727 (2012).

[198]J. Chaput et al., "Multiple scattering from icequakes at Erebus volcano, Antarctica: Implications for imaging at glaciated volcanoes", J. Geophys. Res. **120**, 1129–1141 (2015).

[199]H. Knox, "Eruptive characteristics and glacial earthquake investigation on Erebus volcano, Antarctica", PhD thesis (Mexico Institute of Mining and Technology, 2012).

[200]D. Zandomeneghi, A. Aster, P. Kyle, A. H. Barclay, J. Chaput, and H. Knox, "Internal structure of erebus volcano, antarctica imaged by high-resolution active-cource seismic tomography and coda interferometry", J. Geophys. Res. Solid Earth **118**, 1067–1078 (2013).

[201]D. J. Verschuur, A. J. Berkhout, and C. P. A. Wapenaar, "Adaptive surface-related multiple elimination", Geophysics **57**, 1166–1177 (1992).

[202] A. Aubry, J. de Rosny, J.-G. Minonzio, C. Prada, and M. Fink, "Gaussian beams and legendre polynomials as invariants of the time reversal operator for a large rigid cylinder", J. Acoust. Soc. Am. **120**, 2746–2754 (2006).

[203] J.-L. Robert and M. Fink, "The prolate spheroidal wave functions as invariants of the time reversal operator for an extended scatterer in the Fraunhofer approximation", J. Acoust. Soc. Am. **125**, 218–226 (2009).

[204] S. van den Wildenberg, X. Jia, J. Léopoldès, and A. Tourin, "Ultrasonic tracking of a sinking ball in a vibrated dense granular suspension", Sci. Rep. **9**, 5460 (2019).

[205] J. H. Page, P. Sheng, H. P. Schriemer, I. Jones, J. Xiaodun, and D. A. Weitz, "Group Velocity in Strongly Scattering Media", Science **271**, 634–637 (1996).

[206] D. Royer, E. Dieulesaint, X. Jia, and Y. Shui, "Optical generation and detection of surface acoustic waves on a sphere", Appl. Phys. Lett. **52**, 706–708 (1988).

[207] D. Clorennec and D. Royer, "Investigation of surface acoustic wave propagation on a sphere using laser ultrasonics", Appl. Phys. Lett. **85**, 2435–2437 (2004).

[208] J.-L. Thomas, P. Roux, and M. Fink, "Inverse scattering analysis with an acoustic time-reversal mirror", Phys. Rev. Lett. **72**, 637–640 (1994).

[209] C. Prada and M. Fink, "Separation of interfering acoustic scattered signals using the invariants of the time-reversal operator. application to lamb waves characterization", J. Acoust. Soc. Am. **104**, 801–807 (1998).

[210] H. Ammari, T. Boulier, J. Garnier, W. Jing, H. Kang, and H. Wang, "Target identification using dictionary matching of generalized polarization tensors", Foundations of Computational Mathematics **14**, 27–62 (2013).

[211] H. Ammari, T. Boulier, J. Garnier, H. Kang, and H. Wang, "Tracking of a mobile target using generalized polarization tensors", SIAM Journal on Imaging Sciences **6**, 1477–1498 (2013).

[212] H. Ammari, M. P. Tran, and H. Wang, "Shape identification and classification in echolocation", SIAM Journal on Imaging Sciences **7**, 1883–1905 (2014).

[213] S. Gigan et al., "Roadmap on wavefront shaping and deep imaging in complex media", J. Phys. Photonics, 10.1088/2515-7647/ac76f9 (2022).

[214] A. Thendiyammal, G. Osnabrugge, T. Knop, and I. M. Vellekoop, "Model-based wavefront shaping microscopy", Opt. Lett. **45**, 5101 (2020).

[215] L. Zhu, J. B. de Monvel, P. Berto, S. Brasselet, S. Gigan, and M. Guillon, "Chromato-axial memory effect through a forward-scattering slab", Optica **7**, 338 (2020).

[216] Y. Park, C. Depeursinge, and G. Popescu, "Quantitative phase imaging in biomedicine", Nat. Photonics **12**, 578–589 (2018).

[217] A. C. Kak and M. Slaney, *Principles of computerized tomographic imaging* (Society for Industrial and Applied-Mathematics, Philadelphia, PA, 2001).

[218] M. Imbault et al., "Robust sound speed estimation for ultrasound-based hepatic steatosis assessment", Phys. Med. Biol. **62**, 3582–3598 (2017).

[219] P. Stähli, M. Kuriakose, M. Frenz, and M. Jaeger, "Improved forward model for quantitative pulse-echo speed-of-sound imaging", Ultrasonics **108**, 106168 (2020).

[220] A. Puszka et al., "Spatial resolution in depth for time-resolved diffuse optical tomography using short source-detector separations", Biomed. Opt. Express **6**, 1–10 (2015).

[221] L. Azizi, K. Zarychta, D. Ettori, E. Tinet, and J.-M. Tualle, "Ultimate spatial resolution with diffuse optical tomography", Opt. Express **17**, 12132–12144 (2009).

[222] A. B. Konovalov and V. V. Vlasov, "Theoretical limit of spatial resolution in diffuse optical tomography using a perturbation model", Quantum Electron. **44**, 239 (2014).

[223] K. Suzuki et al., "Dependence of ultrasonic attenuation of liver on pathologic fat and fibrosis: examination with experimental fatty liver and liver fibrosis models", Ultrasound Med. Biol. **18**, 657–666 (1992).

[224] M. Sasso et al., "Controlled attenuation parameter (CAP): a novel VCTE^{TM} guided ultrasonic attenuation measurement for the evaluation of hepatic steatosis: preliminary study and validation in a cohort of patients with chronic liver disease from various causes", Ultrasound Med. Biol. **36**, 1825–1835 (2010).

[225] J. C. Bamber and C. R. Hill, "Acoustic properties of normal and cancerous human liver- I. Dependence on pathological condition", Ultrasound Med. Biol. **7**, 121–133 (1981).

[226] J. C. Bamber, C. R. Hill, and J. A. King, "Acoustic properties of normal and cancerous human liver-II. Dependence on tissue structure", Ultrasound Med. Biol. **7**, 135–144 (1981).

[227]C. F. Chen, D. E. Robinson, L. S. Wilson, K. A. Griffiths, A. Manoharan, and B. D. Doust, "Clinical sound speed measurement in liver and spleen in vivo", Ultrason. Imaging **9**, 221–235 (1987).

[228]J. Y. Schurr D. P. Kim, K. G. Sabra, and L. J. Jacobs, "Damage detection in concrete using coda wave interferometry", NDT&E Int. **44**, 728–735 (2011).

[229]S. Shajahan, F. Rupin, A. Aubry, B. Chassignole, T. Fouquet, and A. Derode, "Comparison between experimental and 2-d numerical studies of multiple scattering in inconel600â® by means of array probes", Ultrasonics **54**, 358–367 (2014).

[230]Y. Zhang, T. Planes, E. Larose, and A. Obermann, "Diffuse ultrasound monitoring of stress and damage development on a 15-ton concrete beam", J. Acoust. Soc. Am. **139**, 1691–1709 (2016).

[231]H. Sato, M. C. Fehler, and T. Maeda, *Seismic wave propagation and scattering in the heterogeneous earth : second edition* (Springer-Verlag, Berlin, 2012).

[232]J. Mayor, P. Traversa, M. Calvet, and L. Margerin, "Tomography of crustal seismic attenuation in metropolitan france: implications for seismicity analysis", Bull. Earthquake Eng. **16**, 2195–2210 (2018).

[233]A. Aubry, "Approche matricielle de l'opérateur de propagation des ondes ultrasonores en milieu diffusant aléatoire", PhD thesis (Université Pierre et Marie Curie, Paris, 2008).

[234]A. Aubry, A. Derode, and F. Padilla, "Local measurements of the diffusion constant in multiple scattering media: application to human trabecular bone imaging", Appl. Phys. Lett. **92**, 124101 (2008).

[235]K. Mohanty, J. Blackwell, T. Egan, and M. Muller, "Characterization of the lung parenchyma using ultrasound multiple scattering", Ultrasound Med. Biol. **43**, 993–1003 (2017).

[236]W. Lambert, "Matrix approach for ultrasound imaging and quantification", PhD thesis (PSL Research University, 2020).

[237]W. Lambert, A. Aubry, T. Frappart, F. Bureau, and M. Fink, "Method and system for ultrasonic characterization of a medium", US17/473,025 (2022).

[238]L. Sandrin, S. Catheline, M. Tanter, X. Hennequin, and M. Fink, "Time-resolved pulsed elastography with ultrafast ultrasonic imaging", Ultrasonic Imaging **21**, 259–272 (1999).

[239]L. Sandrin, M. Tanter, S. Catheline, and M. Fink, "Shear modulus imaging with 2-d transient elastography", IEEE Trans. Ultrason., Ferroelectr. Freq. Control **49**, 426–435 (2002).

[240]A.-M. Almeida, "Fatty liver disease in severe obese patients: diagnostic value of abdominal ultrasound", World J. Gastroentero. **14**, 1415 (2008).

[241]J. E. Browne, A. J. Watson, P. R. Hoskins, and A. T. Elliott, "Investigation of the effect of subcutaneous fat on image quality performance of 2d conventional imaging and tissue harmonic imaging", Ultrasound Med. Biol. **31**, 957–964 (2005).

[242]M. Lediju, M. Pihl, S. Hsu, J. Dahl, C. Gallippi, and G. Trahey, "A motion-based approach to abdominal clutter reduction", IEEE Trans. Ultrason. Ferroelectr. Freq. Control **56**, 2437–2449 (2009).

[243]R. Ali et al., "Local sound speed estimation for pulse-echo ultrasound in layered media", IEEE Trans. Ultrason. Ferroelectr. Freq. Control **69**, 500–511 (2022).

[244]A. Scorza, S. Conforto, C. D'Anna, and S. Sciuto, "A comparative study on the influence of probe placement on quality assurance measurements in b-mode ultrasound by means of ultrasound phantoms", Open Biomed. Eng. J. **9**, 164–178 (2015).

[245]K. H. Nicolaides, M. L. Brizot, and R. J. M. Snijders, "Fetal nuchal translucency: ultrasound screening for fetal trisomy in the first trimester of pregnancy", BJOG: An International Journal of Obstetrics and Gynaecology **101**, 782–786 (1994).

[246]R. Snijders, P. Noble, N. Sebire, A. Souka, and K. Nicolaides, "UK multicentre project on assessment of risk of trisomy 21 by maternal age and fetal nuchal-translucency thickness at 10–14 weeks of gestation", The Lancet **352**, 343–346 (1998).

[247]S. W. Flax, N. J. Pelc, G. H. Glover, F. D. Gutmann, and M. McLachlan, "Spectral characterization and attenuation measurements in ultrasound", Ultrason. Imaging **5**, 95–116 (1983).

[248]Y. Labyed and T. A. Bigelow, "A theoretical comparison of attenuation measurement techniques from backscattered ultrasound echoes", J. Acoust. Soc. Am. **129**, 2316–2324 (2011).

[249]A. Baelde et al., "Effect of microstructural elongation on backscattered field: Intensity measurement and multiple scattering estimation with a linear transducer array", Ultrasonics **82**, 379–389 (2018).

[250] A. Velichko, "Quantification of the Effect of Multiple Scattering on Array Imaging Performance", IEEE Trans. Ultrason. Ferroelectr. Freq. Control **67**, 92–105 (2020).

[251] J. H. Page, H. P. Schriemer, A. E. Bailey, and D. A. Weitz, "Experimental test of the diffusion approximation for multiply scattered sound", Phys. Rev. E **52**, 3106 (1995).

[252] M. S. Patterson, B. Chance, and B. C. Wilson, "Time resolved reflectance and transmittance for the noninvasive measurement of tissue optical properties", Appl. Opt. **28**, 2331–2336 (1989).

[253] R. Vreeker, M. P. van Albada, R. Sprik, and A. Lagendijk, "Femtosecond time-resolved measurements of weak localization of light", Phys. Lett. A **132**, 51–54 (1988).

[254] F. Jendrzejewski et al., "Three-dimensional localization of ultracold atoms in an optical disordered potential", Nat. Phys. **8**, 398–403 (2012).

[255] C. Hainaut et al., "Return to the origin as a probe of atomic phase coherence", Phys. Rev. Lett. **118**, 1–6 (2017).

[256] L. Margerin, M. Campillo, and B. A. van Tiggelen, "Coherent backscattering of acoustic waves in the near field", Geophys. J. Int. **145**, 593–603 (2001).

[257] E. Larose, L. Margerin, B. A. van Tiggelen, and M. Campillo, "Weak localization of seismic waves", Phys. Rev. Lett. **93**, 048501 (2004).

[258] M. P. van Albada, B. A. van Tiggelen, A. Lagendijk, and A. Tip, "Speed of propagation of classical waves in strongly scattering media", Phys. Rev. Lett. **66**, 3132 (1991).

[259] P. C. Waterman, "T-matrix methods in acoustic scattering", J. Acoust. Soc. Am. **125**, 42–51 (2009).

[260] D. Vollhardt and P. Wölfle, "Scaling equations from a self-consistent theory of anderson localization", Phys. Rev. Lett. **48**, 699–702 (1982).

[261] S. E. Skipetrov and B. A. van Tiggelen, "Dynamics of anderson localization in open 3d media", Phys. Rev. Lett. **96**, 043902 (2006).

[262] A. Lagendijk, B. A. van Tiggelen, and D. S. Wiersma, "Fifty years of anderson localization", Phys. Today **62**, 24–29 (2009).

[263] J. B. Pendry, "Light finds a way through the maze", Physics **1**, 20 (2008).

[264] O. N. Dorokhov, "On the coexistence of localized and extended electronic states in the metallic phase", Sol. St. Comm. **51**, 381 (1984).

[265] Y. Imry, "Active transmission channels and universal conductance fluctuations", Europhys. Lett. **1**, 249 (1986).

[266] J. B. Pendry, A. MacKinnon, and A. B. Pretre, "Maximal fluctuations- a new phenomenon in disordered systems", Physica A **168**, 400–407 (1990).

[267] R. Sprik, A. Tourin, J. de Rosny, and M. Fink, "Eigenvalue distributions of correlated multichannel transfer matrices in strongly scattering systems", Phys. Rev. B **78**, 012202 (2008).

[268] Z. Shi and A. Genack, "Transmission eigenvalues and the bare conductance in the crossover to anderson localization", Phys. Rev. Lett. **108**, 043901 (2012).

[269] M. Davy, Z. Shi, J. Wang, and A. Z. Genack, "Transmission statistics and focusing in single disordered samples", Opt. Express **21**, 10367 (2013).

[270] R. Sarma, A. G. Yamilov, S. Petrenko, Y. Bromberg, and H. Cao, "Control of energy density inside a disordered medium by coupling to open or closed channels", Phys. Rev. Lett. **117**, 086803 (2016).

[271] S. Feng and P. A. Lee, "Mesoscopic conductors and correlations in laser speckle patterns", Science **251**, 633–639 (1991).

[272] W. Choi, A. P. Mosk, Q.-H. Park, and W. Choi, "Transmission eigenchannels in a disordered medium", Phys. Rev. B **83**, 134207 (2011).

[273] Y. D. Chong and A. D. Stone, "Hidden black: coherent enhancement of absorption in strongly scattering media", Phys. Rev. Lett. **107**, 163901 (2011).

[274] C. W. J. Beenaker and M. Büttiker, "Suppression of shot noise in metallic diffusive conductors", Phys. Rev. B **46**, 1889 (1992).

[275] M. Henny, S. Oberholzer, C. Strunk, and C. Shchönenberger, "1/3-shot-noise suppression in diffusive nanowires", Phys. Rev. B **59**, 2871 (1999).

[276] I. M. Vellekoop and A. P. Mosk, "Universal optimal transmission of light through disordered materials", Phys. Rev. Lett. **101**, 120601 (2008).

[277]A. Goestchy and A. D. Stone, "Filtering random matrices: the effect of incomplete channel control in multiple scattering", Phys. Rev. Lett. **111**, 063901 (2013).

[278]S. M. Popoff, A. Goetschy, S. F. Liew, A. D. Stone, and H. Cao, "Coherent control of total transmission of light through disordered media", Phys. Rev. Lett. **112**, 133903 (2014).

[279]B. Gérardin, "Manipulation et contrôle d'ondes élastiques guidées en milieux complexes", PhD thesis (Sorbonne Paris Cité, 2016).

[280]E. P. Wigner, "Lower limit for the energy derivative of the scattering phase shift", Phys. Rev. **98**, 145–147 (1955).

[281]F. T. Smith, "Lifetime matrix in collision theory", Phys. Rev. **118**, 349–356 (1960).

[282]S. John, "Electromagnetic Absorption in a Disordered Medium near a Photon Mobility Edge", Phys. Rev. Lett. **53**, 2169 (1984).

[283]S. John, "Localization of Light", Phys. Today **44**, 32 (1991).

[284]F. Evers and A. D. Mirlin, "Anderson transitions", Rev. Mod. Phys. **80**, 1355–1417 (2008).

[285]D. S. Wiersma, P. Bartolini, A. Lagendijk, and R. Righini, "Localization of light in a disordered medium", Nature **390**, 671–673 (1997).

[286]M. Störzer, P. Gross, C. M. Aegerter, and G. Maret, "Observation of the critical regime near anderson localization of light", Phys. Rev. Lett. **96**, 063904 (2006).

[287]K. M. Douglass, S. John, T. Suezaki, G. A. Ozin, and A. Dogariu, "Anomalous flow of light near a photonic crystal pseudo-gap", Opt. Express **19**, 25320–25327 (2011).

[288]T. Sperling, W. P. Bührer, C. M. Aegerter, and G. Maret, "Direct determination of the transiton to localization of light in three dimensions", Nat. Photonics **7**, 48 (2013).

[289]F. Scheffold, R. Lenke, R. Tweer, and G. Maret, "Localization or classical diffusion of light?", Nature **398**, 206–207 (1999).

[290]T. van der Beek, P. Barthelemy, P. M. Johnson, D. S. Wiersma, and A. Lagendijk, "Light transport through disordered layers of dense gallium arsenide submicron particles", Phys. Rev. B. **85**, 1–11 (2012).

[291]T. Sperling, L. Schertel, M. Ackermann, G. J. Aubry, C. M. Aegerter, and G. Maret, "Can 3D light localization be reached in 'white paint'?", New J. Phys. **18**, 13039 (2016).

[292]J. Chabé, G. Lemarié, B. Gréemaud, D. Delande, P. Szriftgiser, and J. Garreau, "Experimental experimental observation of the Anderson metal–insulator transition with atomic matter waves", Phys. Rev. Lett. **101**, 255702 (2008).

[293]S. S. Kondov, W. R. McGehee, J. J. Zirbel, and B. DeMarco, "Three-dimensional Anderson localization of ultracold matter", Science **334**, 66–68 (2011).

[294]Y. Kuga and A. Ishimaru, "Retroreflectance from a dense distribution of spherical particles", J. Opt. Soc. Am. A **1**, 831 (1984).

[295]I. Freund, M. Rosenbluh, and R. Berkovits, "Geometric scaling of the optical memory effect in coherent-wave propagation through random media", Phys. Rev. B **39**, 12403–12406 (1989).

[296]E. Akkermans and G. Montambaux, *Mesoscopic physics of electrons and photons* (Cambridge University Press, London, 2006).

[297]B. A. van Tiggelen, D. A. Wiersma, and A. Lagendijk, "Self-consistent theory for the enhancement factor in coherent backscattering", Europhys. Lett. **30**, 1–6 (1995).

[298]S. E. Skipetrov and A. Sinha, "Time-dependent reflection at the localization transition", Phys. Rev. B **97**, 104202 (2018).

[299]W. K. Hildebrand et al., "Observation of infinite-range intensity correlations above, at, and below the mobility edges of the 3D Anderson localization transition", Phys. Rev. Lett. **112**, 1–8 (2014).

[300]S. E. Skipetrov and J. H. Page, "Red light for Anderson localization", New J. Phys. **18**, 21001 (2016).

[301]F. Cottier, A. Cipris, R. Bachelard, and R. Kaiser, "Microscopic and macroscopic signatures of 3D Anderson localization of light", Phys. Rev. Lett. **123**, 83401 (2019).

[302]S. E. Skipetrov and I. M. Sokolov, "Absence of anderson localization of light in a random ensemble of point scatterers", Phys. Rev. Lett. **112**, 1–5 (2014).

[303]L. Bellando, A. Gero, E. Akkermans, and R. Kaiser, "Cooperative effects and disorder: a scaling analysis of the spectrum of the effective atomic Hamiltonian", Phys. Rev. A. **90**, 1–10 (2014).

[304]R. R. Naraghi, S. Sukhov, J. J. Sáenz, and A. Dogariu, "Near-field effects in mesoscopic light transport", Phys. Rev. Lett. **115**, 1–5 (2015).

[305]R. R. Naraghi and A. Dogariu, "Phase transitions in diffusion of light", Phys. Rev. Lett. **117**, 1–5 (2016).

[306]J. M. Escalante and S. E. Skipetrov, "Longitudinal optical fields in light scattering from dielectric spheres and Anderson localization of light", Annalen der Physik **529**, 1–6 (2017).

[307]B. A. van Tiggelen and S. E. Skipetrov, "Longitudinal modes in diffusion and localization of light", Phys. Rev. B **103**, 174204 (2021).

[308]N. Cherroret, D. Delande, and B. A. Van Tiggelen, "Induced dipole-dipole interactions in light diffusion from point dipoles", Phys. Rev. A **94**, 1–11 (2016).

[309]S. E. Skipetrov and I. M. Sokolov, "Search for Anderson localization of light by cold atoms in a static electric field", Phys. Rev. B **99**, 1–7 (2019).

[310]T. Sperling, "The experimental search for Anderson localisation of light in three-dimensions", PhD thesis (Universität Konstanz, 2015).

[311]L. Schertel et al., "Tunable high-index photonic glasses", Phys. Rev. M **3**, 015203 (2019).

[312]L. A. Cobus, W. K. Hildebrand, S. E. Skipetrov, B. A. van Tiggelen, and J. H. Page, "Transverse confinement of ultrasound through the anderson transition in three-dimensional mesoglasses", Phys. Rev. B **98**, 214201 (2018).

[313]F. Andreoli, M. J. Gullans, A. A. High, A. Browaeys, and D. E. Chang, "Maximum refractive index of an atomic medium", Phys. Rev. X **11**, 11026 (2021).

[314]J. Haberko, L. S. Froufe-Pérez, and F. Scheffold, "Transition from light diffusion to localization in three-dimensional amorphous dielectric networks near the band edge", Nat. Commun. **11**, 4867 (2020).

[315]L. S. Froufe-Pérez, M. Engel, J. J. Sáenz, and F. Scheffold, "Band gap formation and anderson localization in disordered photonic materials with structural correlations", Proc. Natl. Acad. Sci. U. S. A. **114**, 9570–9574 (2017).

[316]N. Bender, A. Yamilov, A. Goetschy, H. Yılmaz, C. W. Hsu, and H. Cao, "Depth-targeted energy delivery deep inside scattering media", Nat. Phys. **18**, 309–315 (2022).

[317]M. Marcenko and L. Pastur, "Distributions of eigenvalues for some sets of random matrices", Math. USSR-Sbornik **1**, 457–483 (1967).

[318]R. Pnini and B. Shapiro, "Fluctuations in transmission of waves through disordered slabs", Phys. Rev. B **39**, 6986–6994 (1989).

[319]R. Sarma, A. Yamilov, P. Neupane, B. Shapiro, and H. Cao, "Probing long-range intensity correlations inside disordered photonic nanostructures", Phys. Rev. B **90**, 014203 (2014).

[320]M. Horodynski et al., "Optimal wave fields for micromanipulation in complex scattering environments", Nat. Photonics **14**, 149–153 (2019).

[321]M. Kaczvinszki, N. Bachelard, J. Hüpfl, M. Horodynski M. Kühmayer, and S. Rotter, "Optimal cooling of multiple levitated particles through far-field wavefront-shaping", arXiv:2103.12592 (2021).

[322]C. E. Shannon, "A mathematical theory of communication", Bell System Technical Journal **27**, 379–423 (1948).

[323]E. Macé, G. Montaldo, I. Cohen, M. Baulac, M. Fink, and M. Tanter, "Functional ultrasound imaging of the brain", Nat. Methods **8**, 662–664 (2011).

[324]F. Brenguier et al., "Towards forecasting volcanic eruptions using seismic noise", Nat. Geosci. **1**, 126–130 (2008).

RÉSUMÉ

En imagerie, on cherche à caractériser un milieu inconnu en le sondant avec une onde puis en analysant les échos réfléchis par le milieu. C'est, par exemple, le principe de l'échographie ultrasonore, de la tomographie par cohérence optique ou de la sismologie par réflexion. Cependant, la propagation des ondes entre les capteurs et le plan focal est souvent dégradée par les hétérogénéités du milieu lui-même. Elles peuvent induire des distorsions des fronts d'onde et des événements de diffusion multiple qui dégradent fortement la résolution et le contraste de l'image. Ces phénomènes constituent donc les limites les plus fondamentales de l'imagerie dans tous les domaines de la physique des ondes.
Cependant, l'émergence des réseaux multi-éléments et les progrès récents en science des données ouvrent la voie à une nouvelle révolution en imagerie. Dans ce contexte, nous avons développé une approche matricielle de l'imagerie dans les milieux hétérogènes. Le formalisme matriciel est en effet un outil idoine pour compenser localement les aberrations sur de grands champs de vision, brisant ainsi les limites actuelles des méthodes de focalisation adaptative. Il conduit également au changement de paradigme suivant en imagerie: Alors que la diffusion multiple est généralement considérée comme un cauchemar, l'approche matricielle peut en tirer profit pour une imagerie hautement résolue et ultra-profonde des milieux diffusants. L'imagerie matricielle est également un outil de caractérisation prometteur puisqu'elle peut fournir une tomographie à haute résolution de la vitesse des ondes et des paramètres de diffusion. Tous ces concepts sont appliqués à la fois à l'optique (pour l'imagerie des tissus biologiques), à l'échographie (pour le diagnostic médical) et à la sismologie (pour la surveillance des volcans et des failles sismiques).
D'un point de vue plus fondamental, un formalisme matriciel est particulièrement adéquat pour sonder le transport des ondes dans les milieux fortement diffusants. D'une part, l'interférence constructive entre des chemins de diffusion réciproques peut ralentir, voire stopper le processus de diffusion. D'autre part, les phénomènes d'interférence peuvent, au contraire, aider les ondes à trouver leur chemin à travers un dédale de diffuseurs. La matrice de diffusion constitue alors un outil unique pour sonder ces canaux de propagation ouverts et mettre en évidence l'importance des boucles de diffusion récurrentes au seuil de la localisation d'Anderson.

MOTS CLÉS

Ondes en Milieux Complexes, Imagerie Matricielle, Diffusion Multiple, Phénomènes d'Interférence

ABSTRACT

In wave imaging, we aim at characterizing an unknown environment by actively probing it and then recording the waves reflected by the medium. It is, for example, the principle of ultrasound imaging, optical coherence tomography or reflection seismology. However, wave propagation from the sensors to the focal plane is often degraded by the heterogeneities of the medium itself. They can induce wave-front distortions (aberrations) and multiple scattering events that can strongly degrade the resolution and the contrast of the image. Aberration and multiple scattering thus constitute the most fundamental limits for imaging in all domains of wave physics.
However, the emergence of multi-element technology and recent advances in data science pave the way towards a next revolution in wave imaging. In that context, we developed a universal matrix approach of wave imaging in heterogeneous media. A matrix formalism is actually the perfect tool to locally compensate for aberrations over large imaging volumes, thus breaking the limitations of adaptive focusing methods. It also leads to the following paradigm shift in wave imaging: Whereas multiple scattering is generally seen as a nightmare, a matrix approach can take advantage of it for ultra-deep and high-resolution imaging. Our matrix approach is also a promising characterization tool since it can provide a high-resolution tomography of the wave velocity and of scattering parameters. All these concepts are applied to both optics (for in-depth imaging of biological tissues), ultrasound imaging (for medical diagnosis) and seismology (for monitoring of volcanoes and fault zones).
From a more fundamental perspective, a matrix formalism can also be particularly fruitful to probe exotic wave transport phenomena in the strong scattering regime. On the one hand, constructive interference between reciprocal multiple scattering paths can eventually stop the diffusion process, giving rise to Anderson localization. On the other hand, interference phenomena can also help waves to find a way through a maze of disorder. The scattering matrix provides a unique tool to probe these open/close scattering channels and highlight the importance of recurrent scattering loops at the onset of 3D Anderson localization.

KEYWORDS

Waves in Complex Media, Matrix Imaging, Multiple Scattering, Interference Phenomena